Spring 2022

Advancement of New Solid-Oxide Iron-Air Battery (SOIAB) Operated on High-Temperature Oxide-Ion Chemistry

Qiming Tang

ADVANCEMENT OF NEW SOLID-OXIDE IRON-AIR BATTERY (SOIAB) OPERATED ON HIGH-TEMPERATURE OXIDE-ION CHEMISTRY

by

Qiming Tang

Bachelor of Engineering
Hunan University of Technology, 2015

Master of Engineering
Harbin Institute of Technology, 2018

Submitted in Partial Fulfillment of the Requirements

For the Degree of Doctor of Philosophy in

Mechanical Engineering

College of Engineering and Computing

University of South Carolina

2022

Accepted by:

Kevin Huang, Major Professor

Xinyu Huang, Committee Member

Dongkyu Lee, Committee Member

William E Mustain, Committee Member

Tracey L. Weldon, Interim Vice Provost and Dean of the Graduate School

DEDICATION

This study is wholeheartedly dedicated to my parents, Yanjin Fan and Zhebing Tang, who offer endless love and support throughout my life.

ACKNOWLEDGEMENTS

Many honest thanks:

My advisor, Prof. Kevin Huang, for his unending research spirit, meticulous caring, and financial supporting. My committee, Prof. Xinyu Huang, Prof. Dongkyu Lee, and Prof. William Mustain for their valuable feedback and guidance. Members of HuangLab of the past and present for their academic discussion and always being a source of comradery and drive.

Friends in Huntington Place, Mr. Xuan Wang, Dr. Hanfei Mei, Dr. Wenfeng Xiao and Mr. Rui Xin for their caring and joy all the times off work. Friends in USC, Mr. Rob Lichtenheld, Ms. Charlotte Crotwell, Mr. Aidan Billings, Ms. Xiaoya Gao for their communications and enriching my life in the campus even during pandemic. I enjoyed every minute.

My girlfriend, Ms. Qin Jiang, for her complete understanding and sharing all my sadness, happiness, failure, and success in everyday of my Ph.D. study. My parents for everything they sacrificed to raise me right and always give me the best.

At the end, I appreciate for the world peace and hope pandemics do end soon.

ABSTRACT

Climate change caused by anthropogenic greenhouse gas (GHG) emissions such as the burning of fossil fuels for power generation and industrial processing is affecting the global climate. To address this critical issue, a transition from fossil energy to renewable energy, especially wind and solar, is necessary. However, to successfully realize this transition, a cost-effective and large-scale stationary electricity storage system is indispensable. In this work, a new type of solid-oxide iron-air battery (SOIAB) operated on high-temperature oxide-ion chemistry is studied for this purpose due to its unique cycling characteristics suitable for large-scale Long Duration Electricity Storage (LDES) applications.

In the first part of the thesis, the reduction kinetics of iron oxides to metallic iron with hydrogen as the reducing agent is investigated. Aimed at understanding and ultimately improving the kinetics of FeO_x reduction, it covers the kinetic studies on isothermal H_2-reduction of iron oxides (derived from Fe_2O_3) as oxygen carrier in a Chemical Looping Hydrogen (CLH) and SOIAB environments. ZrO_2 is purposely mixed with FeO_x to prevent Fe particles from sintering, thus obtaining reliable kinetic data. It was found that the reduction of Fe_3O_4 to Fe follows two consecutive steps and can be reasonably described by phenomenological chemical-controlled and diffusion-controlled kinetic models. In addition, guided by thermodynamics, the desirable starting oxide phases, i.e., Fe_3O_4 and FeO, were obtained by precisely controlling the ratio of partial pressures of H_2O and H_2. The kinetics of the two one-step reduction reactions follows

nicely the Johnson-Mehl-Avrami (JMA) phase transformation model. The results show that FeO-to-Fe reduction exhibits two orders of magnitude higher rate constant than Fe_3O_4-to-Fe with half the activation energy. The obtained kinetic parameters provide firsthand data for engineering and design of practical SOIABs.

In the second part of the thesis, the Reversible Solid Oxide Cell (RSOC) in the SOIAB, a critical component determining the performance and lifetime, is studied. In order to improve the electrochemical performance and stability of the battery, a new battery vessel with a better gas tightness has been redesigned, and the anode supported thin electrolyte layer was made by dip-coating technology and modified by Gadolinium Doped Cerium (GDC) infiltration. The electrochemical performance testing results suggest that the modified RSOFC is an important step in improving the battery performance. Compared to dry-pressed cells, the dip coated cells show a power enhancement of 30%.

In the third part of the thesis, two types of new energy storage unit (ESU) materials were designed to enhance reduction kinetics. The slow FeO_x reduction kinetics is significantly improved by IrO_2 nanoparticles in Fe-based ESU, achieving high cycle efficiency of 73% at a high-power density of 50 mA cm^{-2}. Furthermore, $BaZr_{0.4}Ce_{0.4}Y_{0.1}Yb_{0.1}O_{3-\delta}$ (BZC4YYb), a proton-conducting perovskite, was also studied as support for Fe particles in ESU. Compared to the traditional oxide support ZrO_2, this new support significantly enhances the kinetics of redox reactions, achieving a high round trip efficiency (RTE) of ~65% at 1.5 C (75 mA cm^{-2}).

TABLE OF CONTENTS

LIST OF TABLES

LIST OF FIGURES

LIST OF SYMBOLS

P_{H_2O} Partial pressures of water.

P_{H_2} Partial pressures of hydrogen.

P_{O_2} Partial pressures of oxygen.

E_N^* Theoretical Nernst potential of battery.

E^o Fixed electromotive force under the standard state.

ΔG^0 Standard Gibbs free energy change at specific temperature.

N_e Number of electrons transferred in the reaction (from balanced reaction).

F Faraday constant (96,485 C mol^{-1}).

n Number of electrons transferred in the cell reaction per mole metal.

R Universal gas constant, 8.314 J $mol^{-1}K^{-1}$.

T Temperature in kelvins.

SE^* Theoretical specific energy based on the mass of iron element, Wh kg^{-1}.

Q^* Total theoretical charge.

t Time in seconds.

I Applied current, A.

m_{Me} Mass of the metal in g.

M_{Me} Molar mass of the metal in g mol^{-1}.

SC* Theoretical specific capacity based on the mass of iron element, Ah kg^{-1}.

SE Actual measured specific energy.

V_a Actual measured potential of the battery.

U_{Me} Actual utilization of metal, %.

M^{n+} Metal ions, n is oxidation number.

S_{red} Area of reduction peak over the full reduction process.

I_{H_2Opro} Time-dependent ion current related to H_2O production.

ξ Reduction extent as a function of time.

k Rate constant.

A Pre-exponential factor.

E_a Activation energy.

$f(\xi)$ Mathematical function that depends on the controlling mechanisms.

$g(\xi)$ Integral mathematical function related to mechanisms of the reduction reaction.

λ Dimensionality of growth, 1, 2 and 3.

β Nucleation process, $0<\beta<1$,$\beta=0$ represents instantaneous nucleation and $\beta=1$ means a very slow nucleation rate.

n Avrami exponent that depends on the mechanism of nucleation and growth process.

ϕ Diameter of disc.

wt.% Percent of weight.

j Current density, A cm^{-2}.

R_p Polarization resistance.

η Overpotential.

j_0 Exchange current density.

α Transfer coefficient.

V_C Cell voltage in the full cell.

R_o Ohmic resistance.

R_t Total resistance.

P Power density of RSOFC.

Φ Heating rate, K s^{-1}.

T_{max} Temperature in kelvin corresponded to maximum TPR peak.

C Constant.

$OH_O^{\bullet}$ Proton defect.

$V_o^{\bullet\bullet}$ Oxide-ion vacancy.

O_o^X Lattice oxygen.

LIST OF ABBREVIATIONS

BYC ..... Yttrium-Doped Barium Cerate

BZC4YYb ..... $BaCe_{0.4}Zr_{0.4}Y_{0.1}Yb_{0.1}O_{3-\delta}$

CA .....Citric Acid

CAS..... Compressed Air Storage

CE ..... Counter Electrode

CLH.....Chemical Looping Hydrogen

CSED .....Charge Specific Energy Density

DSED ..... Discharge Specific Energy Density

EDS .....Energy Dispersive X-Ray Spectroscopy

EDTA.....Ethylene Diamine Tetraacetic Acid

EIS..... Electrochemical Impedance Spectroscopy

EMF .....Fixed Electromotive Force

ESB ..... Er Stabilized Bismuth

ESU .....Energy Storage Unit

FESEM..... Field Emission Scanning Electron Microscope

FIB .....Focused Ion Beam

GDC ..... Gadolinium Doped Ceria

GHG..... Greenhouse Gas

HE ..... Hydrogen Electrode

HRTEM.....High-Resolution Transmission Electron Microscope

ID .....Inside Diameter

IT ..... Intermedium Temperature

JMA ..... Johnson-Mehl-Avrami

LDES ..... Long Duration Electricity Storage

LSGM ..... Lanthanum Strontium Gadolinium Manganite

LSM ..... Sr Doped Lanthanium Manganite

MFC ..... Mass Flow Controller

MIEC ..... Mixed Ionic and Electronic Conductor

MPD ..... Maximum Power Density

MS ..... Mass Spectrometer

NOAA ..... National Oceanic and Atmospheric Administration

NZE ..... Net-Zero Emissions

OC ..... Oxygen Carrier

OCV ..... Open Circuit Voltage

OD ..... Outside Diameter

OE ..... Oxygen Electrode

OER ..... Oxygen Evolution Reaction

ORR ..... Oxygen Reduction Reaction

PHS ..... Pumped-Hydro Storage

PVB ..... Polyvinyl Butyral

PVP ..... Polyvinylpyrrolidone

RSOFC ..... Reversible Solid Oxide Fuel Cell

RTE ..... Round Trip Efficiency

ScSZ ..... Scandia Stabilized Zirconia

SED ..... Specific Energy Density

SEM ..... Scanning Electron Microscope

SOC.....State of Charge

SOEC ..... Solid Oxide Electrolyzer Cell

SOFC.....Solid Oxide Fuel Cell

SOIAB..... Solid Oxide Iron-Air Battery

SOMAB .....Solid Oxide Metal-Air Battery

STEC..... Symmetrical Three-Electrode Cell

STEM.....Scanning Transmission Electron Microscope

TEC.....Thermal Expansion Co-efficient

TG ..... Thermogravimetric

TPB .....Triple Phase Boundary

TPB .....Triple Phase Boundary

TPR .....Temperature Program Reduction

WE ..... Work Electrode

XRD ..... X-Ray Diffraction

YSZ ..... Yttrium Stabilized Zirconia

CHAPTER 1

INTRODUCTION

1.1 Motivation

1.1.1 Climate Change and Energy

Climate change caused by anthropogenic greenhouse gas (GHG) emissions is already affecting the entire world with the extreme weather conditions. The carbon dioxide (CO_2) processes contributed about 75% of the total GHG emissions today, which is dominated by the burning of fossil fuels for energy production and industrial processing. Figure 1.1a shows that the global surface temperature has been steadily increasing since mid-20th century, now about 1^{o}C warmer than the long-term average of 1901-2000, resulting directly the mean sea level rise, extreme warm temperature and heavy precipitation events in some regions. An increasing number of countries are announcing pledges to achieve net-zero emissions (NZE) by 2050 to give the world an even chance of limiting the global temperature rise to 1.5 ^{o}C and achieve the complete transformation of the global energy system.

In order to pursue NZE and reduce energy intensity further, a transition away from fossil energy to renewable energy has been proposed. Renewable sources of energy, including wind and solar, do not produce CO2, which will provide more than 60% of energy use in 2050 in the NZE according to the report from International Energy Agency (Figure 1.1b). However, this kind of carbon-free energy sources offer intermittent power

supplies that do not always match real-time demand. Besides daily fluctuations depending on the weather events, variable electricity consumption will introduce more uncertainty if the wind and solar are integrated entirely into the grid. Thus, the generated renewable electrical energy must be stored in times of excess supply for later use. Battery storage is considered an appealing option to conventional pumped-hydro storage for its fast response, high energy density and modularity.

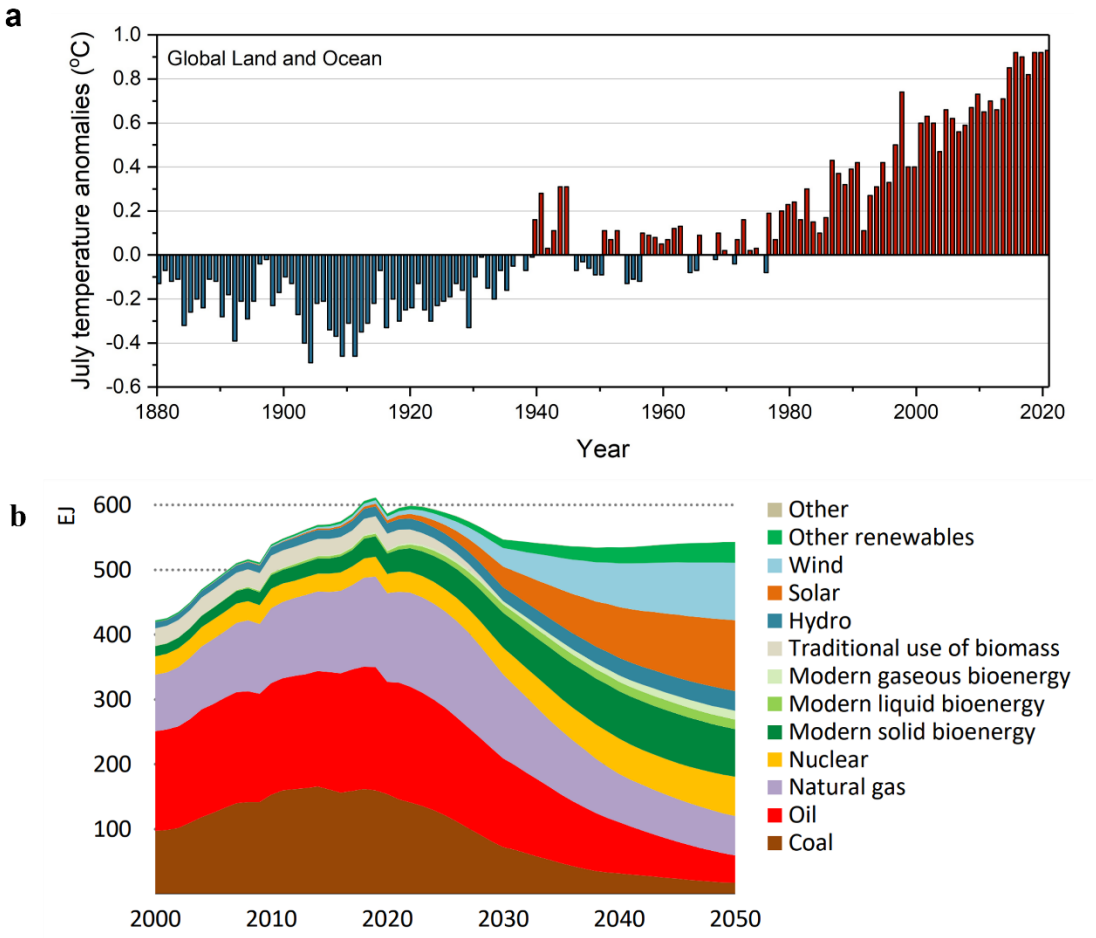

Figure 1.1 (a) Global average surface temperatures since 1880 compared to the long-term average (1901-2000). The zero line represents the long-term average temperature for the whole planet. Data from National Oceanic and Atmospheric Administration (NOAA) [1]. (b) Total energy supply in the NZE process. Renewables and nuclear power displace most fossil fuel use in the NZE, and the share of fossil fuels falls from 80% in 2020 to just over 20% in 2050 [2].

1.1.2 Need for Long Duration Electricity Storage (LDES)

Cost-effective, large-scale stationary electricity storage systems play a critical role in deepening renewable energy penetration and achieving resilient grid stability. As of today, the majority of commercial electricity storage deployments, as well as research development, focus on systems with durations ≤ 10 hours at rated power [3]. Recent analyses suggest that LDES with multi-day storage and even seasonal energy arbitrage will have significant advantages in allowing deeper penetration of low-cost wind and solar resources [4-8]. Unfortunately, today's most dominant large-scale electricity storage (e.g. pumped-hydro storage (PHS) and compressed air storage (CAS)) can only discharge 6 to 10 hours, which only satisfies applications of daily baseload energy time-shift and cannot leverage the benefits of LDES [5, 7], as shown in Figure 1.2. Attributed to the recent advancement in battery technology as well as high interest in stationary energy storage, Li-ion and redox flow batteries have been considered as a potential near-term solution for large-scale stationary electricity storage. From an economic perspective, these batteries are severely limited in extending storage durations beyond 10 hours due to the high costs of scaling the quantity of stored electricity, not to mention the safety concern on using clustered Li-ion batteries for large-scale application. Therefore, there is currently a significant lack of economically attractive LDES technologies on the market. To address this technological gap, new electrochemical storage concepts to store more energy in the battery system design and electrode materials optimization are needed.

Metal-air batteries assembled from metal anode and an air-breathing cathode in a proper electrolyte are emerging as a new energy storage device with ultrahigh energy density (ca. 3500 Wh kg^{-1} for lithium-air batteries) [9-14], which can be a promising

replacement to traditional batteries. However, there are two crucial issues to be considered. First, using of liquid organic electrolytes in metal-air batteries is flammable and toxic [15]. Second, the oxygen diffusion through the oxygen electrode tends to be blocked by the condensed reaction product, such as Li_2O_2 in Li-Air batteries [13], which can suppress the further electrochemical reactions and quash the battery's power. Developing alternative all solid-state metal-air battery technology can potentially address the above issues. My PhD study is aimed to develop a novel solid oxide "iron-air" battery (SOIAB) operated on oxide-ion chemistry within intermediate temperature (500-650 °C) and composed of a Reversible Solid Oxide Fuel Cell (RSOFC) and Chemical Looping Hydrogen (CLH) unit.

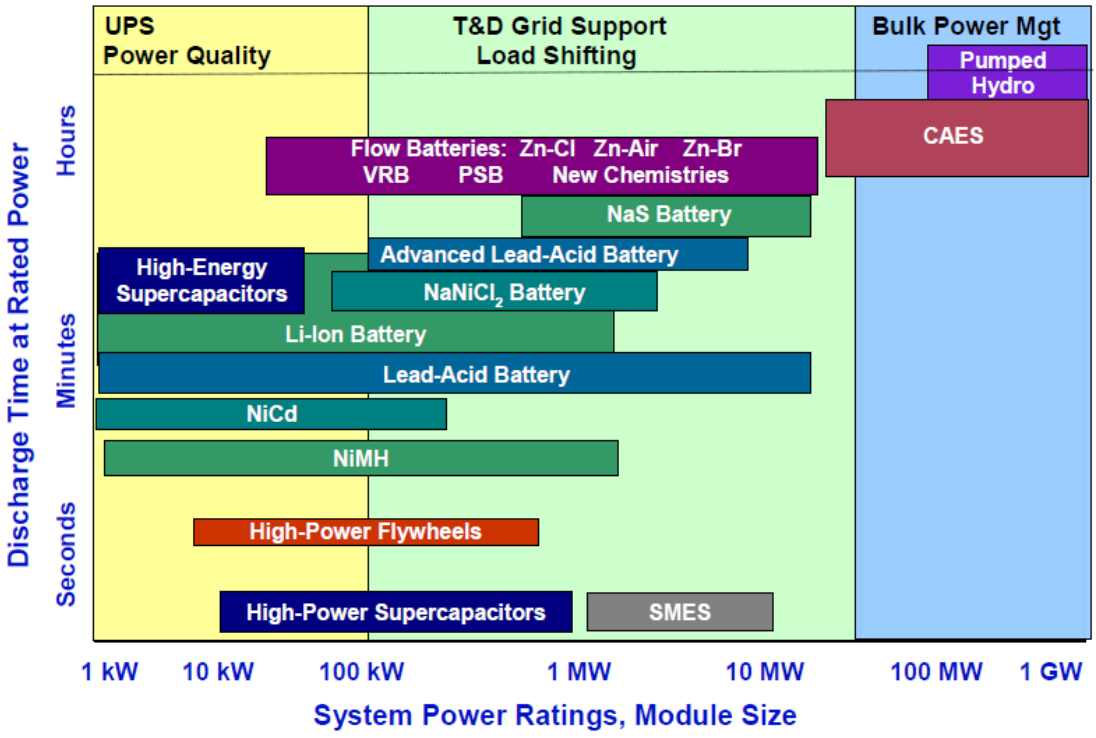

Figure 1.2 Comparison of discharge time and power rating for existing energy storage technologies [16].

1.2 Benefits and Limitations of SOMAB

1.2.1 Working Principles of Batteries

Battery is a device that stores chemical energy and converts it to electricity by a series of redox reaction in a close system. For example, Figure 1.3 shows the schematic illustration of metal air battery system, which consists of a metal anode, including Li, Na and K, and a porous air cathode separated by an ion-conducting membrane. As for an aprotic lithium-air battery system, at the anode, electrochemical potential forces the lithium metal to release electrons by oxidation reaction during discharge (without involving the cathodic oxygen) as following:

$$Li \rightleftharpoons Li^+ + e^- \tag{1.1}$$

The electrons move in the external circuit while the lithium ions are transferred in the internal circuit from anode to cathode. Thus, in the cathode, a possible cathodic mechanism could involve the following reactions, generally referred to as oxygen reduction reaction (ORR) during discharge process:

$$O_2 + Li^+ + e^- \rightleftharpoons LiO_2 \tag{1.2}$$

$$LiO_2 + Li^+ + e^- \rightleftharpoons Li_2O_2 \tag{1.3}$$

During charging, the reactions in electrodes reverse. It is worth noting that the electrochemical decomposition of lithium peroxide to Li^+ by oxygen evolution reaction (OER) upon charging in the cathode is not always reversible, which can be attributed to the fact that these peroxides have limited solubility in the electrolyte and are easy to stay on the air cathode, resulting in the accumulation effects and eventually shuts off the battery.

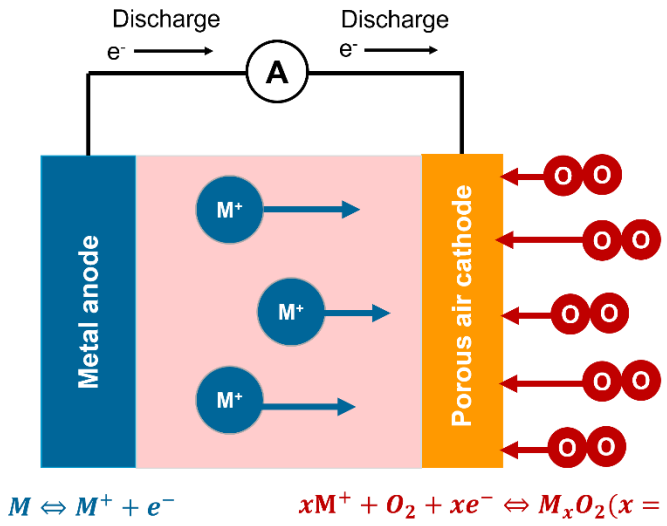

Figure 1.3 Schematic configuration and reactions taking place at the electrodes for the conventional metal-air battery based on liquid organic electrolyte.

To address the intrinsic issues in the traditional metal-air battery, a new type of all solid-state battery operated on high-temperature oxide-ion chemistry solid-oxide iron-air battery has been proposed for LDES [17-22]. One of the unique characteristics of SOMAB is its stable, efficient, and low-cost energy storage performance at low rates. The battery utilizes air as the unlimited oxygen source and low-cost iron-bed as the oxygen storage medium. During cycling, a RSOFC alternately operates in fuel cell mode for discharge and electrolyzer mode for charge, respectively, while oxygen is being stored in the metal/metal oxides redox couple via a gas-phase H_2/H_2O shuttle. Figure 1.4 exhibits the schematic of working principle of this all-solid oxide metal-air redox battery, which is composed of a RSOFC and energy storage unit (ESU). The RSOFC functions as the electrical charger and discharger, and the ESU serves as an energy store medium via metal/metal oxide redox reactions under the H_2/H_2O environment. During discharging, see the left part in Figure 1.4, the RSOFC operates as a fuel cell model (SOFC) where the oxygen in the air electrode (cathode) obtains electrons to produce O^{2-}, then the produced

O^{2-} goes to the fuel electrode (anode) through electrolyte and combines with H_2 in the ESU chamber further yield H_2O; the produced H_2O diffuses to ESU and reacts with metal, producing more hydrogen to sustain the electrochemical oxidation cycle. When the metal is fully or partly (in controlled portion) oxidized, the discharge process is stopped. During charging, as shown in the right part of Figure 1.4, the RSOFC serves as an electrolyzer (SOEC), where the H_2O in the anode will be split into H_2 and O^{2-} as the energy is input to the system, the produced H_2 diffuses back to ESU and reduces metal oxide into metal, producing more H_2O to sustain electrochemical reduction process. When all metal oxide or a controlled portion is depleted, the charging process is finished. Thus, in the air electrode, the reactions involved ORR/OER during discharge and charge are:

$$\frac{1}{2}O_2(g) + 2e^- \Leftrightarrow O^{2-} \tag{1.4}$$

For the fuel electrode, the total reaction can be summarized by combining the reaction loop in Figure 1.4:

$$Me(s) + xO^{2-} \Leftrightarrow MeO_x(s) + 2xe^- \tag{1.5}$$

The direction of the reversible redox reaction can be driven by the ratio of the partial pressures of water and hydrogen (P_{H_2O}/P_{H_2}) in the fuel electrode chamber. When the partial pressure of water is above the equilibrium value, oxidation is dominant (discharging), and vice versa.

By merging the eq. (1.4) and (1.5), the global reaction of the battery can be obtained:

$$Me(s) + \frac{x}{2}O_2(g) \Leftrightarrow MeO_x(s) \tag{1.6}$$

It is evident that this new all-solid-state battery is essentially a metal-air battery, albeit with a similar working principle with a redox flow battery instead of metal ions

transferring between electrodes in the conventional metal-air batteries. However, compared to the traditional Li-air and Zn-air system based on the aprotic electrolytes, this newly designed battery is advantageous in terms of safety, chemical stability and power and energy independence [17].

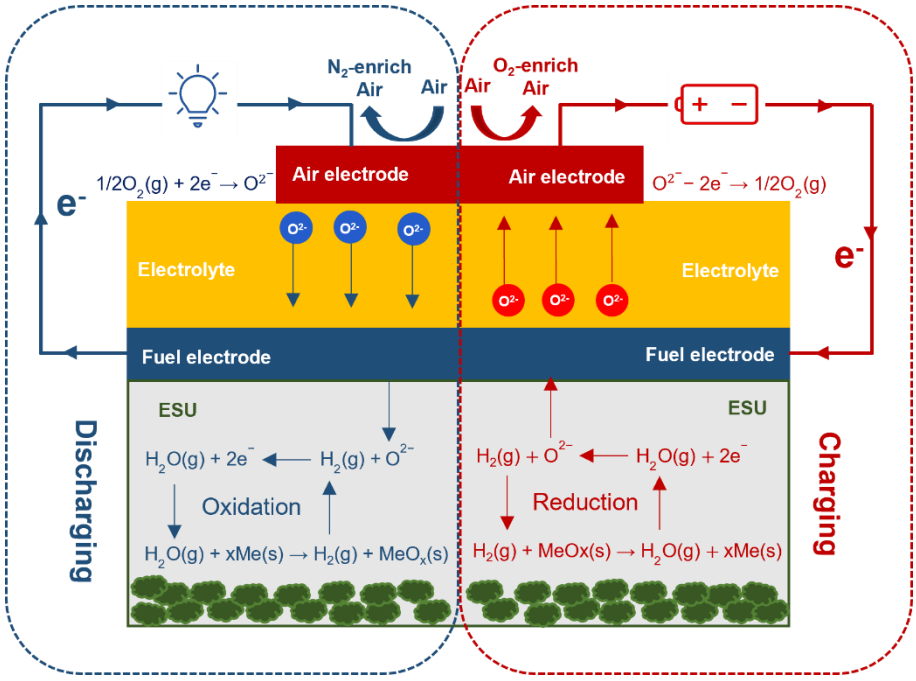

Figure 1.4 Schematic of working principle of the all-solid oxide metal-air redox battery.

1.2.2 Key Features of SOMAB

According to the configuration of this novel SOMAB, consisted of RSOFC and CLH production unite, several features of this new battery are conceived special from other batteries for large-scale stationary energy storage due to its all-solid state working environment and separated power and energy storage units.

(1) The combination of RSOFC and CLH production unit in a close system directly achieves an effective storage for hydrogen. The battery can be discharged/charged by consuming/reproducing hydrogen by metal/metal oxide redox couples.

(2) The fuel electrode and ESU are physically separated, enabling a fast charge-discharge

process and high safety without the concerns of electrode structure damage, metal dendrites formation or other byproducts resulted from metal ions insertion/desertion as commonly encountered in the traditional rechargeable batteries.

(3) Like a concentration cell, there should be a fixed electromotive force (EMF) with a fixed value of P_{H_2O}/P_{H_2} at an operating temperature in this novel battery. Such a state of charge (SOC) independent EMF feature is advantageous over liquid metal batteries, in which the EMF depends on the extent of metal ions transferring.

(4) The new battery presents a dual-electrons transfer process based on the solid oxygen ion electrolyte instead of the single-electron transfer in the traditional rechargeable batteries, such as Li-ion and Na-ion, improving the energy storage capacity at a higher current density.

(5) Energy can be designed independently from power to meet specific application: the energy of the battery is determined by the amount of metal in the ESU, while the power is controlled by the surface area of the RSOFC.

(6) The intermediate temperatures (500-650 ^{o}C) can effectively boost the reaction kinetics in electrodes, even in the absence of noble metal catalysts.

(7) It is sustainable, cost-effective, and environmental benignity because of the use of earth-abundant, inexpensive, and nontoxic redox couple energy storage materials, such as iron/iron oxide couples. Thus, it is suitable for applications for LDES.

1.2.3 Energy Density of SOMAB

The energy density is always relevant to the electrode materials in traditional batteries. However, the ESU is the most important component in the SOMABs since it not only determines the energy capacity, but also partially the power that a SOMAB can

deliver, which directly involves the metal redox reactions in the fuel electrode chamber. To derive the energy density of this system, thermodynamics is applied. For an SOMAB operated at fixed temperature (T), the equilibrium reaction can be built under such isothermal case, as shown in eq. (1.6). Then the theoretical Nernst potential (E_N^*) of this battery can be determined by the Nernst equation:

$$E_N^* = E^o - \frac{RT}{nF} \ln \left(\frac{1}{[P_{O_2}]^{\frac{x}{2}}} \right) \tag{1.7}$$

Where $E^o = \frac{-\Delta G^0}{N_e F}$, which refers to the EMF under the standard state. ΔG^0 is the standard Gibbs free energy change at specific temperature, which can be obtained from Table A1 listed most of the fuel oxidation reactions of Appendix A. R is the universal gas constant, 8.314 J mol^{-1} K^{-1}; T is the temperature in kelvins; n refers to the number of electrons transferred in the cell reaction per mole metal, $n = 2x$ for this case; and F is the Faraday constant, 96485 C mol^{-1}; P_{O_2} is the partial pressure of oxygen, $P_{O_2} = 0.21$ in air.

Then the theoretical specific energy (SE*, based on the mass of iron element, Wh kg^{-1}) can be calculated from eq. (1.7):

$$SE^* \ (Wh\ kg^{-1}) = \frac{Q^* \times E_N^*}{m_{Me}(kg)} = \frac{nF \times E_N^*}{3600 \times M_{Me} \times 0.001} \tag{1.8}$$

Where $Q^* = n \times F = I \times t(seconds)$, which refers to the total theoretical charge, here is one mole metal; M_{Me} is the molar mass of the metal in g mol^{-1}.

Thus, the theoretical specific capacity (SC*, based on the mass of iron element, Ah kg^{-1}) can be obtained based on eq. (1.8):

$$SC^* \ (Ah\ kg^{-1}) = \frac{SE^*}{E_N^*} \tag{1.9}$$

The actual measured specific energy (SE) is determined by the following:

$$SE\ (Wh\ Kg^{-1}) = \frac{\int_{t_1}^{t_2}(I_a \times V_a)dt}{m_{Me}(kg)} \tag{1.10}$$

Where, t_1 and t_2 refers to the process of charging or discharging; I_a is the applied current; V_a is the actual measured potential of the battery. Thus, the round trip efficient (RTE, %) can be calculated by

$$RTE = \frac{SE_{discharge}}{SE_{charge}} = \frac{\int_{t_1}^{t_2}(I_{discharge} \times V_{discharge})dt}{\int_{t_1}^{t_2}(I_{charge} \times V_{charge})dt} 100\% \tag{1.11}$$

The C-rate, describing how fast a battery charges and discharges, can be expressed by applied current. For example, a 1C battery needs one hour to charge or discharge fully, while a 0.5C battery requires two hours:

$$I_{@1c} = \frac{nF}{3600\ seconds} \text{ and } I_{@0.5c} = \frac{nF}{7200\ seconds} \tag{1.12}$$

Since the energy capacity of this system depends on the metal/metal oxide mass, the utilization of metal (U_{Me}, %) is of crucial parameter for this new energy storage system, which can be calculated from the following equations:

$$t_{Me}^{*} = \frac{Q_{Me}^{*}}{I_a} \tag{1.13}$$

$$U_{Me} = \frac{Q_{Me}}{Q_{Me}^{*}} = \frac{t_{Me}}{t_{Me}^{*}} \tag{1.14}$$

Where t_{Me}^{*} is the theoretical full discharge or charge time, Q_{Me}^{*} is the total charge capacity from metal, Q_{Me} and t_{Me} are the measured charge capacity and actual discharge/charge time (second), respectively.

Therefore, to achieve a suitable SOMAB for LDES, we must think about the ESU, such as redox couple materials we choose, equilibrium redox reaction under isothermal condition in the close system, and the utilization of active materials during cycling. All of them will directly impact the energy density, cost, safety, and lifespan.

1.2.4 Challenges for SOMAB

Despite those encouraging features mentioned above, this novel metal-air battery still faces two challenges from the RSOFC and ESU. As of RSOFC, combination of both SOFC and SOEC technology into a close system requires higher reversibility, and the high electrode polarization losses in RSOFC when operating at intermediate temperatures should be also considered. For ESU, there is very little known about the rate-limiting steps and fundamental mechanisms governing the kinetics of the underlying mixed-valent metal/metal-oxide redox reactions in this new battery. Usually, the process of oxidation of metal is faster than that of reduction of oxide due to an intrinsically higher kinetic rate constant for metal-oxidation, resulting in an easy discharge than charge. Therefore, enhancing reduction kinetics in ESU is a key step to achieve a successful development of the new SOMAB system [23].

1.3 Materials Selection for SOMAB

Advancements in SOMAB are influenced by the electrical performance of RSOFC and redox reversibility of ESU. Although a large number of research efforts have been devoted into SOFCs field over the past decades, problems still remain with regard to performance and durability, especially in the intermediate temperature region (500-650 ^{o}C). The ESU is a CLH production system, which can be realized in a fluidized bed reactor with redox reversible oxygen carries. Therefore, an important criterion for improving this battery performance is the materials of choice, including the electrodes and electrolyte materials in RSOFC and oxygen carries in ESU.

1.3.1 Electrolytes for RSOFC

In RSOFC, the electrolyte serves as a dense separation between anode and cathode. It

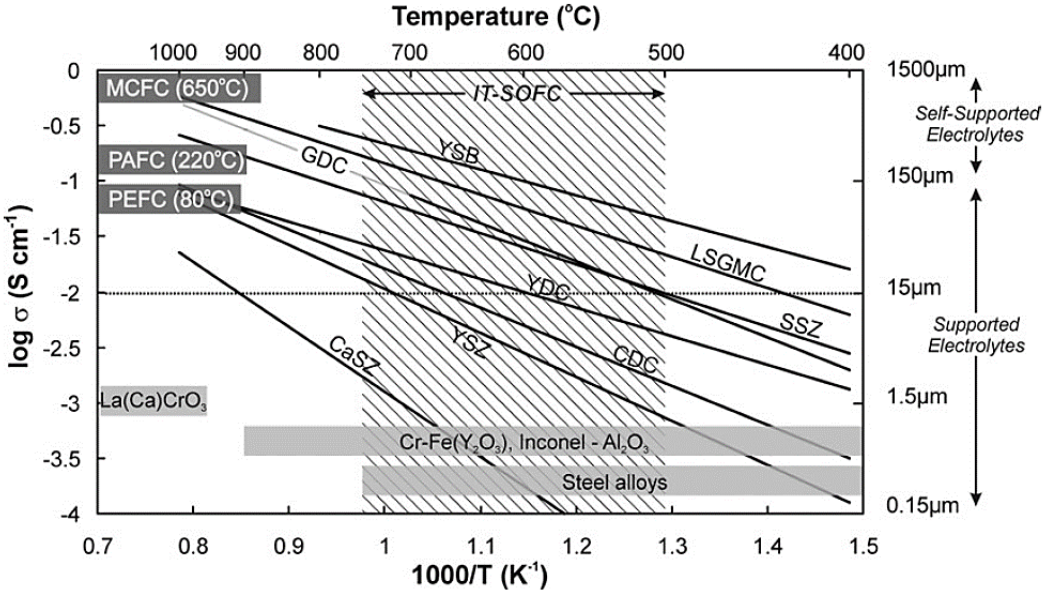

Figure 1.5 Specific ionic conductivity as a function of operational temperature for different solid oxide fuel cell electrolytes [24].

must be stable in both reducing and oxidizing environments and must have high ionic conductivity (>0.1 Scm^{-1}) with a negligible electric conductivity [25-27]. The electrolyte performance depends mainly on the operation temperature, thickness, and intrinsic materials properties. The most commonly studied oxygen conductor electrolytes are Zirconia-based electrolytes [28-30], e.g., scandia stabilized zirconia (ScSZ) and yttrium stabilized zirconia (YSZ), ceria-based electrolytes [31-33], such as gadolinium doped ceria (GDC), and lanthanum-based electrolytes, such as lanthanum strontium gadolinium manganite (LSGM). Figure 1.5 shows the ionic conductivities as a function of operational temperature for different electrolytes. From the perspective of commercial applications in intermediate temperature region (500-650 ºC), SOFCs based on CeO_2-based electrolytes are less attractive due to their intrinsically high electronic conduction and mechanical issues upon exposure to reducing atmospheres although they show excellent performance in lab-scale button cells [34]. The LSGM-based SOFCs face the same problems because

of its high cost, high chemical reactivity with conventional electrode materials, and low mechanical strength [31, 35]. Therefore, ZrO_2-based SOFCs still remain the mainstream of commercial development. Among all ZrO_2-based electrolytes, Sc-and Ce- co-doped ZrO_2 (SCSZ) stands out to be a promising IT-electrolyte due to its high and stable oxide-ion conductivity over a wide range of oxygen partial pressure, excellent chemical stability, high mechanical strength, and good compatibility with nickel metal [36].

1.3.2 Anodes for RSOFC

The anode materials should have high ionic and electrical conductivity to transport the electrons during the electrochemical reactions. The anode usually is a metal-ceramic mixture (cermet), where the metal component acts as electrical conductor while the ceramic (electrolyte material) provides ionic conductivity and improves matching in thermal expansion co-efficient (TEC) between electrolyte and anode in some degrees. Besides, it must possess a large surface area of triple phase boundary (TPB) to accelerate the anodic reactions, and a prominent porous microstructure to improve gas diffusion [24, 37]. For intermediate temperature, the cells are usually built with anode supporting electrolyte, which can reduce the ohmic loss attributed to the electrolyte thickness, enabling lower operating temperature and higher performance. The most common anode materials for SOFC are the nickel-based cermet (Ni/YSZ and Ni/ScSZ) which exhibits superior catalytic properties for fuel oxidation and good current collection.

1.3.3 Cathodes for RSOFC

RSOFC cathodes generally consists of two individual phases: an electronic conducting phase acting as catalysis for the oxygen reduction reaction (ORR) and an ionic conducting phase for transporting oxygen ions [25, 38-42]. Conventional perovskite-type

Sr doped $LaMnO_3$, such as $La_{1-x}Sr_xMnO_3$ (LSM), are commonly used as oxygen electrodes for high-temperature Zirconia-based electrolytes RSOFC, owing to its high electrical conductivity, good structure/chemical stability, and suitable TEC with the YSZ/GDC electrolyte [43]. However, their electrochemical property is very poor at reduced temperatures, which can be ascribed to low ionic conductivity in LSM at that condition. The main routes for optimizing cathode electrochemical performance include finding new compositions and novel families of materials, and modifying the morphology, such as improving the active surface area, interface area and porosity [44]. Similar to Ni/ScSZ anode electrodes, LSM is thus often combined with a high ionic conducting phase to extend the active TPB region out into the three-dimensional structure of the cathode. In this regard, the stabilized Bi-based has been reported as the highest ionic conductivity in the intermediate temperature region among all the well-known oxide-ions conductors [38]. For example, Er-stabilized Bi_2O_3 (ESB) exhibited prominent conductivity at 500 ºC (0.0268 S cm^{-1}), which is much higher than that of YSZ (0.0009 S cm^{-1}) and GDC (0.005 S cm^{-1}) [45, 46]. Unfortunately, the Bi_2O_3 based composite has very poor structural stability below the order-disorder transition temperature where oxygen vacancies tend to order with time, leading to a decay in ionic conductivity [47]. In order to improve the stability of Bi_2O_3 based composite, aliovalent doping with rare earth cations, such as Y, Ce, Er and Zr, has been systematically investigated and stable conductivity has been achieved by the doping [48]. Combining a co-doped Bi_2O_3 oxygen-ion conductor with LSM as composite cathode for intermediated temperature RSOFC should be a logical strategy.

1.3.4 Iron-Air System for ESU

While the current state of the art of the SOFC technology has greatly facilitated the development of RSOFC since the same cell designs can be used for the SOEC mode [42], the other vital configuration in the SOMAB, viz. ESU, is still new research topic. Benefiting from the development of CLH technology, there are a large body of oxygen carriers (OC) reported in the literature, like Fe_2O_3, Ti_2O_3, Cr_2O_3, Cu_2O, NiO, Mn_2O_3, and WO_3, etc. [49-52]. All of them can be operated at high temperatures to produce H_2. Figure 1.6 compares E_N, SE* and specific cost of most transition metal related redox couples, among which Ti/TiO_2, Cr/Cr_2O_3, V/V_2O_3 and Mn/MnO exhibit the highest E_N and SE*, respectively, while the Cu/CuO redox couple has the lowest values. Another important criterion for selecting ESU metals is the equilibrium partial pressure of oxygen ($P_{O_2} atm$) in the anode chamber, which is controlled by the redox reaction as shown in Figure 1.4. In order to avoid undesirable oxidation of Ni in the anode and reduction of ZrO_2 electrolyte, a suitable $P_{O_2} atm$ in the fuel chamber should be controlled, which is lower than Ni/NiO and higher than Zr/ZrO_2 according to the Ellingham diagram, see Appendix B. For stationary energy storage, if the storage materials could be made less expensive, the economics would be even more appealing. Figure 1.6c shows the specific cost analysis for different metal/metal oxide couples candidates, suggesting Fe/FeO redox couple and W/WO_3 hold the lowest energy cost. Considering these criteria, the choice of ESU materials is narrowed down to W and Fe. However, according to the previous work, [53] the W/WO_3 redox couple exhibits a low redox activation at intermediate temperatures, leading to a reasonable performance only at a higher operation temperature (over 800 ^oC). Given the specific metal cost and energy density, there is a focus on

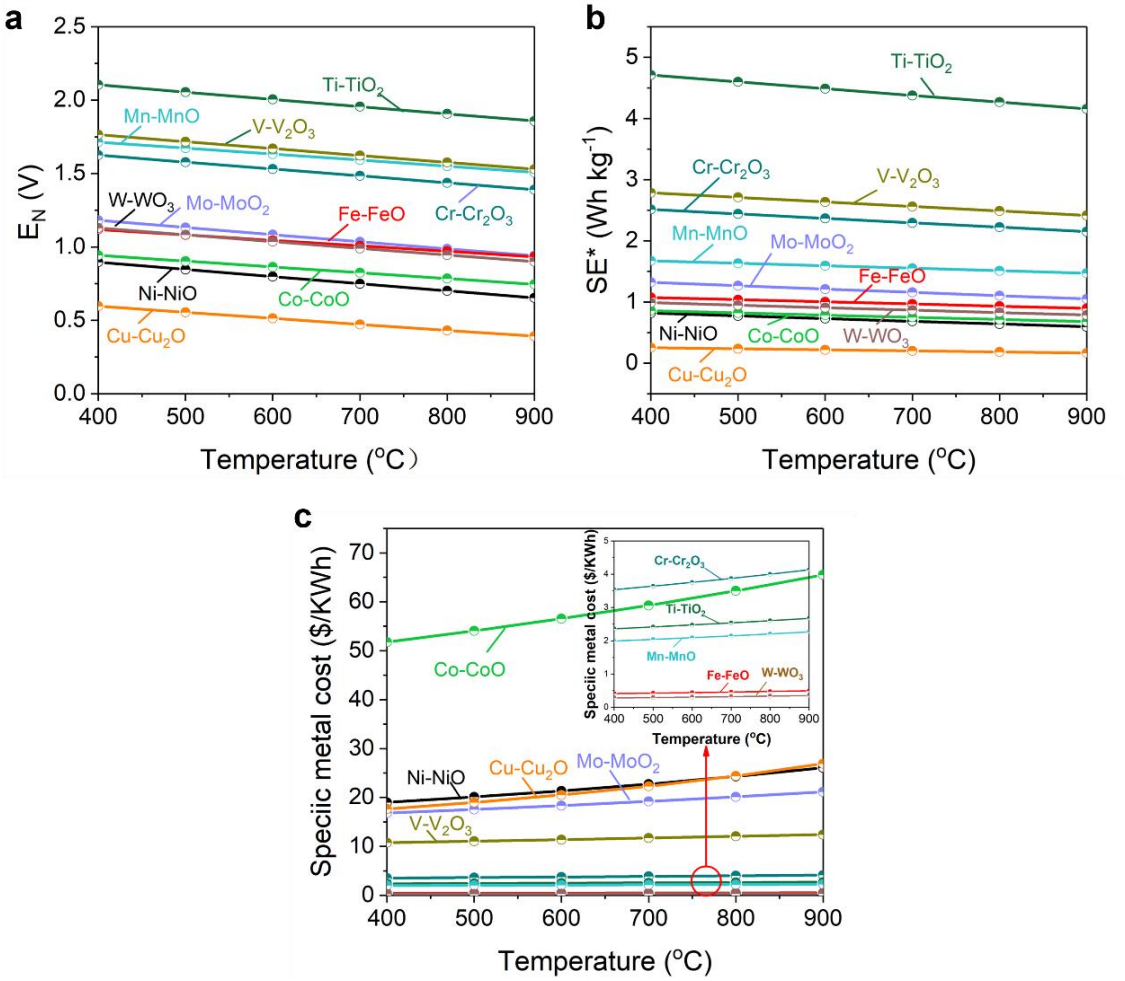

Figure 1.6 Comparison of SOMAB-related a) thermodynamic Nernst potential (E_N), (b) specific energy density based on metal mass (SE*) and (c) specific metal cost analysis among transition metal and oxide redox couples.

Fe/FeOx ESU materials for the SOMAB applications, leading to the name of solid oxide iron-air redox battery (SOIAB). Iron is the one of most significant components of the earth's crust, and it has been studied widely as main energy storage materials in conventional liquid Fe-air batteries.

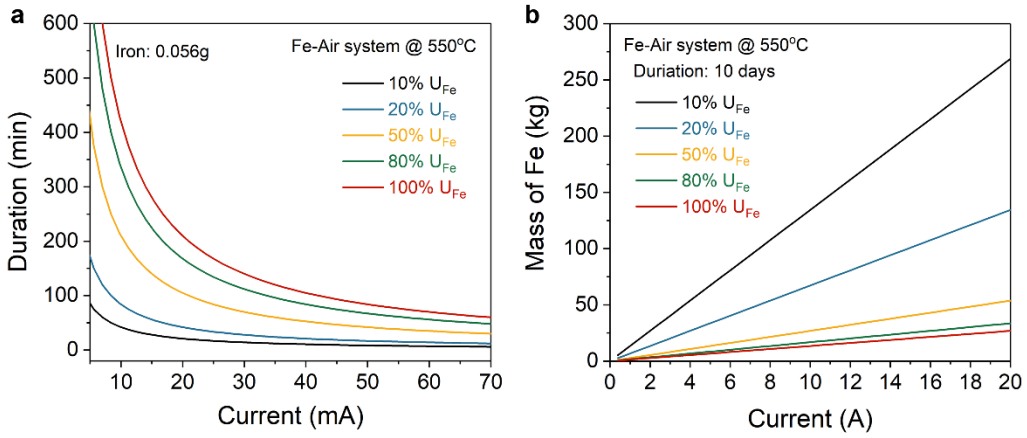

Figure 1.7 Current-U_{Fe}-duration relationship. (a) Discharge/charge duration with 0.056 g Fe (used in this study) *vs. j* and U_{Fe}; (b) the mass of Fe for 10 days storage at different j and U_{Fe}.

However, SOIAB's low rate-performance, while not suitable for applications requiring fast charge and discharge cycles, might not necessarily a problem for LDES as long as there is a sufficient amount of Fe available in the battery to store oxygen during discharge and produce hydrogen during charge. For example, a simple calculation based on Faraday's law indicates that 67.3 kg of Fe is needed to store electricity for 10 days at a current of 10 A and 20% Fe-utilization (see Figure 1.7). More importantly, energy (size of Fe-bed) and power (area of electrode) can be separately pursued in SOIAB for specific applications. It is envisioned for LDES applications that a large Fe-bed can be designed to store energy for months or even the entire renewable-rich season under a low power mode. Therefore, in addition to many other advantages of Fe-bed materials (*e.g.*, earth abundance and low cost), it is reasonable to regard IT-SOIAB as a potential technology for LDES.

1.4 Outline of This Thesis

Broadly, Chapter 1 introduces the motivation for seeking high-energy density and safe

solid-state metal-air battery. The novel solid oxide Fe-Air battery system was the first target of this search with many challenges, including anode, cathode in RSOFC and ESU materials. Chapter 2 is focused on the fundamental investigation for the Fe/FeOx couple reduction kinetics at high temperatures, which gives a new insight into improving the performance of battery. Chapter 3 covers the modification of anode supporting electrolyte in RSOFC, which address the main challenges for RSOFC stability and performance. Chapter 4 explores the modifications of iron bed (ESU) compositions, which leads to the improvement of redox activation and stability at the intermediate temperatures. Finally, Chapter 5 summarizes the main conclusions of this thesis and discusses some possible further work.

CHAPTER 2

KINETICS OF IRON OXIDES REDUCTION TO METALLIC IRON WITH HYDROGEN

Published in ACS Applied Energy Materials 2021, 4, 7, 7091–7100 and Chemical Engineering Journal, 2022, 434: 134771.

2.1 Introduction

FeO_x is the most popular choice of oxygen carriers (OC) for chemical looping hydrogen (CLH) reactor and solid oxide iron-air redox battery (SOIAB) due to its earth abundance, low cost, and high oxygen content. However, the performance of a Fe/FeO_x chemical looping cycle is critically limited by the reduction kinetics of FeO_x. Aimed at understanding and ultimately improving the kinetics of FeO_x reduction, this chapter covers the kinetic studies on isothermal H_2-reduction of Fe_3O_4 (derived from Fe_2O_3) as oxygen carrier in a CLH and SOIAB environment. In addition, the one-step reduction of Fe_3O_4-to-Fe and FeO-to-Fe is realized by precisely controlling the ratio of partial pressure of H_2O and H_2, upon which kinetic data are obtained. The obtained kinetic parameters provide firsthand data for engineering and design of practical SOIABs.

2.2 Experimental Methods

2.2.1 Materials Preparation

For Fe_2O_3-ZrO_2 powders: The starting Fe_2O_3-ZrO_2 composite OC was prepared by a co-precipitation method, in which the importance of mixing ZrO_2 with iron oxides to obtain

reliable kinetic data due to the excellent resistance of ZrO_2 to Fe-particles sintering. Briefly, the stoichiometric solutions of $Fe(NO)_3$•$9H_2O$ (≥99.999%, Sigma-Aldrich) and $ZrO(NO)_2$•$6H_2O$ (≥99.999%, Alfa-Aesar) in mole ratios of Fe:Zr=85:15 were first prepared by dissolving in deionized water. Then these two solutions were mixed in a beaker with a cation concentration of 0.1 M, and Polyvinylpyrrolidone (PVP, Sigma-Aldrich) as a surfactant was added while stirring constantly for 30 min. The resulting clear orange solution was then added dropwise to a slight excess of ammonium carbonate solution under constant stirring, while the temperature of the solution was maintained at 35 ^oC. To ensure full precipitation of all the cations in the solution, the molar ratio of $(NH_4)_2CO_3$ (Sigma-Aldrich) and M^{n+} (M= Zr and Fe) was kept as $n(NH_4)_2CO_3$: nM^{n+}=2.5 : 1. The resulting brown precipitate was then left in the solution for 20 h with continuous stirring. Finally, the aged suspension precipitate was collected through a filter and washed several times with deionized water and ethanol by centrifuge, and finally dried overnight at 80 ^oC. To obtain the Fe_2O_3-ZrO_2 OC, the collected precipitate was calcined in static air at 600 ^oC for 2h. Similarly, pure Fe_2O_3 OC was also synthesized with the same method but without $ZrO(NO)_2$•$6H_2O$.

2.2.2 Apparatus and Testing

For the overall reduction experiment: To create a similar reaction environment to the SOIAB, reduction of the prepared Fe_2O_3-ZrO_2 and pure Fe_2O_3 OCs and their subsequent kinetic studies were performed in a fixed bed reactor; the experimental setup is illustrated in Figure 2.1. The experimental system mainly consists of a quartz tube reactor, water

pump, temperature controller, a program-controllable four-way switch, mass flow controllers, and a mass spectrometer (MS, Pfeiffer Omnistar 100) at the outlet of the reactor. The gas flow rate was controlled by a mass flow controller (Alicat Scientific MFC Series). The steam was generated from a homemade steamer operated at 120 °C with a DI water feed rate at 8.037 μL min^{-1} controlled by a syringe pump (SyringeONE Programmable Syringe Pump), which will produce 10 sccm H_2O.

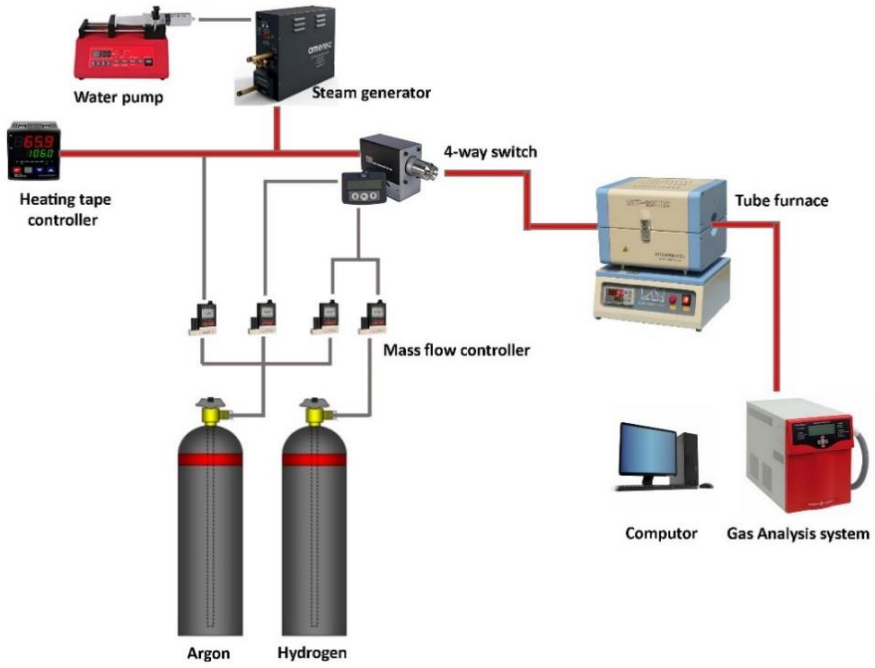

Figure 2.1 The system setup for kinetic study of FeO_x reduction.

Approximately 100 mg of OC supported on a lump of quartz wool was placed inside a quartz glass tube, and then the furnace was heated to 400 °C under argon at 200 sccm. Then, a mixture of H_2 and Ar with different concentrations (5%, 10% and 20% H_2) was introduced into the reactor during temperature ramp to the temperature of interest, *i.e.* 600, 650, 700, 750 and 800 °C. MS was used to analyze the effluent compositions and confirm a full reduction of the starting Fe_2O_3 into Fe. At each temperature, it was held for 20 min before the first oxidation by H_2O and the following reduction by H_2. Note that

under a CLH or SOIAB condition, the starting oxide composition for the reduction cycle depends on temperature and partial pressure of oxygen (or the ratio of partial pressures of H_2O to H_2). Therefore, we have chosen to use an H_2O-oxidation cycle to create *in situ* the equilibrium Fe-oxide composition for the subsequent reduction kinetics study. We will show later that this starting oxide composition for reduction kinetic study is Fe_3O_4 under the experimental condition.

For one-step reduction experiment: The only modification was the replacement of a steam generator/water pump by a water bubbler at the room temperature to ensure a more stable steam supply at the low concentration range. The described H_2O/H_2 ratio was then simply controlled by the mass flow rates of the add-in H_2. Briefly, the experiment was started by first loading 100 mg Fe_2O_3/ZrO_2 into a quartz tube reactor, following by raising furnace temperature to 400 ºC under Ar flowed at 200 sccm. Then, a 10% H_2-Ar was introduced into the reactor chamber during temperature ramp to the target point, *i.e.*, 500, 525, 550, 700, 750, 800 and 850 ºC. The effluent was constantly analyzed by an online MS during reduction and a full reduction of the Fe_2O_3 into Fe is confirmed by the H_2 concentration, i.e., there will be no H_2 consumption upon full reduction. After this initial full-reduction activation process, the oxidation was carried out by switching to a gas with a controlled H_2O/H_2 ratio to achieve a desired oxide form. To control the H_2O/H_2 ratio, a H_2 with a fixed mass flow rate is added into the room-temperature moistened Ar stream flowed at a fixed flow rate. We use Figure 2.5b of thermodynamic phase diagram as a guidance to dial a H_2O/H_2 ratio for a specific iron oxide. For example, P_{H_2O}/P_{H_2} = 0.4 was set for the oxidation of Fe to FeO at 700-850 ºC, whereas P_{H_2O}/P_{H_2} = 2.0 was set for the oxidation of Fe to Fe_3O_4 at 500-550 ºC. Once the wanted oxide

phase is realized, the one-step reduction, viz. Fe_3O_4 to Fe and FeO to Fe, was performed with different H_2 concentrations in Ar (5%, 10% and 20%). The reduction kinetics was evaluated based on the change in H_2O concentration in the effluent measured by MS.

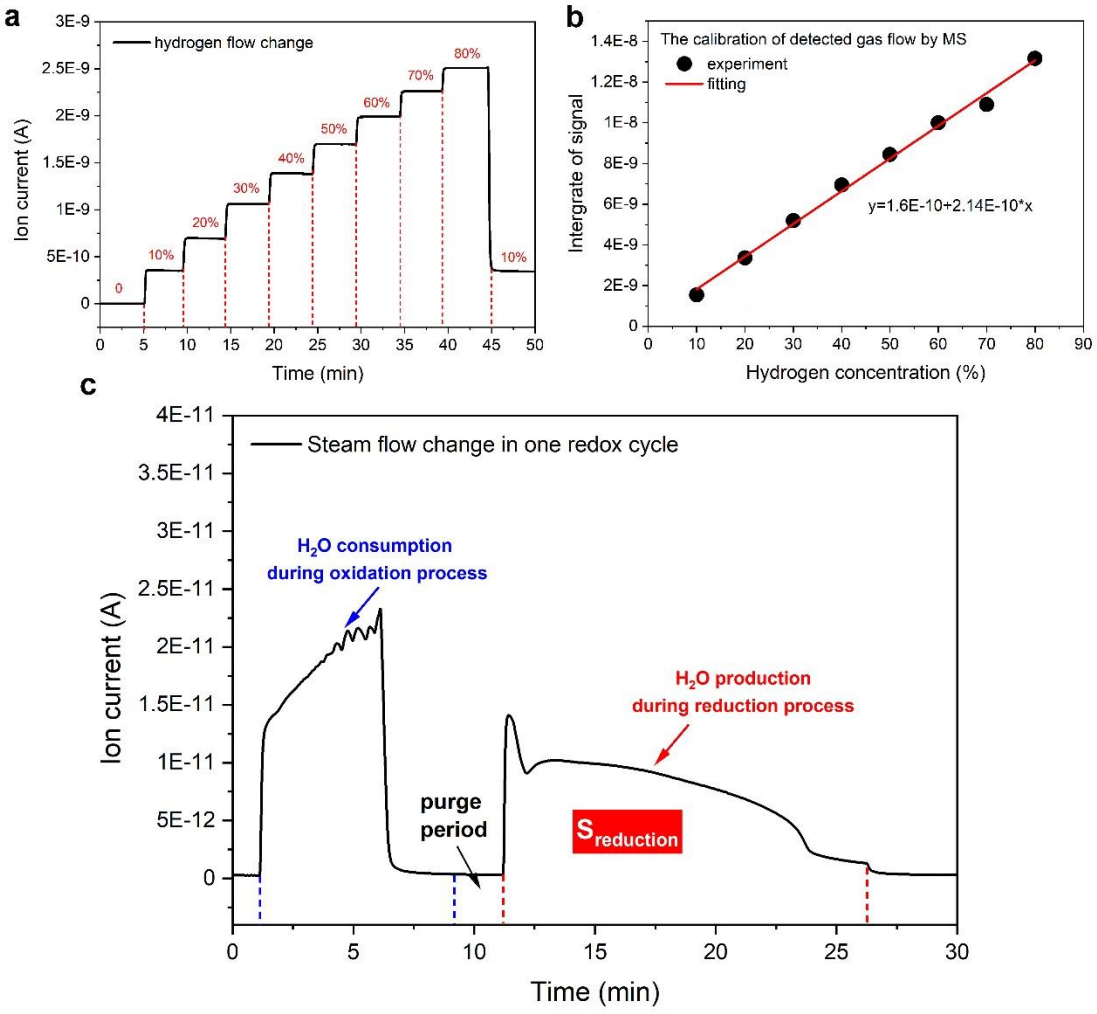

Figure 2.2 (a) The response of ion current in the MS system to the change of H_2 concentration; (b) the relationship between the integrated ion current and H_2 concentration; (c) the profile of change in outlet gas composition in one redox cycle of between Fe_3O_4 and Fe.

2.2.3 Data Processing

MS calibration: To accurately determine the gas composition, we first performed calibration on MS. The relationship between ion current and H_2 concentration read by

MFC is shown in Figure 2.2a. As H_2 concentration increases, so does the ion current. Figure 2.2b shows the linear relationship between the H_2 concentration and the integrated ion current, from which concentration of H_2 can be determined.

Reduction kinetic data: The reduction kinetics is evaluating by measuring the change in H_2 or H_2O concentration in the effluent by MS. Figure 2.2c shows the ion-current change during one full redox cycle. The first peak corresponds to the outlet water signal during the H_2O-oxidation process, and the second peak relates to the outlet water signal during the H_2-reduction process. The reduction extent, ξ (Fe_3O_4 to Fe) can be expressed as a function of time, t, using the following formula:

$$\xi(t) = \frac{\int_0^t (I_{H_2O\ pro})dt}{S_{red}} \tag{2.1}$$

Here, $I_{H_2O\ pro}$ is the time-dependent ion current related to H_2O production; S_{red} is the area of reduction peak over the full reduction process.

2.2.4 Materials Characterization

The phase composition of the prepared Fe_2O_3/ZrO_2 composite was examined by X-ray diffraction (Rigaku D/MAX-2100). The surface compositions of Fe_2O_3/ZrO_2 upon exposure to H_2O/H_2 mixture under different H_2O/H_2 ratios and temperatures were also probed by a Xplora plus Raman spectrometer (HORIBA) equipped with a commercial Linkam TS 1000 heating stage (Figure 2.3). Figure 2.3a shows schematically a quartz window, sealed with Buna O-ring, used to allow transmission of the excitation laser and collection of scattered photons. The stainless-steel jacket of the gas-stream chamber was cooled with a circulating water. Figure 2.3b-2.3e show the setup of *in-situ* Raman testing system. The lens with 50× magnification and long working distance (8mm) objective were used with laser excitation in wavelength of 638 nm. The Raman spectra were

collected using the LabSpec 6 software every 3 minutes. The morphologies of the Fe_2O_3/ZrO_2 was also captured by a field emission scanning electron microscope (FESEM, Zeiss Gemini500) fitted with energy dispersive X-ray spectroscopy (EDS).

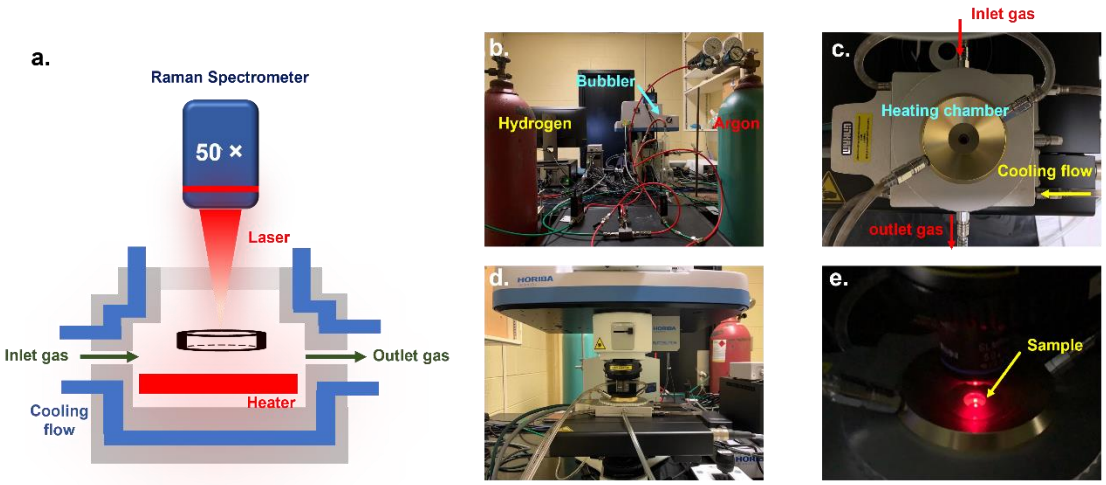

Figure 2.3 Schematic and picture of the environmental chamber and setup for the *in-situ* Raman spectroscopy.

2.3 Overall Reduction Kinetics

2.3.1 Phenomenological Models for Fe-Oxide Reduction

Generally, the reduction of iron oxides by H_2 is a complex, heterogeneous gas-solid reaction [54]. A schematic representation of the reaction between gas and solid particles is illustrated in Figure 2.4a. During the reduction, a gaseous reactant, such as H_2, will first reach the external surface of the solid material, and enter the internal body of the solid through pores. The reactant will then adsorb on the surface of the solid, where a chemical reaction takes place, forming gaseous products and new phases on the solid surface. Finally, the gaseous products diffuse out of the porous solid body and entrain into the bulk gas phase. Therefore, the kinetics of a gas-solid reaction could be limited by the rates of diffusion process and surface reaction, whichever is slower. If a dense outer shell

forms during reaction or agglomeration occurs, the progress of reaction can become limited by the diffusion process. In this case, both chemical and diffusion kinetics must be considered.

The following generic phenomenological kinetic equations has been used to represent the kinetics of reduction:

$$\frac{d\xi}{dt} = kf(\xi) \tag{2.2}$$

where $\frac{d\xi}{dt}$ represents the kinetic rate; t is the reduction time; ξ is the reduction extent; k is the rate constant, which is expressed by $k = A\ exp(-\frac{E_a}{RT})$, where A, E_a, R and T are pre-exponential factor, activation energy, gas constant and temperature, respectively; and $f(\xi)$ is a mathematical function that depends on the controlling mechanisms. If the reaction is controlled by chemical reaction, $f(\xi) = 3(1-\xi)^{2/3}$; if it is limited by the diffusion in the product layer, $f(\xi) = 3/2(1-\xi)^{2/3} * (1-(1-\xi)^{1/3})$ [55].

For reaction kinetics under isothermal conditions, the rate of eq. (2.3) can be analytically integrated to yield:

$$g(\xi) = \int_0^{\xi} \frac{d\xi}{f(\xi)} = kt \tag{2.3}$$

where $g(\xi)$ is an integral mathematical function related to mechanisms of the reduction reaction. Therefore, the relationship between the extent of reduction and time can be obtained, from which the kinetic rate constant *k* can be further determined.

For reduction that is chemical reaction controlled:

$$\boldsymbol{\xi} = 1-(1-kt)^3 \tag{2.4}$$

For reduction that is chemical reaction controlled:

$$\boldsymbol{\xi} = 1-(1-\sqrt{kt})^3 \tag{2.5}$$

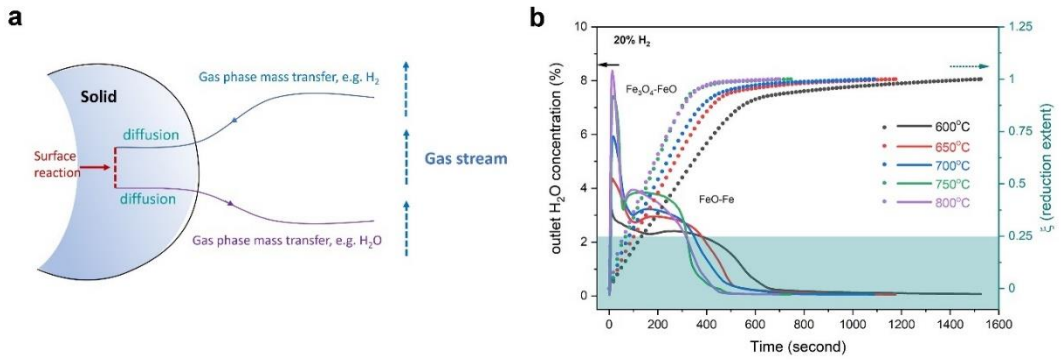

Figure 2.4 (a) A schematic diagram of the reaction between a gas and solid particle; (b) the outlet H_2O concentration and reduction extent of Fe_3O_4 *vs.* time with an inlet 20% H_2. Dots: reduction extent; lines: H_2O concentration measured by MS.

2.3.2 Determination of Stable Fe-Oxide Phase

The reduction kinetic behavior of Fe-oxides in H_2 has been investigated extensively by the thermogravimetric (TG) method. However, there are less reports in the literature on using MS method. Through analyzing the outlet gas compositions, the phenomenologically based mechanisms of reactions can be analyzed with accuracy and high fidelity. Figure 2.4b shows variations of the outlet H_2O concentration during a live reduction of Fe_3O_4 (after a full reduction from Fe_2O_3 to Fe in the starting Fe_2O_3-ZrO_2 and subsequent oxidation to Fe_3O_4 in 10% H_2O), and the corresponding reduction extent *vs.* time at different temperatures (600-800 °C) in 10% H_2-Ar. The reduction extent was calculated from eq. (2.1). The outlet H_2O concentration measured by MS increases rapidly at the beginning of the reaction, reaching a temporal maximum, and then decreases toward the end of reduction, suggesting the reduction is initially fast and then becomes slow. Also as expected, the rate of reduction is significantly faster at higher temperatures than at lower temperatures. The two peaks shown in Figure 2.4b appears to suggest that there are two distinct reactions involved in the reduction, which are relate to the following reactions:

$$Fe_3O_4 + H_2 \longrightarrow 3FeO + H_2O \quad (2.6)$$

$$3FeO + 3H_2 \longrightarrow 3Fe + 3H_2O \quad (2.7)$$

For the initial sharp peak, corresponding to ξ=0-0.25, it suggests that it is related to the reduction of Fe_3O_4 to FeO based on the 1:3 H_2-stoichiometry between reaction (2.6) and (2.7); while the second broader peak corresponding to a larger ξ=0.75 is related to the reduction of FeO to Fe. It is worth noting that the rate of reduction slows down with time, especially after reduction extent of 0.9, which is likely related to low fraction of FeO and impeded diffusion by partial Fe-particle sintering. We will discuss the latter in a later section.

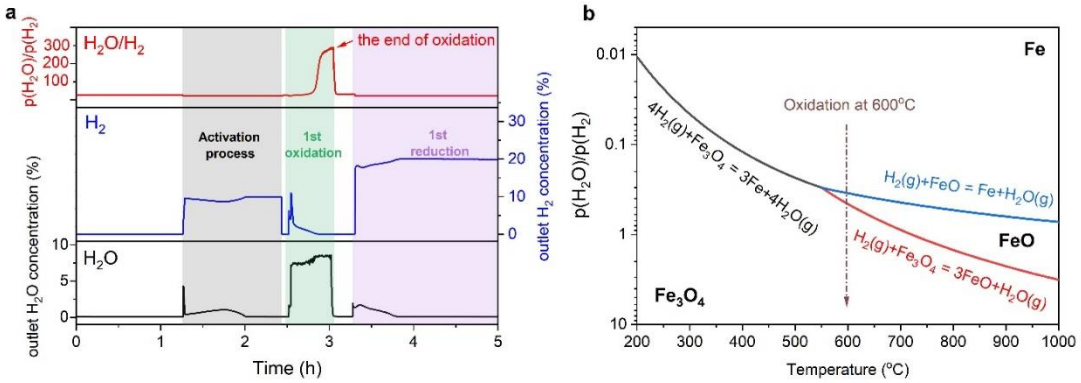

Figure 2.5 (a) The outlet H_2O and H_2 concentrations and the corresponding P_{H_2O}/P_{H_2} *vs.* time during oxidation at 600 °C; (b) thermodynamic phase stability diagram of Fe–O–H system. This plot is constructed by HSC Chemistry 6.0.

To confirm the finial FeO_x composition after oxidizing Fe by 20% H_2O (note: Fe was derived from an initial full reduction of Fe_2O_3/ZrO_2 in a pure H_2), the ratio of partial pressures of H_2O and H_2 that are in equilibrium with the formed Fe-oxide was calculated based on the outlet H_2O and H_2 concentrations measured by MS. The raw experimental results are shown in Figure 2.5a, along with Figure 2.5b that shows the calculated thermodynamic phase stability diagram of Fe–O–H system. It is evident that at all

experimental temperatures above 600 ºC and P_{H_2O}/P_{H_2} is about 220, Fe_3O_4 will be the stable oxide phase. Therefore, it is the starting oxide for our H_2-reduction kinetic study.

2.3.3 Modeling of Experimental Data

Figure 2.6a-2.6c show the grouped isotherms of the normalized Fe_3O_4 reduction extent *vs.* time from 600 to 800 ºC in different inlet H_2 concentrations. It is seen that all curves exhibit a rapid increase in the early stage of reduction, followed by a slower increase to the final plateau. As expected, the rate of conversion from Fe_3O_4 to Fe increases with reaction temperature and H_2 content. We here use the chemical-reaction controlled model discussed above to fit the data, from which the rate constant (k) *vs.* T are obtained. Figure 2.6d shows the Arrhenius plots of *k*, from which the activation energies (E_a) are found to be 24±3, 28±2, and 25±3 KJ/mol for 5%, 10% and 20% H_2, respectively. These activation energies fall within the range of the reported values [56], but it seems that E_a is less sensitive to H_2 content. The actual values of *k* and E_a along with the fitting reliability are summarized in Table C.1 of Appendix C for reference.

Figure 2.7a shows the reduction degree of pure Fe_3O_4 (derived from a pure Fe_2O_3) *vs.* time obtained at different temperatures and fixed inlet 20% H_2. Note that we here only show the results in 20%H_2 but expect the same trending in 5 and 10% H_2. Compared to the data derived from Fe_2O_3-ZrO_2 composite, the results clearly indicate a different reduction behavior. When the temperature is above 650 ºC, instead of increasing with temperature, the rate of reduction in fact gradually decreases. This could be explained by the sintering of Fe-particles, forming a dense layer limiting mass transfer (see the morphology later). Therefore, different from Fe_3O_4 derived from Fe_2O_3-ZrO_2, a diffusion-controlled model should be also considered for the case of pure Fe_3O_4 reduction

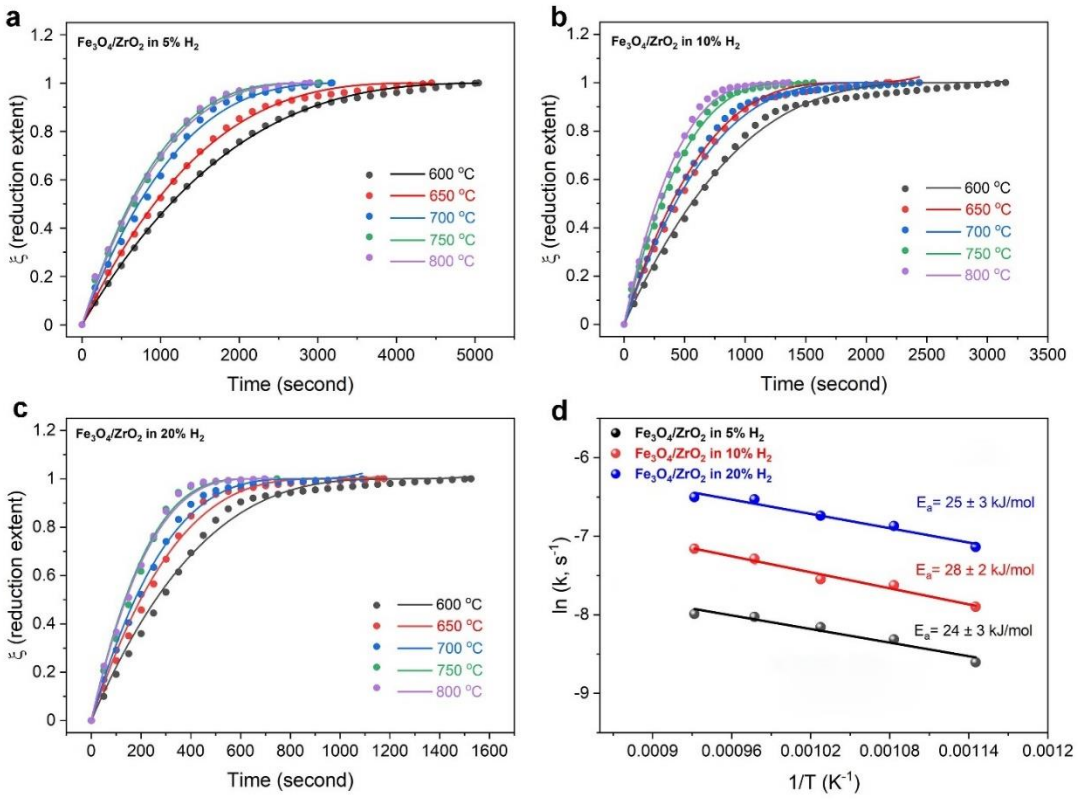

Figure 2.6 Reduction extent of Fe_3O_4 *vs.* time at 600 to 800 °C in (a) 5% H_2; (b) 10% H_2; (c) 20% H_2; (d) Arrhenius plots of reduction rate constant of Fe_3O_4 at different H_2 contents based on chemical-controlled model.

above 700 °C. The results of both chemical-controlled (600 and 650 °C) and combined chemical-and diffusion-controlled model (700~800 °C) are shown in Figure 2.7b. Clearly, the merits-of-figure of fittings are not as good as Fe_3O_4-ZrO_2 of Figure 2.7a. Fe-particles sintering, which was not considered in the modeling, is deemed the reason for the poorer fitting. Nevertheless, the rate constants derived from the chemical-controlled model increase with temperature until particle agglomerations prevail above 650 °C. Since the dense product layer formed during the reduction process prevents the inward and outward diffusions of H_2 and H_2O, respectively, a further reduction will likely be controlled by the diffusion beyond this point. Furthermore, with the increase of temperature, the sintering effect becomes more pronounced, resulting in a lowered rate constant instead. The kinetic

parameters obtained are summarized in Table C.2 of Appendix C, which shows a generally lower rate constant than that derived from Fe_2O_3-ZrO_2. Therefore, the inert ZrO_2 additive plays a beneficial role in retaining high reduction kinetics of Fe_3O_4.

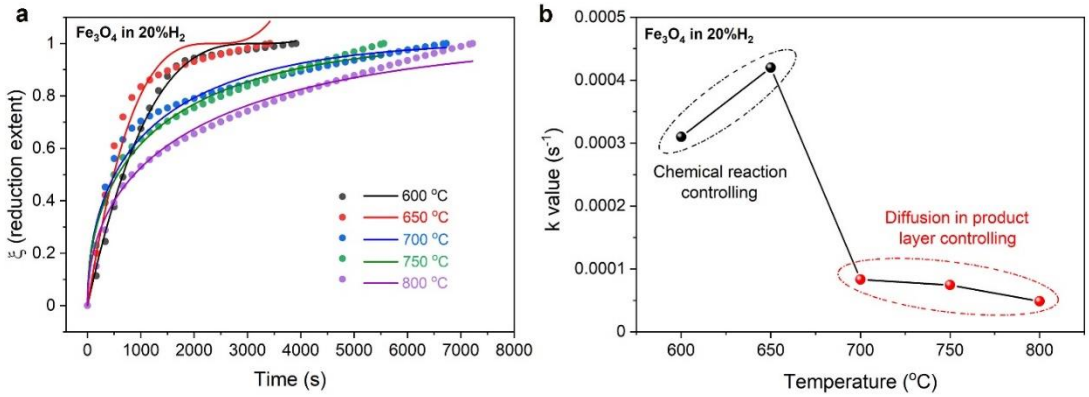

Figure 2.7 (a) Reduction extent of Fe_3O_4 derived from a pure Fe_2O_3 *vs.* time at 600 to 800 °C in 20% H_2; (b) rate constant of reduction of Fe_2O_3-derived Fe_3O_4 at different temperatures in 20% H_2.

2.3.4 Morphologies and Phases of Fe-Oxide Before and After Reduction

SEM images of the original pure Fe_2O_3 and post-tested one at different temperatures in 20% H_2 are shown in Figure 2.8, where a significant morphological change with temperature is observed. Figure 2.8a depicts the morphology of the original Fe_2O_3 powders prepared through co-precipitation and calcination at 600 °C for 5h. Nanoscale Fe_2O_3 particles are clearly seen to evenly distribute within soft agglomerates. After reduction study at 600 °C, Figure 2.8b shows a partial shrinkage with a small degree of agglomeration and some porosity.

As the temperature increases from 600 to 800 °C, Figure 2.8c-2.8f show that the surface of the sample exhibits severe agglomeration and becomes denser. A denser microstructure is evidently observed when the reduction temperature is above 650 °C, which is direct evidence for the blocked diffusion and lowered kinetic rate.

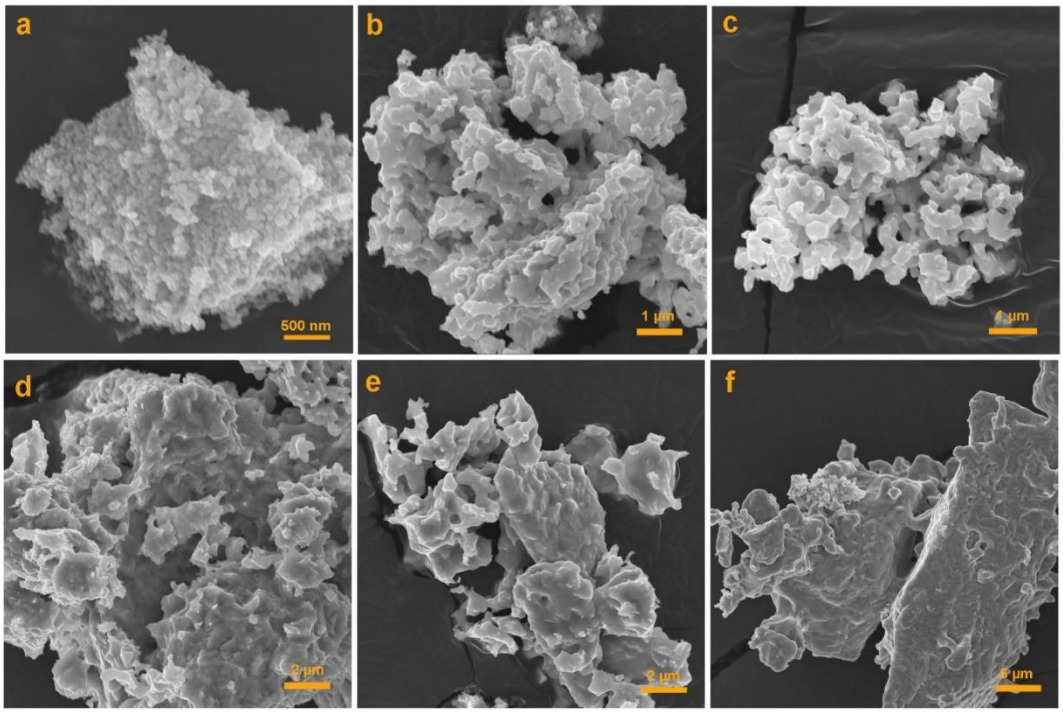

Figure 2.8 SEM images of (a) a pure Fe_2O_3 before testing; after testing in 20% H_2 at (b) 600; (c) 650; (d) 700; (e) 750; (f) 800 ºC.

In contrast, samples derived from Fe_2O_3-ZrO_2 have a different morphology after a similar reduction process. Figure 2.9a shows the morphology of Fe_2O_3-ZrO_2 powder before testing. It exhibits uniform nanoparticles like pure Fe_2O_3. After testing, Figure 2.9b-2.9f show that it still retains a nanoscale morphology. The element mapping in Figure 2.9g confirms the homogeneous distributions of Fe and Zr even in the reduced powder.

The phase compositions revealed by XRD of the pure Fe_2O_3 and Fe_2O_3-ZrO_2 composite OCs before and after the first redox cycle are shown in Figure 2.10. Both as-prepared pure and Fe_2O_3-ZrO_2 composite consist of the expected phases. For the pure Fe_2O_3 precursor, Figure 2.10a shows that the Fe-oxidation product by 10% H_2O is magnetite (Fe_3O_4) instead of hematite (Fe_2O_3) or wüstite (FeO) at 700 ºC, consistent with

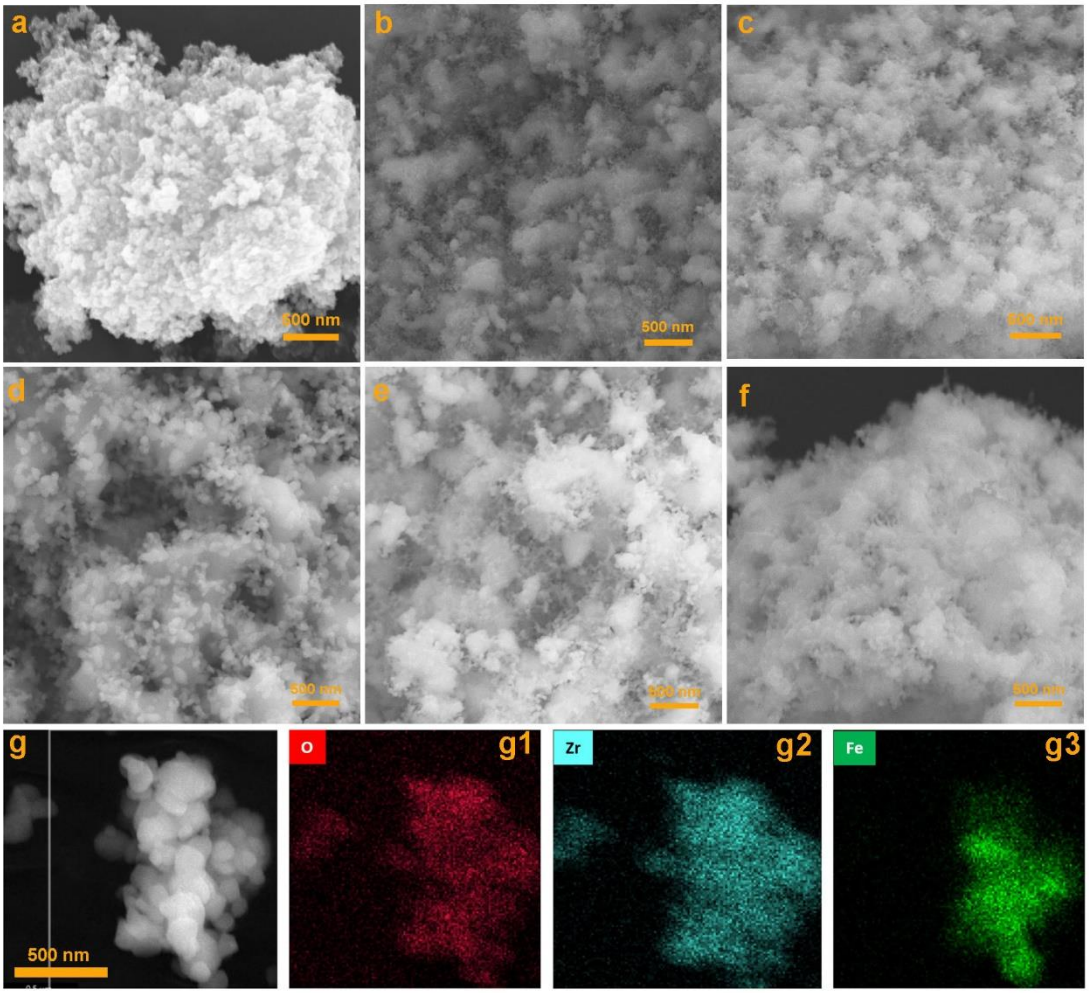

Figure 2.9 (a) SEM images of Fe_2O_3-ZrO_2 before reduction; after reduction in 20% H_2 at (b) 600 ºC; (c) 650 ºC; (d) 700 ºC; (e) 750 ºC; (f) 800 ºC; (g) elemental mapping of O, Zr and Fe after reduction.

the thermodynamic prediction (see Figure 2.5b). In the following reduction process, Fe_3O_4 is fully reduced to Fe. Thus, Fe/Fe_3O_4 is the active redox couple for CLH under this condition. Figure 2.10b shows similar phase compositions for Fe_2O_3-ZrO_2 after the first redox cycle. During the redox process, all XRD peaks of ZrO_2 remain unchanged, even though the peak at 28.2º is weak due to the high crystallinity and high content of Fe_2O_3, suggesting its chemical stability to Fe-based materials and H_2.

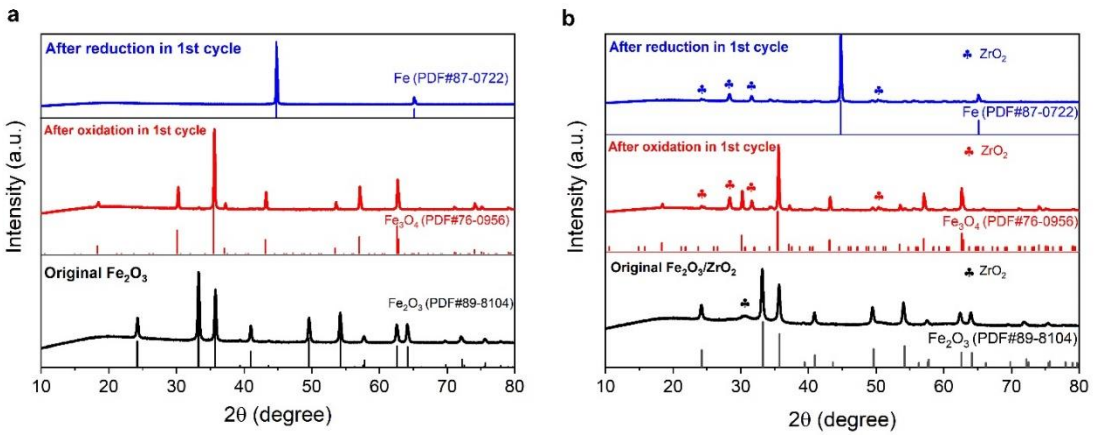

Figure 2.10 Comparison of XRD patterns of the as-prepared precursors of Fe_2O_3 (a) and Fe_2O_3/ZrO_2 (b) before and after the first oxidation in 10% H_2O and reduction in 20% H_2 at 700 °C.

2.3.5 Kinetics Process for Overall Reduction

To further provide a clearer picture of the phenomenological mechanisms of reduction of Fe_3O_4 derived from Fe_2O_3-ZrO_2, a model-free analytical approach was also adopted [55, 57]. From eq. (2.3), it can be rearranged into:

$$\ln(t) = (-\ln(A) + \ln(g(\xi))) + E_a/RT \quad (2.8)$$

By plotting ln t versus 1/T, the activation energies can be obtained at any reduction extents from the slope of a fitting line. Figure 2.11a shows the fittings at ξ =0.05 to full reduction at 600-800 °C in 20% H_2, while Figure 2.11b shows the derived E_a *vs.* ξ. According to the previous report [55], the process of reduction can be described by single-step kinetics if E_a does not vary with ξ. In this case, with increasing ξ, E_a firstly increases from 24 to 35 kJ/mol within $0.05<\xi<0.15$, then decreases to 22 kJ/mol within $0.15<\xi<0.85$, and then increases to 37 kJ/mol within $0.85<\xi<0.95$, finally decreases to 15 kJ/mol at the end of reduction. These variations reflect the changes in nucleation and growth mechanisms during the reduction process. Combined with the kinetics data and XRD results, we divide the reduction process into three steps: 1) the first stage is

attributed to the reduction of Fe_3O_4 to FeO ($0<\xi<0.25$); its high E_a implies that it might be a limiting step; 2) the second stage is a further reduction from FeO to Fe ($0.25<\xi<0.85$), during which E_a decreases with the reduction process; 3) the last stage is related to a diffusion process, during which the reduction rate slows down, as shown in Figure 2.6c, with an increased E_a. In addition, at the end of reduction period, the gradually densified Fe outer layer also presents a barrier to the reduction, resulting in a higher E_a.

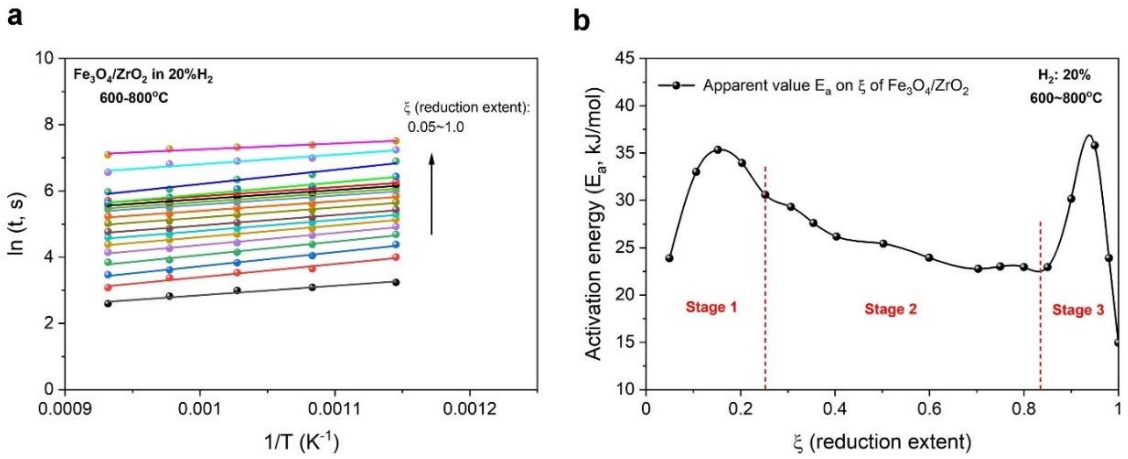

Figure 2.11 (a) Plots of ln t versus 1/T at different reduction extents and a temperature of 600-800 oC in 20% H2; (b) activation energy as a function of reduction extent (ξ).

2.4 One-Step Reduction Kinetics

2.4.1 Confirmation of the Starting Oxide for H_2-Reduction

Figure 2.12a shows the thermodynamic equilibrium phase of Fe-O-H system predicted as a function of temperature and partial pressure ratios of H_2O and H_2 (P_{H_2O}/P_{H_2}). The diagram indicates the following phase domains: Fe, FeO and Fe_3O_4. At low temperature (T < 550 °C), only metallic Fe and Fe_3O_4 are in equilibrium with H_2-H_2O gas phase,

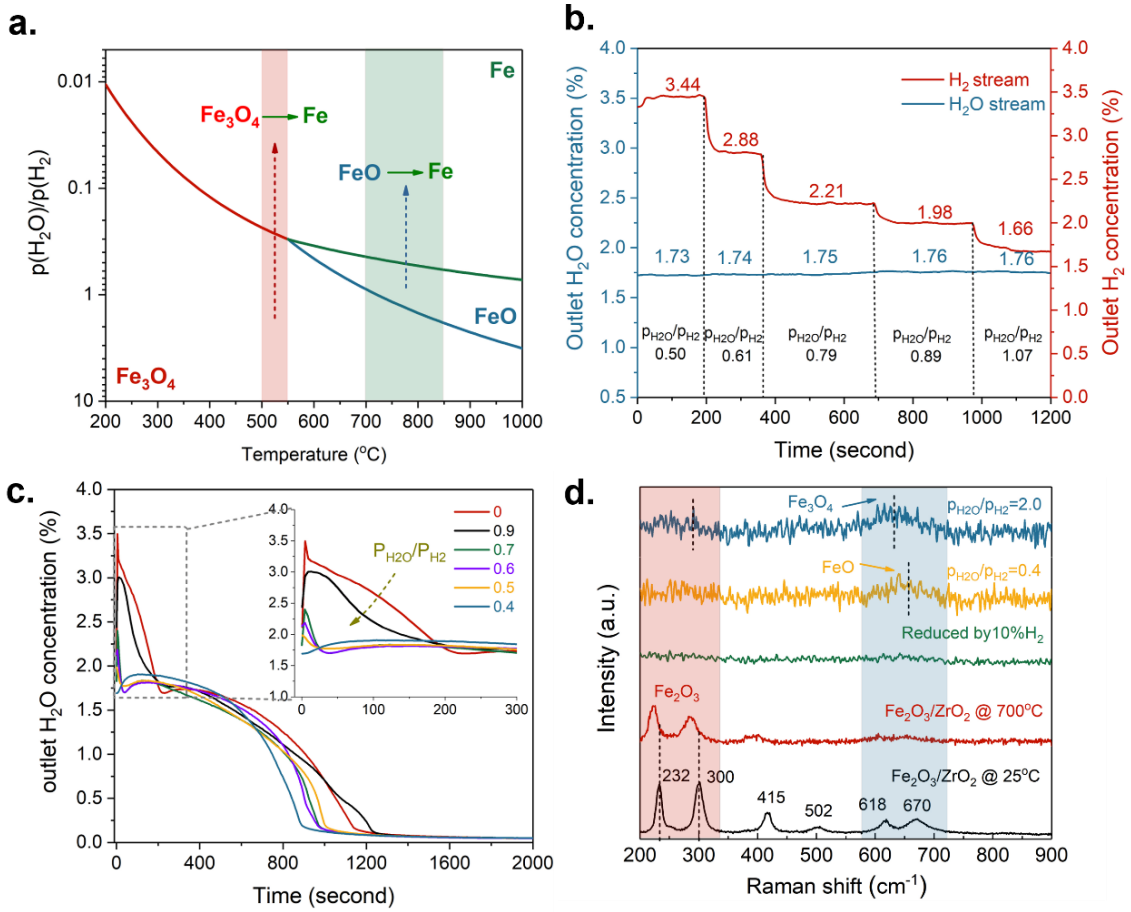

Figure 2.12 (a) Thermodynamics phase stability diagram of Fe-O-H system calculated by HSC Chemistry 6.0. (b) The ratio of H_2O and H_2 analyzed by MS corresponding to the change of H_2 flow rates. (c) The profiles of the outlet gas composition during reduction process in 10% H_2 at 700 °C for different starting states of reduction. (d) *In-situ* Raman spectra of Fe_2O_3/ZrO_2 sample in different gas environments.

meaning that Fe_3O_4 can be directly reduced into Fe by H_2. In contrast, there is an intermediate phase of FeO before Fe_3O_4 is reduced to Fe at T ≥ 550 °C. To study the kinetics of a specific one-step reduction process, the P_{H2O}/P_{H2} can be controlled for a specific temperature range to achieve a specific iron oxide, i.e., Fe_3O_4 and FeO. In this study, we study two temperature ranges of 500-550 and 700-850 °C, where Fe_3O_4 to Fe and FeO to Fe reduction reactions are prevalent. To precisely control the H_2O content, we first performed a calibration on H_2O content. Figure 2.12b shows the ratio of H_2O and H_2

in the reaction chamber analyzed by MS with a room-temperature water bubbler.

The H_2O concentration in effluent was found to be 1.75%, less than the theoretical 3.13%, which implies that the saturation of Ar by H_2O is not perfect with the bubbler. With the known H_2O content, the H_2 flow rate can be accordingly set to achieve the desirable H_2O/H_2 ratio and thus the wanted starting iron oxide phase for reduction kinetic study. Figure 2.12c shows an exemplary profile of the outlet H_2O concentration variation during the reduction process in 10% H_2-Ar at 700 ºC on a sample treated in different P_{H2O}/P_{H2} ratios, thus with different oxide phase. According to Figure 2.12a, there exists two possible iron oxide phases at 700 ºC: Fe_3O_4 and FeO, depending on the ratio of P_{H_2O}/P_{H_2}. Without H_2O, the starting iron oxide has been previously confirmed as Fe_3O_4 due to the residual oxygen in Ar by XRD (see Figure 2.10), which will have to go through FeO first before being fully reduced into Fe. Thus, the total reduction process includes two steps: Fe_3O_4 to FeO and FeO to Fe. The first hump before 200 seconds is a characteristic of such a two-step reduction process, corresponding to the two-step combined reduction kinetics. However, the main objective of this study is to obtain kinetic rate constants of one-step direct reduction such as FeO to Fe and Fe_3O_4 to Fe. As shown in Figure 2.12c, as we decrease P_{H_2O}/P_{H_2} ratio (moving from bottom up in Figure 2.12a) from 0.9 to 0.4, the first hump disappears abruptly at $P_{H_2O}/P_{H_2} \leq 0.7$, implying that starting oxide phase for reduction becomes FeO. To ensure FeO is free of Fe_3O_4, we use the data from the FeO derived from $P_{H_2O}/P_{H_2} = 0.4$ treatment for kinetic calculations.

To independently confirm the phase is what we want, we also performed *in-situ* Raman spectroscopy on sample exposed to different gases; they are shown in Figure 2.12d. The spectrum of Fe_2O_3/ZrO_2 at room temperature (black) exbibits distinct Raman

shifts at 232 (A_{1g}), 300 (E_g), 415 (E_g), 502 (A_{1g}), 618 (E_g) and 670 cm^{-1} (LO E_u), assigned to the hematite's irreducible vibrational modes [58]. While there is no obvious Raman peak for ZrO_2, its presence is confirmed by XRD pattern shown in Figure 2.10. Compared to the Raman spectra of prepared Fe_2O_3/ZrO_2 powders at room temperature, all peaks collected at 700 ºC are slightly red-shifted (red) since the lattice expansion of Fe_2O_3 at high temperatures decreases the vibration frequency of Fe-O bonds. The variations of Raman spectra with gas environments at 700 ºC are shown in Figure 2.12d, marked with green, orange, and blue. After a full exposure to 10% H_2-Ar, all Raman peaks disappeared, suggesting the Fe_2O_3 has been fully reduced to metallic Fe. After we introduced a wet H_2 with P_{H_2O}/P_{H_2} = 0.4, a wide but weak peak at 600-700 cm^{-1} appears; it can be assigned to FeO [59]. When P_{H2O}/P_{H2} is increased to 2.0, additional peak at 650 cm^{-1} corresponding to Fe_3O_4 appears [60]. Compared to the standard Raman active phonon modes for FeO and Fe_3O_4 phases [58], all of Raman peaks shows slightly red move because of the high temperature environment. The small weak peaks at 250 and 300 cm^{-1} observed at P_{H_2O}/P_{H_2}=2 and 700ºC might suggest a trace amount of Fe_2O_3 also formed under this condition.

2.4.2 Kinetics Models

The reduction process of iron oxide with H_2 usually involves a sequence of nucleation and growth steps. Johnson-Mehl-Avrami (JMA) solid-state phase transformation model has been widely used to describe such an isothermal reduction kinetics [56, 61-69]. In this model, a new phase is nucleated by germination nuclei contained in the old phase, followed by growth. The JMA equation relates the transformed fraction at a constant temperature T and reaction time t. Once ξ is determined, the overall kinetic rate *k(T)* can

be calculated by:

$$\xi(t) = 1 - exp[-k(T)t^n] \tag{2.9}$$

where t is the reaction time, ξ is the reduction extent, $k(T)$ is the Arrhenius rate constant, which can be given by $k(T) = A * \exp(-\frac{E}{RT})$ and n is the Avrami exponent that depends on the mechanism of nucleation and growth process [70]. Generally, $n = \lambda + \beta$, where λ is the dimensionality of growth, $\lambda = 1, 2\ or\ 3$; and β depends on the nucleation process ($0 < \beta < 1$, $\beta = 0$ represents instantaneous nucleation and $\beta = 1$ means a very slow nucleation rate).

Using the logarithmic form and rearrangement of eq. (2.9), Sharp-Hancock equation can be derived [64]:

$$ln[-\ln(1-\xi)] = nln(t) + \ln(k) \tag{2.10}$$

The local $n(\xi)$ can be calculated by differentiating eq. (2.10) into:

$$n(\xi) = \frac{\partial \ln(-\ln(1-\xi))}{\partial \ln(t)} \tag{2.11}$$

In addition, during the iron oxide reduction process, the reaction rates can be also expressed by:

$$\frac{d\xi}{dt} = k(T) * f(\xi) \tag{2.12}$$

where $f(\xi)$ is the integration reaction model function. For the reduction kinetics under isothermal conditions, eq. (2.12) can be integrated into:

$$g(\xi) = \int_0^{\xi} \frac{d\xi}{f(\xi)} = kt = A * exp((-\frac{E_a}{RT})t \tag{2.13}$$

where $g(\xi)$ is the function of the integration reaction model function. By taking the logarithm and rearranging eq (2.13), one can get:

$$\ln(t) = \left(-lnA + lng(\xi)\right) + \frac{E_a}{RT} \tag{2.14}$$

where t is the time for a specific reduction extent. By plotting $\ln(t)$ versus 1/T based on the eq. (2.14), the activation energies E_a can be obtained at different reduction extents.

2.4.3 Reduction Kinetics of Fe_3O_4 to Fe

The isothermal kinetics of Fe_3O_4 to Fe reduction process in H_2-Ar was determined by measuring the variations of H_2O content in the effluent and data processing by JMA model. The change in H_2O concentration *vs.* time during the reduction process is due to oxygen removal from iron oxide. Figure 2.13a, 2.13c and 2.13e show the outlet H_2O content variations with time-on-reduction from 500 to 550 ºC under different inlet H_2 concentrations, while Figure 2.13b, 2.13d and 2.13f show the corresponding normalized degree of Fe_3O_4 reduction *vs.* time. It is evident that the reduction kinetics is affected by both of temperature and H_2 concentrations. Compared to multiple step reduction process in above, there is nearly no reduction peak related to Fe_3O_4 to FeO reduction, suggesting the one-step reduction of Fe_3O_4 to Fe has been achieved under this condition.

The results also show that the H_2O production is faster in the early stage than the later one. To determine the kinetic rate constant, JMA model was applied to fit the experimental data, see lines in Figure 2.13b, 2.13d and 2.13f. The sigmoidal profile of these kinetic plots could be analyzed by separating three periods based on JMA phase transformation model [64]: (1) induction period ($0 < \xi < 0.05$); (2) acceleratory region ($0.05 < \xi < 0.8$); (3) decelerating period and completion($0.8 < \xi < 1.0$); The induction period tends to be dominated by nucleation events, the acceleratory region can be attributed to the growth process and the decelerating region results from the fusion of Fe and thus affecting the diffusion path. At a given temperature, values of k, n and E are

extracted from the fitting results, which are summarized in Table C.3 in Appendix C. The n value is found to be constant at 1.45, indicating that a 1-diamensional nucleation and growth process for the reduction. The Arrhenius plots of k are shown in Figure 2.14

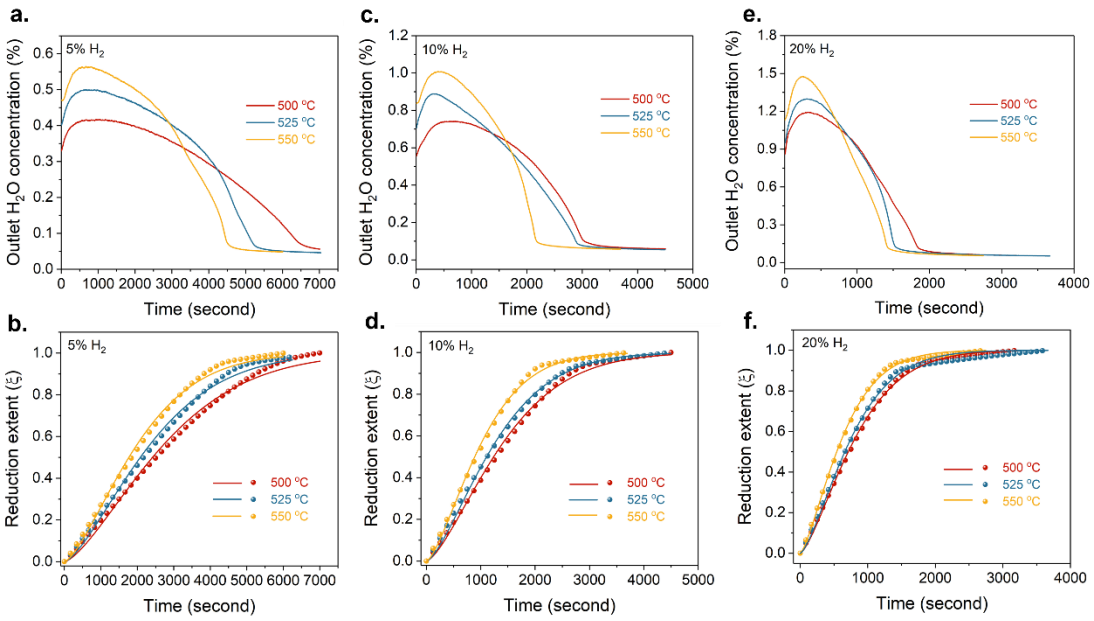

Figure 2.13 Reduction kinetic data: profiles of outlet water concentration changes during reduction process and corresponding reduction extent (dot) of Fe_3O_4 versus time and JMA reduction model fitting curves (line) at 500 to 550 °C in (a and b) 5% H_2, (c and d) 10% H_2, and (e and f) 20% H_2.

from which E_a are obtained to be 47.6±2.8, 50.6±5.6 and 40.1±2.3 kJ mol^{-1} for 5, 10 and 20% H_2, respectively. The weak dependence of E_a on H_2 concentration infers that energy barrier of the reduction process may not be mass transfer limited.

To evaluate the order of solid-state reaction rate for the one-step reduction, Sharp-Hancock plots of ln(-ln(1-ξ)) *vs.* ln (t) based on the actual experiment data are shown in Figure 2.15a at 500 to 550 °C in 10% H_2. There are apparently three distinct stages with different Avrami exponents n in the whole conversion process. At the beginning of the conversion, the average of n value is ~ 1.12; at the medium state, the n increases to ~ 1.67; at the final stage, n decreases to 0.89. It is worth noting that when the reduction

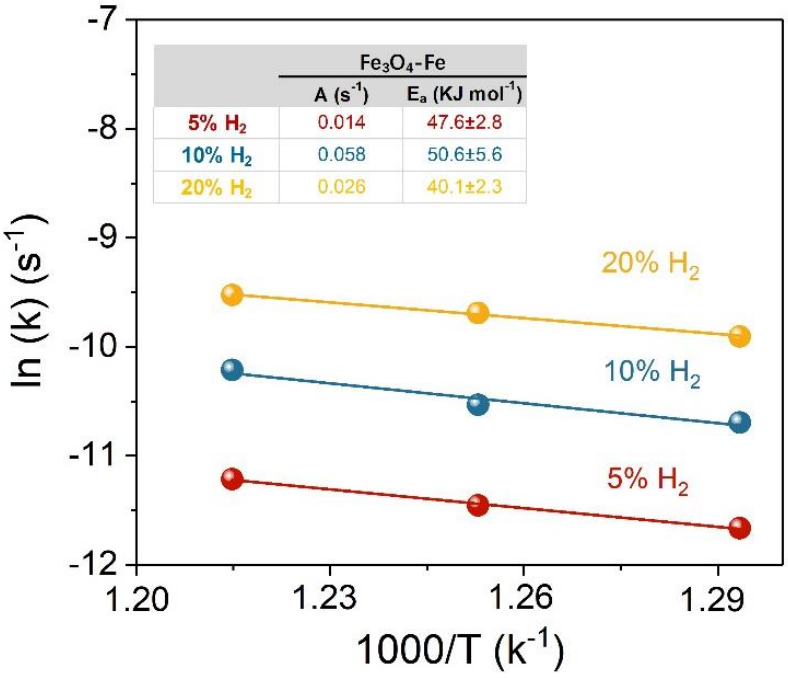

Figure 2.14 Arrhenius plots of rate constant of Fe_3O_4 to Fe reduction derived from the JMA phase transformation model.

extent is close to 1, n trends to be infinite, which is attributed to the boundary conditions of the mathematical function ($\xi \neq 1$ in eq. (2.11)). The variation of Avrami exponent n during the reduction reaction indicates that there are different dominating mechanisms in each reaction stage. To explore local exponent n at different reduction extent, using eq. (2.11), local exponent n *vs.* reduction extent ξ are plotted and shown in Figure 2.15b. At the beginning of reaction, the n-value increases and reaches a maximum value, suggesting a decrease in the nucleation rate, which agrees with the results in Figure 2.15a. At the end of reduction, the n falls below 1, implying the reduction process becomes diffusion- controlled, possibly due to the blocking effect of partially sintered Fe particles. To further provide a clearer picture of the mechanisms, with eq. (2.14), the plots of ln (t) *vs.* 1/T obtained at ξ=0.01 to full reduction (ξ=1) from 500 to 550 °C in 10% H_2 are shown in Figure 2.15c. For a given reduction extent ξ, E_a can be obtained from the

slope of each line. Figure 2.15d plots the derived E_a *vs.* ξ, which shows E_a decreases with reduction extent. This trending can be explained according to the crystal nucleation and growth theory by the fact that E_a required during nucleation is higher than that for growth [68]. Therefore, the reduction kinetics of Fe_3O_4 to Fe follows the nucleation and growth model.

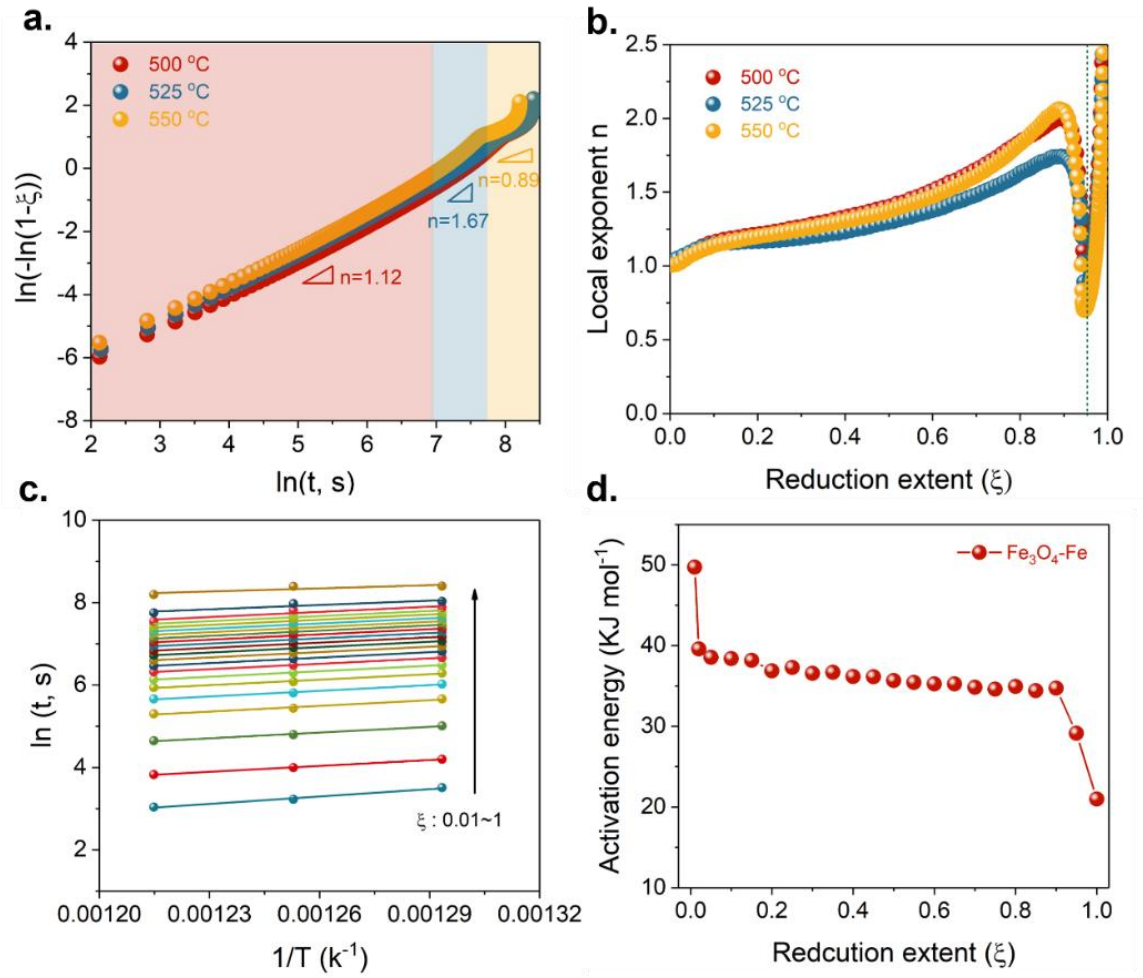

Figure 2.15 (a) Sharp-Hancock plots of ln(-ln(1-ξ)) *vs.* ln (t) based on the data at 500 to 550 °C in 10% H_2. (b) local exponent n values *vs.* reduction extent at 500 to 550 °C in 10% H_2. (c) ln (t) *vs.* 1/T with different reduction extents at 500 to 550 °C in 10% H_2. (d) Activation energy as a function of the reduction extent for the conversion of Fe_3O_4 to Fe.

To observe the change in morphologies of the specimen before and after reduction, SEM images of the original Fe_2O_3/ZrO_2 before and after reduction at different

temperatures were collected; they are shown in Figure 2.16. Figure 2.16a is a typical SEM image of the as-prepared Fe_2O_3/ZrO_2 before reduction, consisting of uniform spherical nanoparticles with an average particle size of 30 nm. After reduction at 500 ^oC to 550 ^oC, however, Figure 2.16b-2.16d show some degree of agglomerations with an average particle size of 200 nm. But there are still some nanoparticles (few nanometers) visibly anchored on the surface of sintered larger particles. The elemental mapping on the reduced sample shown in Figure 2.16e-2.16i cannot conclusively identify the real compositions of these nanoparticles due to the resolution issue of EDS. In other words, these nanoparticles could be pure Fe or Fe-oxide.

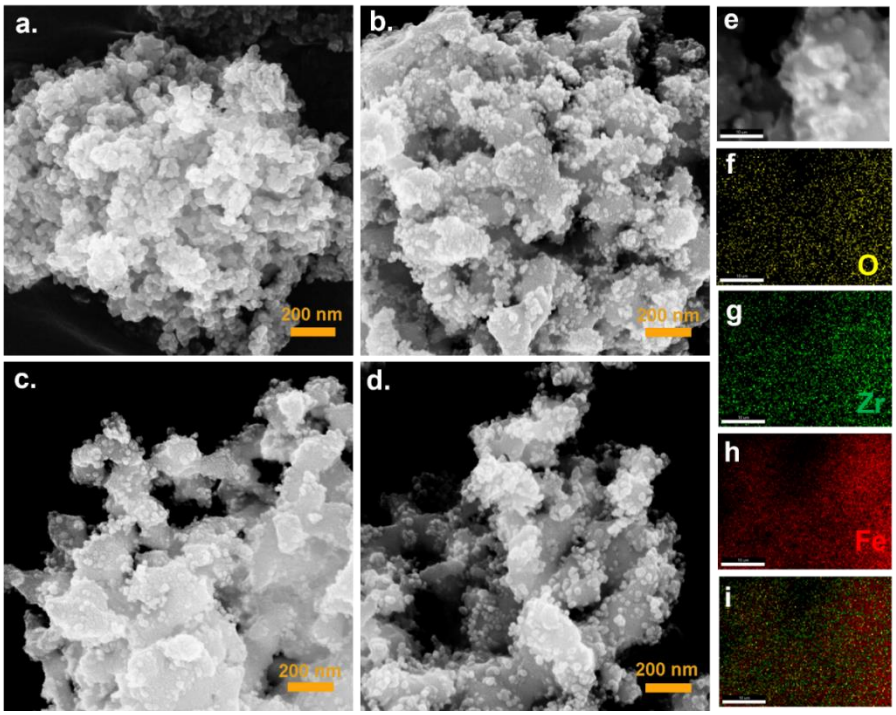

Figure 2.16 SEM images of (a) pristine Fe_2O_3/ZrO_2 before reduction; after reduction in 10% inlet H_2 at (b) 500, (c) 525 and (d) 550 ^oC. (e) Area of element mapping of reduced sample at 550 ^oC for (f) O, (g) Zr, (h) Fe and (i) overlay of different elements.

2.4.4 Reduction Kinetics of FeO to Fe

The kinetics of FeO to Fe reduction taking place above 550 ^oC is equally important to

that of Fe_3O_4 to Fe from both scientific and engineering perspectives. However, there are scarce reports in the literature dealing with the kinetics of this single-step reduction. We here apply similar method to the study of Fe_3O_4-Fe reduction. The starting FeO was obtained by controlling the P_{H_2O}/P_{H_2} as described above. The collected raw data and converted reduction extent ξ are shown in Figure 2.17a-2.17f. The FeO-Fe one-step reduction can be confirmed by the single reduction peak in Figure 2.17a, 2.17c and 2.17e. With the JMA model, the fitting results are plotted as lines in Figure 2.17b, 2.17d and 2.17f. The extracted n, k and E_a values are summarized in Table C.4 of Appendix C. The average n value is close to 1.45, indicating that a 1-diamensional nucleation and growth process. The Arrhenius plots of k is shown in Figure 2.18, from which E_a are obtained to be 29.0±5.6, 25.8±1.9 and 23.9±4.0 KJ mol^{-1} for 5, 10 and 20% H_2, respectively. The level of E_a has a weak dependence on H_2 concentration and is smaller than that Fe_3O_4-Fe reduction. Compared to the Fe_3O_4-Fe reduction, the rate constant of FeO-Fe reduction is roughly two orders of magnitude higher than that of Fe_3O_4-Fe reduction, largely due to the higher temperatures and possibly lower oxygen content or kinetics-friendly defects in FeO.

To further investigate the one-step FeO-Fe reduction mechanisms, n value describing the phase transformation is discussed. Sharp-Hancock plots for the FeO-to Fe reduction are shown in Figure 19a. It is evident that the Avrami exponent n for the overall reduction process is not a constant. At the beginning of the reduction, n value is averaged at 1.09; in the intermediate stage, n increases to ~ 1.63; in the final stage, n decreases to 1.01. The variations of Avrami exponent n with the extent of reduction ξ imply that the dominating mechanisms are changing with reaction stages. To explore local exponent n at

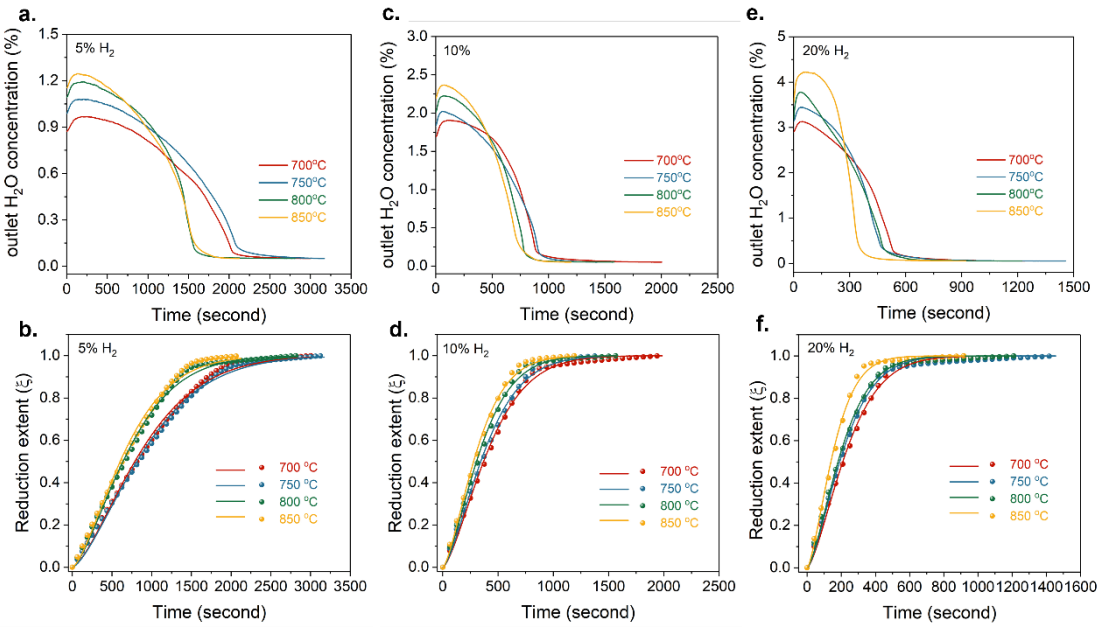

Figure 2.17 Profiles of outlet H_2O concentration during reduction process and corresponding reduction extent (dot) *vs.* time with JMA model fitting curves (line) from 700 to 850 °C in (a and b) 5% H_2, (c and d) 10% H_2, and (e and f) 20% H_2.

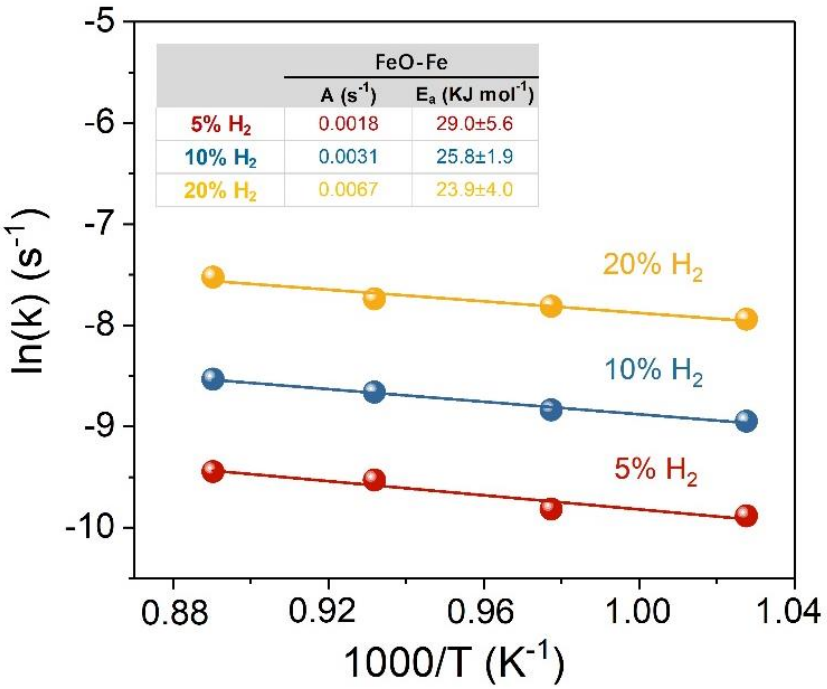

Figure 2.18 Arrhenius plots of rate constant of FeO to Fe reduction derived from the JMA phase transformation model.

different reduction extent ξ, using eq. (3), we plot local exponent n values with reduction extent ξ in Figure 2.19b. Like the Fe_3O_4-Fe reduction shown in Figure 2.15b, at the beginning of transformation, n increases to 2.5, corresponding to a growth mechanism changing from 1D to 2D, but decreases to ~ 0.5 at the end of reduction, suggesting a decrease in the nucleation and growth rate. This trending can be attributed to the diffusion limitation induced by the partial sintering of Fe particles at high temperatures. To further provide a clearer picture of the mechanisms, using eq. (6), we plot ln (t) *vs.* 1/T in Figure 2.19c at ξ = 0.05 to full reduction (ξ = 1) at 700-850 ºC in 10% H_2. At a given reduction extent ξ, E_a can be obtained from the slope of a fitting line for the plots. Figure 2.19d shows the derived E_a *vs.* ξ. The results clearly indicates that E_a decreases with reduction, which can be explained by the fact that E_a required during the initial nucleation is higher than that of growth. But in the mediate stage, E_a keeps roughly constant at ~ 17 kJ mol^{-1}, implying the nucleation and growth of FeO-Fe reduction becomes homogeneous.

The morphologies of the specimen after reduction at high temperatures are shown in Figure 2.20 of SEM images. After reduction at 700 to 850 ºC, some agglomerations are observed in comparison to the original morphologies (Figure 2.16(a)) of Fe_2O_3/ZrO_2 before reduction as well as those exposed to intermediate temperature reduction (Figure 2.16b-2.16d). These agglomerations could result in a slowed kinetics at the final state of reductions even though ZrO_2 as sintering inhibitor is present and has a homogenic distribution (Figure 2.20e-2.20f). However, compared to ZrO_2-free iron oxide reduction, the sintering is much marginal.

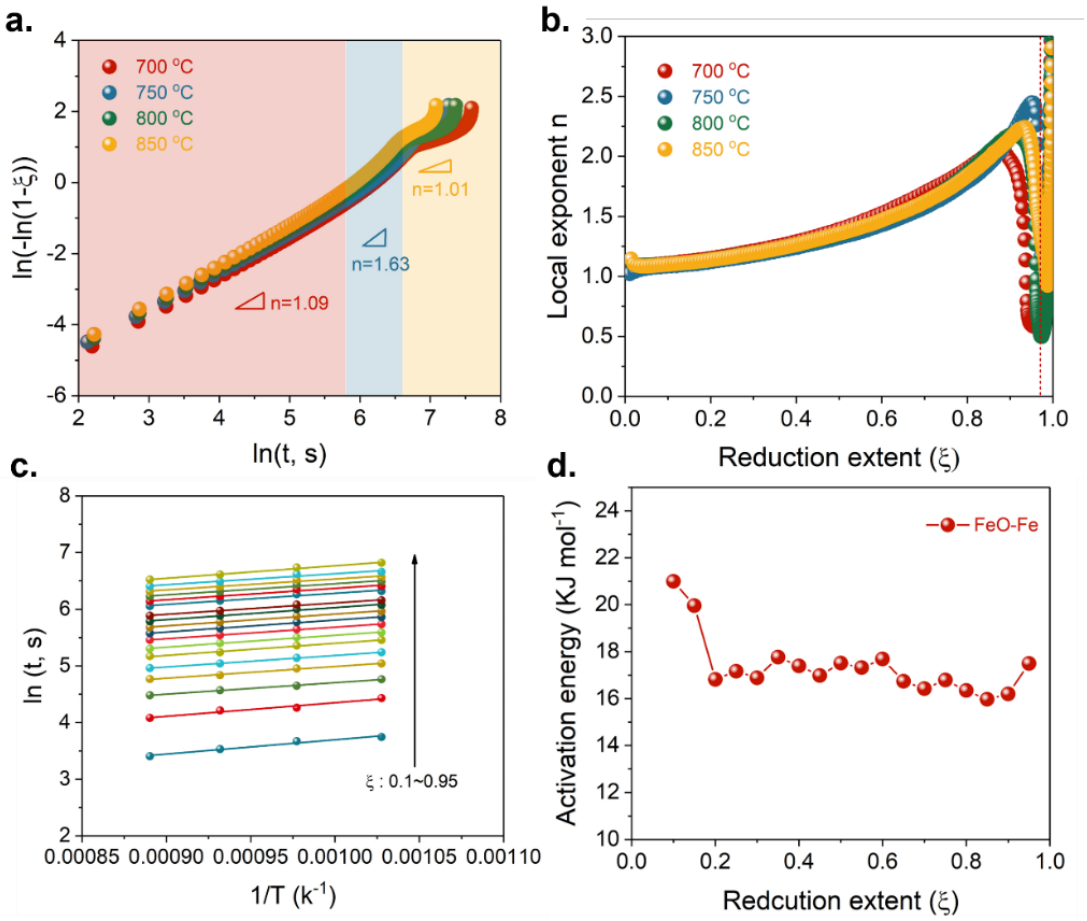

Figure 2.19 (a) Sharp-Hancock plots of ln(-ln(1-ξ)) versus ln (t) based on the measurement data at 700 to 850 °C in 10% H_2. (b) local exponent n *vs.* reduction extent at 700 to 850 °C in 10% H_2. (c) plots of ln (t) *vs.* 1/T with different reduction extents at 700 to 850 °C in 10% H_2. (c) Activation energy *vs.* reduction extent for the conversion of FeO to Fe.

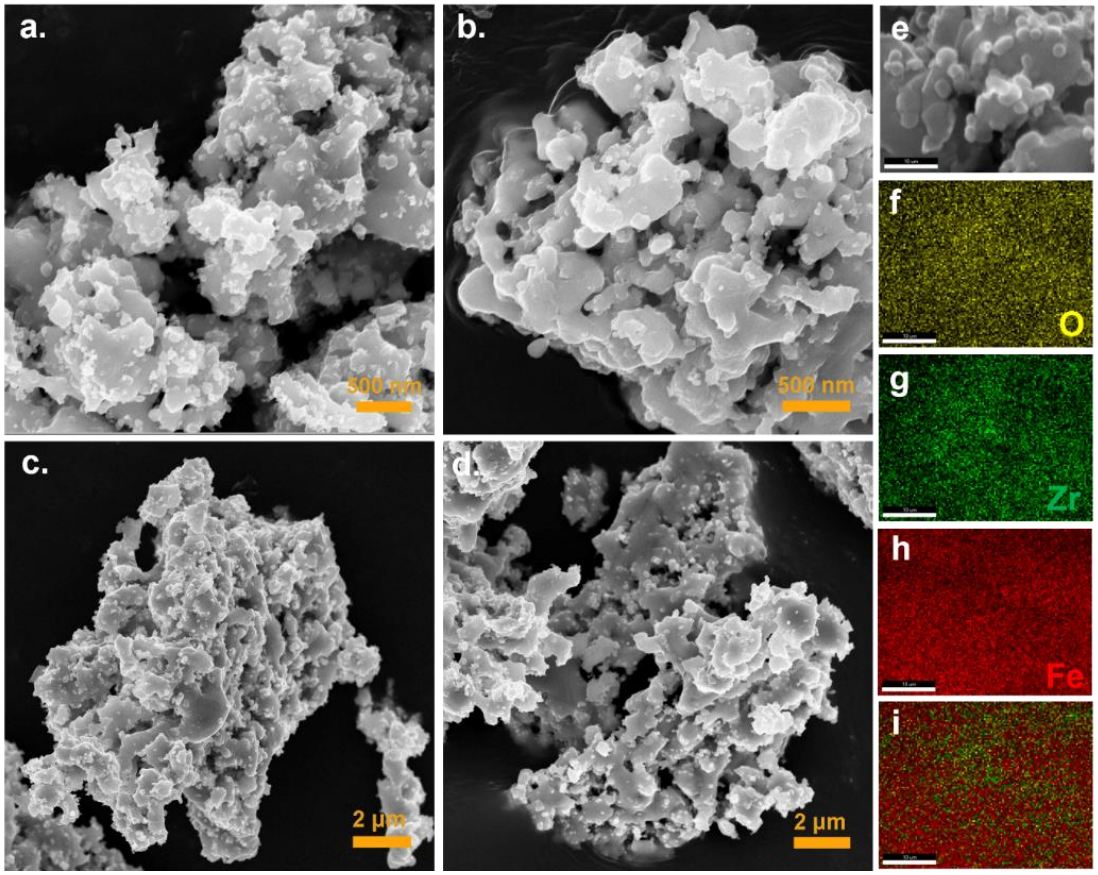

Figure 2.20 SEM images of Fe_2O_3/ZrO_2 after reduction in 10% inlet H_2 at (a) 700, (b) 750, (c) 800 and (d) 850 °C. (e) area of element mapping of reduced sample at 700 °C for (f) O, (g) Zr, (h) Fe and (i) overlay of different elements.

2.5 Summary

In this chapter, the overall and one-step reduction kinetics of Fe_3O_4 derived from Fe_2O_3/ZrO_2 have been investigated by MS in a temperature range of 500-850 °C and H_2 content of 10-20%. The work first demonstrates the need for ZrO_2 to achieve stable performance and provides key kinetic data for engineering design of SOIAB systems in the future. For the multi-step reduction in Fe_3O_4/ZrO_2, we show that the reduction of Fe_3O_4 to Fe follows two consecutive steps and can be reasonably described by phenomenological chemical-controlled and diffusion-controlled kinetic models. In addition, the desired iron oxide, Fe_3O_4 or FeO, has been formed *in situ* from fully reduced

iron particles by precisely controlling the ratio of H_2O and H_2 concentrations and temperature. With the desired iron oxide, the reduction kinetics of one-step iron oxide to iron was studied by measuring H_2O content *vs.* time with an on-line MS and phenomenological modeling. It is found that the reduction degree of the two one-step reduction processes follows nicely the JMA phase transformation model, revealing three stages during the reduction, in which the E_a of the nucleation is faster than the growth. The kinetics of FeO-to-Fe reduction exhibits two orders of magnitude higher kinetic rate constant than that of Fe_3O_4-to-Fe counterpart with half the activation energy.

CHAPTER 3

IMPROVING THE ELECTROCHEMICAL PERFORMANCE OF REVERSIBLE SOLID OXIDE FUEL CELL

Qiming Tang, Nansheng Xu, Yongliang Zhang, and Kevin Huang, "Advancing Intermediate Temperature Solid Oxide Iron-Air Battery for Seasonal Long Duration Energy Storage" to be submitted.

3.1 Introduction

Reversible Solid Oxide Fuel Cell (RSOFC) is a significant component in SOIAB, which functions as the electrical functioning unit. During discharging, RSOFC can run in the fuel cell mode to convert H_2 produced from the oxidation of iron in the ESU to electricity. During charging, it can operate effectively in electrolysis modes to electrolyze H_2O produced by the reduction of iron oxide to H_2 which further feeds the reduction reaction in the ESU. Given that the advancements in SOIAB are significantly influenced by the designs of RSOFC, in this chapter, we demonstrate that the performance of RSOFC can be significantly improved by optimizing electrolyte, electrodes, and testing fixture, resulting in a SOIAB with high stability and high round trip efficiency.

3.2 Experimental Methods

3.2.1 Materials Preparation

Iron bed materials: the Fe-bed (the energy storage material) is a mixture of Fe_2O_3 and ZrO_2. It was prepared by a co-precipitation method. Briefly, the stoichiometric solutions

of $Fe(NO)_3$•$9H_2O$ (≥99.999%, Sigma-Aldrich) and $ZrO(NO)_2$•xH_2O (≥99.999%, Alfa-Aesar) in a molar ratio of Fe:Zr=85:15 were first dissolved in deionized water separately. Then the two solutions were mixed in a beaker with a cation concentration of 0.1 M. The resultant clear orange solution was then added dropwise to an $(NH_4)_2CO_3$ (Sigma-Aldrich) solution bath under a constant stirring. To ensure a full precipitation of all cations in the solution, the molar ratio of $(NH_4)_2CO_3$ and M^{n+} (M= Zr and Fe) was kept as $n(NH_4)_2CO_3$:nM^{n+}=2.5:1. The resultant brownish precipitate was then left in the solution for 20 h with continuous stirring. Finally, the aged suspension was filtered and washed several times with ethanol, dried overnight at 80 ºC and calcined in air at 600 ºC for 5h to yield the final product.

$La_{0.8}Sr_{0.2}MnO_3$ (LSM)/$(Bi_{0.75}Y_{0.25})_{0.93}Ce_{0.07}O_{1.5}$ (BYC) OE: The LSM/BYC composite OE was prepared by combustion method using nitrates as the metal precursors. Briefly, for LSM preparation, stoichiometric amounts of $La(NO_3)_3 \cdot 6H_2O$ (Sigma-Aldrich), $Sr(NO_3)_2$ (Sigma-Aldrich) and $Mn(NO_3)_2 \cdot 4H_2O$ (Sigma-Aldrich) were dissolved into 500 mL 0.2 M citric acid (CA, Sigma-Aldrich) solution with a molar ratio of metal ions:CA=1:2. Then 10 mL nitric acid (70%, Sigma-Aldrich) solution was added into the mixture solution under stirring. The pH of the solution was then adjusted to ~ 6 with ammonia (28%-30%, Sigma-Aldrich). Finally, the transparent solution was heated in an oven at 240 ºC until auto-combustion. The obtained powders were then broken up and calcinated at 900 ºC for 5h. The BYC powders were prepared by a similar process with $Bi(NO_3)_3 \cdot 5H_2O$ (Sigma-Aldrich), $Y(NO_3)_3 \cdot 6H_2O$ (Sigma-Aldrich), and $Ce(NO_3)3 \cdot 6H_2O$ (Sigma-Aldrich) as the metal precursors, except the molar ratio of the metal ions to CA is 1:1.5 and the calcination temperature is 700 ºC.

3.2.2 Fabrication of Hydrogen Electrode (HE)-Supported Electrolyte

Co-pressing method: A mixture of NiO (J.T. Baker) and $(ZrO_2)_{0.89}(Sc_2O_3)_{0.1}(CeO_2)_{0.01}$ (ScSZ) (Daiichi Kigenso Kagaku Co. Ltd., Japan) with a weight ratio of 60:40 was ball-milled for 4 hours in ethanol with zirconia balls. Then the slurry was dried overnight at 80 ºC. The dried powders, mixed with 2 wt.% carbon (Fisher Chemical) as a pore former and 3 wt.% polyvinyl butyral (PVB, Butcar® B-98, Sigma) as a binder, were first gently pressed in a die of 1 inch in diameter. Then a layer of ScSZ powders was distributed uniformly on top of the pressed HE with a sieve, followed by co-pressing with the HE substrate into a bi-layer structure. Finally, the pellet was sintered at 1350 ºC for 5 hours and then polished to ~ 400 μm thickness. The thickness of the ScSZ electrolyte is ~45 μm with a diameter of 0.8 inch.

Dip-coating method: The HE-substrate was firstly prepared by the above method. Briefly, NiO, ScSZ and carbon powders with a weight ratio of 6:4:3 were ball-milled for 4 hours in ethanol with ZrO_2 balls. Then the slurry was dried overnight at 80 ºC. The dried powders were then fully mixed with 5 wt.% PVB in acetone with an agate mortar, followed by pressing into pellets of ϕ1 inch and partially sintering at 900 ºC for 2h to achieve enough strength. The HE functional layer was deposited by dipping the HE pellet into a slurry containing NiO:ScSZ=60:40 (wt.%) mixture with a 10 wt.% carbon for 15 s. Then the pellet was pull out of the suspension and dried in an oven for 10 min. The pellet was subsequently sintered at 800 ºC for 2h, after which a thin layer of ScSZ electrolyte was deposited on top of the functional layer by the same dip-coating technique. The recipe of the electrolyte slurry is similar to the functional layer but without NiO. The HE, functional layer and electrolyte triple-layers were finally co-sintered at 1350 ºC for 5h.

The final product was ground down to ~400 μm thickness. The thicknesses of the ScSZ electrolyte and HE functional layer are both ~10 μm with a diameter of 0.8 inch.

3.2.3 Infiltrating GDC Nanoparticles into HE Substrate

$Gd_{0.2}Ce_{0.8}O_2$ (GDC) nanoparticles were infiltrated into the NiO-ScSZ HE substrate to improve the HE performance. To do so, 0.5 M nitrate solutions of GDC precursors were prepared by dissolving stoichiometric amount of $Gd(NO_3)_3 \cdot 6H_2O$ (Sigma-Aldrich) and $Ce(NO_3)_3 \cdot 6H_2O$ (Sigma-Aldrich) in a distilled water with 20 vol.% ethanol. Ethylene diamine tetraacetic acid (EDTA, Sigma-Aldrich) and citric acid (CA, Sigma-Aldrich) as a surfactant and chelating agent, respectively, dissolved into a diluted ammonia was then added into the GDC precursor solution. The pH of the solution was carefully adjusted to 8. The molar ratio of CA to EDTA to metal ions was kept at 2:1:1. After infiltration, the NiO-ScSZ/ScSZ half-cell was fired in air at 500 ^oC for 1h to decompose metal nitrates into their respective oxides. The loading of GDC was controlled by the number of infiltration and determined based on the mass change before and after infiltration.

3.2.4 Single Cell Fabrication

Two types of cells were fabricated in this work to examine the battery performance: (i) HE-supported full cell and (ii) electrolyte-supported symmetrical cell. For the HE-supported full cell, OE was made by screen printing the OE ink on top of the ScSZ electrolyte surface. The ink consists of a mixture of LSM, BYC and a V-006 binder (Columbia International) in a weight ratio of LSM:BYC:V-006 = 40:60:150. After printing and drying, the cell is calcined at 800 ^oC for 2h to make the final cell. The effective area of the cathode electrode is 1.4 cm^2, and the silver mesh and gold paste were used as current collectors for both OE and HE.

For the electrolyte-supported symmetrical three-electrode cell, the ScSZ electrolyte with a thickness of 200 μm was made by tape casting method. The same cathode as the full cell was screen-printed symmetrically on both sides of the ScSZ electrolyte and then fired at 800 ^{o}C for 2 hours. To make the third reference electrode, a gold wire was wound and fixed by gold paste along the circumference of the electrolyte pellet.

3.2.5 Battery Cell Assembly and Testing

For a typical battery testing, a total of 86 mg of Fe-bed material (with 56 mg Fe_2O_3 and 32 mg ZrO_2) was loaded into the chamber of battery holder shown in Figure 3.2. The use of ZrO_2 is to mitigate Fe-particles from sintering during operation. Then, the RSOFC was placed into the grove of the holder with the HE substrate facing down. A layer of glass slurry consisted of glass powder (from Schott GM31107) mixed with binder was then applied along the perimeter between the cell and holder, see Figure 3.2d of the assembled battery. The current collection wires on the HE-side were carefully routed through an insulating glass ring and the glass layer to avoid short circuiting with the metal holder.

The electrochemical performance of the battery was tested using a Solartron Multichannel system (model 1470e) in conjunction with a Solartron 1255 frequency response analyzer. The battery was first heated in the air from room temperature to 680 ^{o}C and held for 30 min to melt the glass and achieve gas tightness. Then, the temperature was decreased to 550 ^{o}C for testing. A 5% H_2/N_2 at 50 cm^3/min was first introduced into the HE-chamber for 30 minutes to purge the residual air, then switched to pure H_2 through a room temperature water bubbler to reduce the HE and Fe-bed into their metallic states. The open-circuit voltage (OCV) of the battery cell was constantly monitored and used to judge the completion of the reduction process. Once it is done, the

initial V-I curves and EIS of the RSOFC were first measured under OCV in flowing 3% H_2O-H_2. Then the H_2 outlet and inlet valves were closed in sequence and the OCV was monitored until it reached the theoretical potential of 1.067 V (for Fe-Fe_3O_4 redox couple at 550 ^oC). Now the battery is ready for discharge/charge cycling. The MultiStat software is used for collecting data and performing data analysis. The rate performance, utilization of iron bed (U_{Fe}) and stability were systematically carried out based on the protocol listed in Table D.1 in Appendix D. The cutoff voltages for discharge and charge are set at 0.8 and 2.0 V, respectively.

3.2.6 Materials Characterization

The phase compositions of the prepared Fe_2O_3/ZrO_2 composite, LSM and BYC were examined by X-ray diffraction operated at a scan rate of 2^o min^{-1} from 10 to 80^o using Rigaku D/MAX-2100. The morphologies of the Fe-bed materials and battery cell components were examined by a field emission scanning electron microscope (FESEM) (Zeiss Gemini500) with Energy Dispersive X-Ray Spectroscopy (EDS) for elemental mapping analysis. A high-resolution transmission electron microscope (HRTEM, HITACHI H-9500) and scanning transmission electron microscope (STEM, HITACHI SU9000) was also used to examine the infiltrated GDC nanoparticles. The focused-ion-beam technique (FIB, Hitachi NB-5000) was used to prepare TEM samples.

3.3 Battery Fixture Design

Entire close environment is crucial for battery system which demands a good gas tightness in battery fixture. In this new type of iron-air battery, the combination of RSOFC and CLH production unit in a close system directly achieves an effective storage for hydrogen, where the discharged/charged process completes via

consuming/reproducing hydrogen by metal/metal oxide redox couples. Here, a new battery testing fixture was designed which is featured by a grove on the cross-section at the open-end of the HE-chamber (OD 1.25” and ID 0.5”), see Figure 3.1a and b. The diameter (ϕ 0.9”) of the grove is slightly larger than the diameter of the cell (ϕ 0.8”) to allow the cell to sit in. A layer of glass powder mixed with a binder is then applied to the edge between cell and the holder. The holder is made of an Ultra-High-Temperature Alloy X Nickel (from McMaster), on which an outlet and inlet tubing in OD 0.125” are weld in the upper and bottom positions, respectively. Figure 3.2 shows the actual picture of the holder. The new designed holder shows better gas tightness since the additional grove on the surface of battery vessel can keep the melted glass powders distributed around the gap between RSOFC and battery vessel at high temperature, while the melted glass powders easily flow away from the surface of vessel, see Figure 3.2b. With the new design, the successful rate of battery testing has been increased by 10-fold, from 10% to 100%.

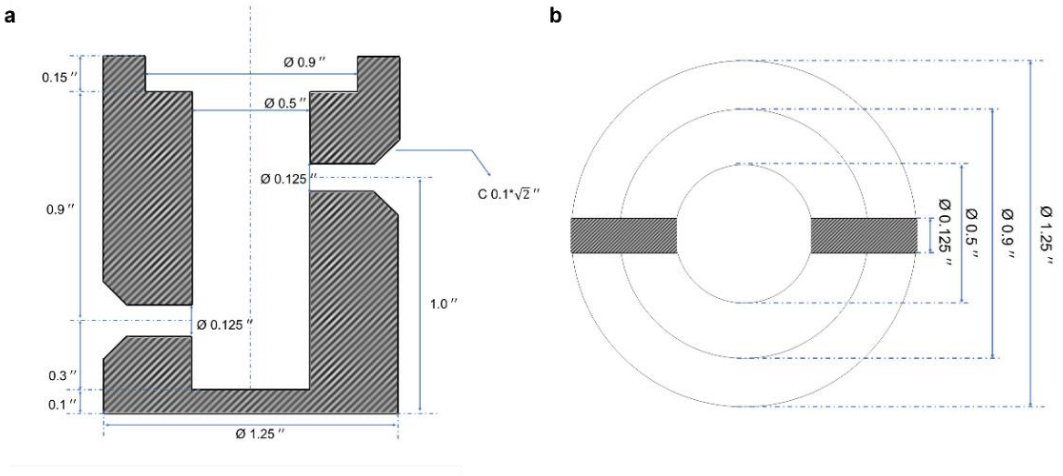

Figure 3.1 A new design of the battery holder: (a) cross section; (b) top view.

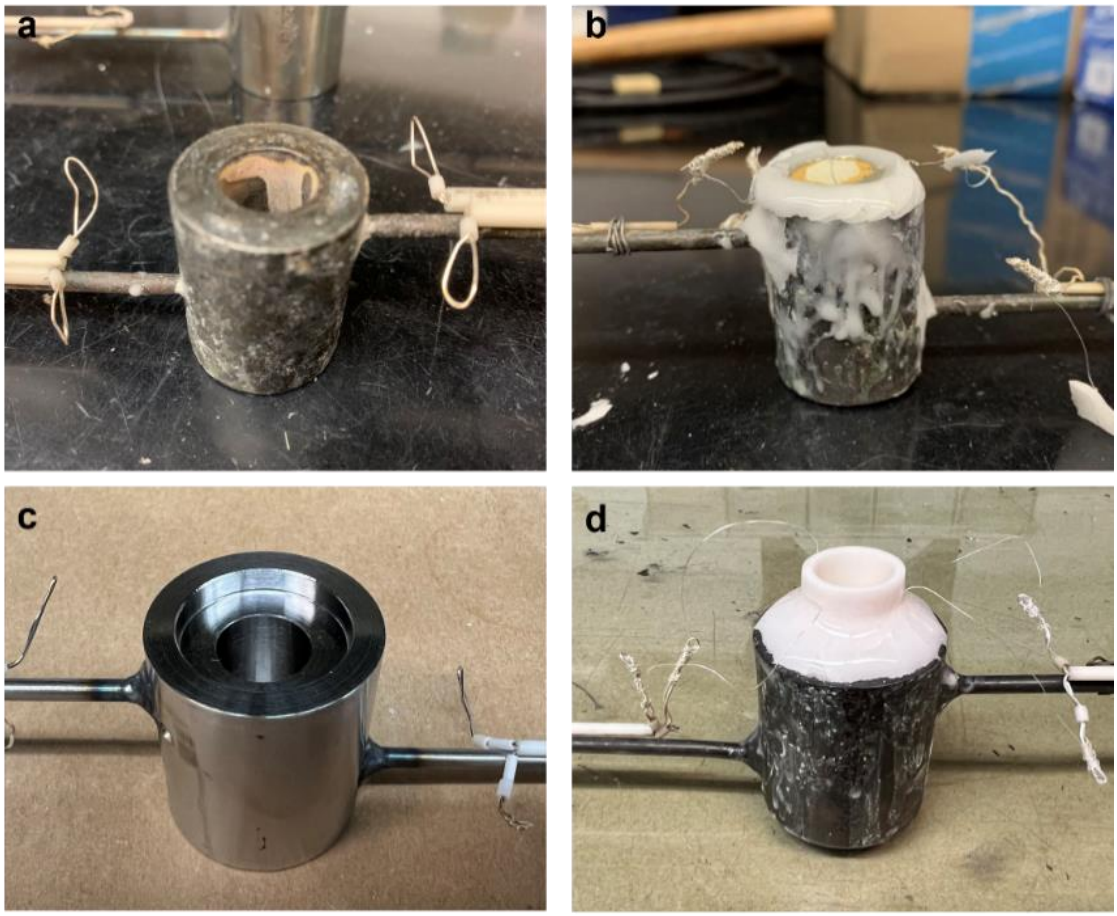

Figure 3.2 Actual picture of battery holder: (a and b) old design; (c and d) new design.

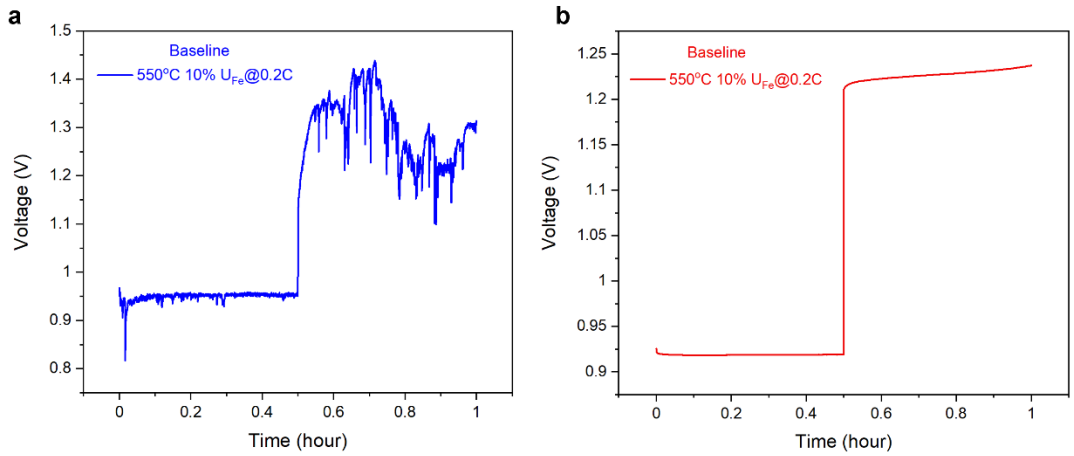

Figure 3.3 Voltage profiles of iron-air battery with energy storage materials of Fe_2O_3/ZrO_2 during one whole cycle with U_{Fe}=10% and current density of 0.2 C at 550 ºC (10 mA cm^{-2}): (a) old design; (b) new design.

In order to confirm the improved gas tightness of new designed battery holder, the voltage changes during charge and discharge process were exterminated, as shown in Figure 3.3. Compared to the old design, the newly designed battery shows more reliable electrochemical data since the better gas tightness which provides a stable and close gas environment.

3.4 Modification of HE-Supported Electrolyte

The RSOFC consists of an oxide-ion conducting solid electrolyte between two electrodes, where the charge carriers are oxygen ions. In SOFC mode, the oxygen fed to the air electrode is reduced into oxygen ions which diffuse through the electrolyte to the fuel electrode side, oxidizing hydrogen into water. The opposite mechanism occurs in SOEC mode, where the water in fuel electrode receives electrons from the external circuit, producing hydrogen and oxygen ions; the latter is pumped back to the oxygen electrode through the electrolyte, where it is oxidized into oxygen. Therefore, the performance of RSOFC is closely related to the electrochemical activity and stability of the electrode materials and electrolyte. For example, decreasing the thickness of electrolyte reduces the resistance of oxygen ions transport, resulting in improved performance. To achieve thin and dense electrolyte structure, the modified dip-coating method was used to fabricate anode-supported electrolyte.

3.4.1 Co-Pressing Method

As a method to make pellets, the co-pressing process was also widely used to fabricate anode-supported electrolyte due to its easiness. In this study, the co-pressing method was evaluated. In detail, the anode support with a thickness of 800 μm was first fabricated by die pressing; then ~0.07g pure ScSZ powders was added onto the surface of the substrate

and co-pressed to form an electrolyte layer. Figure 3.4 shows the cross-sectional images of a co-pressed cell. The electrolyte-anode interface sintered by conversional sintering method at 1350 ºC for 5h is shown in Figure 3.4a. It can be seen that the anode is well adhered to the electrolyte membrane (~45 μm). Figure 3.4b and 3.4c exhibit the anode support structure before and after reduction, respectively, where few pores distributed non-uniformly in the anode support are seen.

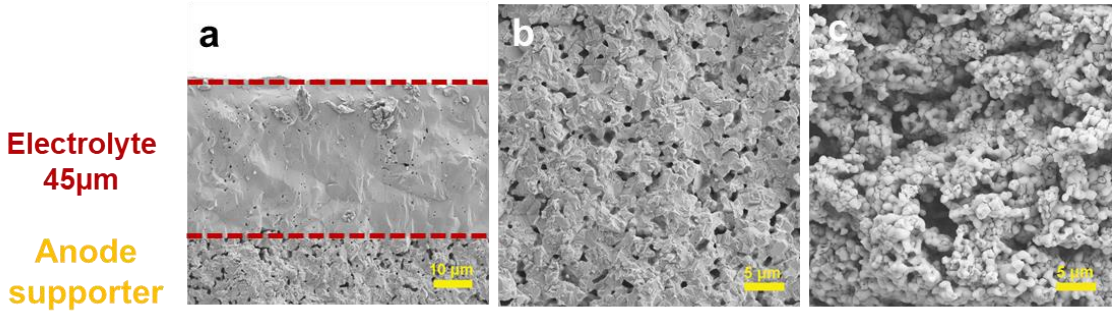

Figure 3.4 SEM image of HE-supported electrolyte made by co-pressing: (a) cross-section of electrolyte/anode interface before reduction; (b) HE-support before reduction; (c) HE-support after reduction.

Figure 3.5a shows the V-I curves and power density of the ScSZ cell fabricated by co-pressing method. Maximum power density of 89 mW cm^{-2} with open-circuit voltage (OCV) of 1.142 V was obtained at 550 ºC. Figure 3.5b exhibits the electrochemical impedance spectra of the cell measured under open-circuit conditions at 550 ºC. For full cell, the high frequency intercept corresponds to the ohmic resistance of the cell (R_o), contributed from the ionic resistance of the electrolyte and electronic resistance of the electrodes. The low frequency intercept represents the total resistance (R_t) of the cell. R_t includes the R_o and the interfacial polarization resistance (R_p), which corresponds to cathode-electrolyte and anode-electrolyte interfacial resistances. The expected ohmic resistance from the co-pressed cell is 5.7 Ω cm^{-2} at 550 ºC with a fresh electrode. The

cycling performance testing results shown in Figure 3.5c suggest that after few cycles the overpotential increased sharply since the limited porous structure hinders the charge process (SOEC mode). Therefore, a more porous and thinner electrolyte should be fabricated to achieve a better electrochemical performance of battery.

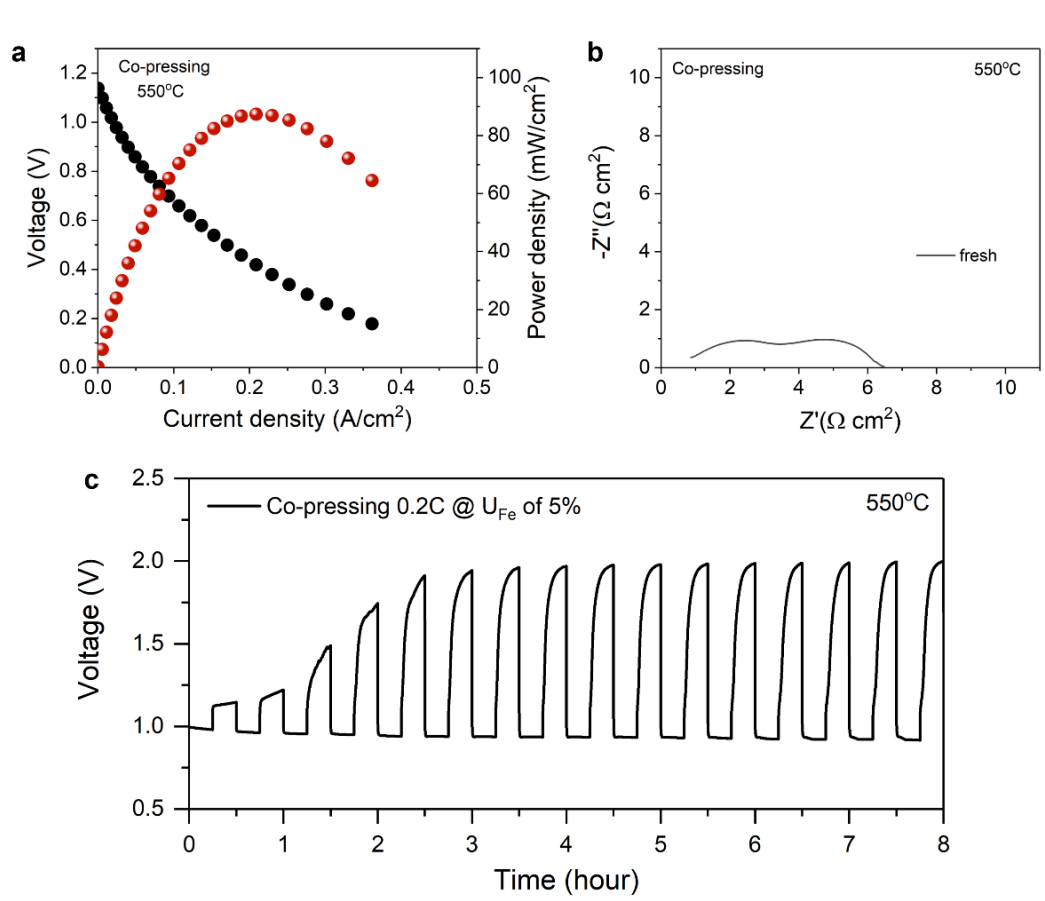

Figure 3.5 Electrochemical performance of co-pressing single cell: (a) cell voltage and power density as a function of current density at 550 °C for the fresh electrodes; (b) Impedance spectra and resistances of the single cell under open-circuit conditions; (c) cycling performance of battery tested at a current density of 0.2 C (10 mA cm^{-2}) with an iron utilization of 5%.

3.4.2 Dip-Coating Method

Dip-coating process is one of the commonly used liquid-phase deposition method for the formation of thin films. This method is based on dipping a substrate into a slurry and

after the solvent component on the substrate is dried out, a solid thin film is left on the substrate. Compared to the co-pressing method, this method can obtain a thinner electrolyte layer on a controlled porous anode support. The formulae containing ScSZ powders, 2-propanol as solvent, PVP and PVB as polymer binder, terpineol as dispersant, were prepared as the electrolyte slurry, see Table 3.1. For the anode functional layer, NiO and carbon black were added into the slurry; carbon black acts as a pore former.

Table 3.1 Formulae of dip-coating slurry for function layer and electrolyte layer

Component	Function Layer		Electrolyte Layer	
	Percent (wt.%)	Mass (g)	Percent (wt.%)	Mass (g)
NiO	13.0%	7.20	---	---
ScSZ	8.7%	4.80	12.0%	6.00
Carbon black	2.2%	1.20	---	---
45% PVP	4.0%	2.20	2.2	1.08
PVB	0.6%	0.36	0.4%	0.22
Terpineol	6.2	3.40	6.8%	3.40
2-propanol	65.3	36.00	78.6%	39.40

The cross-sectional view of microstructure in the dip-coated anode-supported half-cell is shown in Figure 3.6a. A 10-μm thick, dense ScSZ electrolyte and 10-μm thick, porous functional layer are clearly seen on the anode-support. Figure 3.6b and 3.6c shows pores in a diameter of 3-5 μm in the porous anode before and after reduction in H_2-3% H_2O at 550 ^oC, respectively. Compared to the co-pressed half-cell, the cell fabricated by dip-coating technology shows bigger pores and thinner electrolyte, which could improve the cell performance.

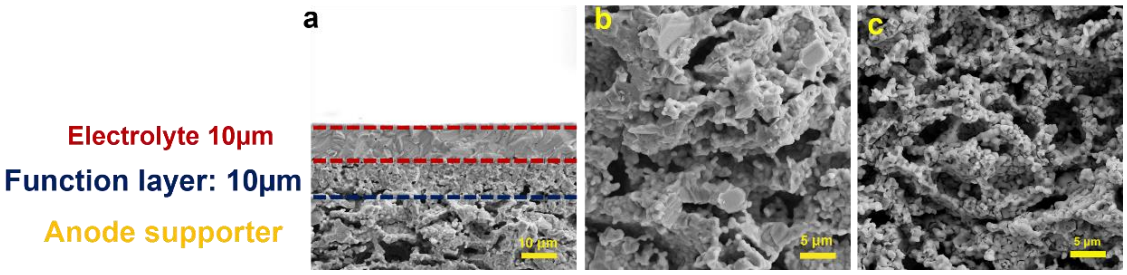

Figure 3.6 SEM image of anode-supported electrolyte made by dip-coating technology: (a) cross-section of electrolyte/anode interface before reduction; (b) anode-support before reduction; (c) anode-support after reduction.

Figure 3.7a compares variations of OCV *vs.* time in H_2-3%H_2O for co-pressed and dip-coated cells in open system. Evidently, the dip-coated cell exhibits a shorter reduction time than co-pressed counterpart because of its larger initial pores in HE. After full reduction, the dip-coated cell also exhibits a slightly higher OCV than co-pressed cell (1.144 *vs.* 1.138V), suggesting that the former has a much better gas tightness. The current-voltage and current-power curves of the cell are shown in Figure 3.7b. The cell open circuit voltage at 550 ºC is 1.144V is very close to the theoretical values, indicating that the dip-coated electrolyte is dense enough and the battery shows excellent gas tightness. The corresponding maximum power density is 152 mW cm^{-2}, which exhibits near 60% improvement than that of co-pressing cell, since the thinner electrolyte and porous anode support. However, the maximum power density decays 30% after cycling performance testing at a current density of 10 mA cm^{-2}, which could be attributed to the degradation of cathode materials and anode active materials, Ni, aggregation at the SOFC and SOEC environment alternately. In order to figure out the degradation source, the cathode stability should be estimated.

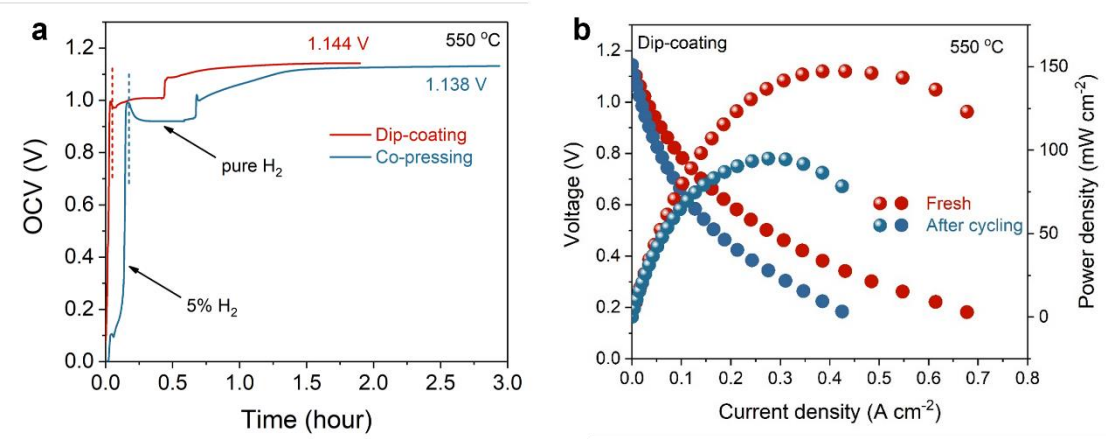

Figure 3.7 (a) A profile of OCV *vs.* time during reduction process in open system for RSOFC made by co-pressing and dip-coating technology; (b) Cell voltage and power density as a function of current density at 550 ºC for the fresh cell and cycling tested cell by dip-coating technology at a current density of 0.2 C (10 mA cm^{-2}) with an iron utilization of 5%.

3.5 Electrochemical Analysis of Oxygen Electrode (OE)

To evaluate the overpotentials contributed from different cell components and figure out the degradation source so that we can purposely work toward improving the performance-limiting component, we use the symmetrical three-electrode cell (STEC) method we developed recently [71]. Figure 3.8a and 3.8b show a schematic of STEC method. The counter electrode (CE) and working electrode (WE) are identical OE of LSM/BYC, while the reference electrode is a gold wire attached to the circumference of the electrolyte disk. Depending on the direction of the DC current applied, EIS spectrum related to either ORR (discharge) or OER (charge) polarization can be obtained. For example, when a positive current density (j) is applied as shown in Figure 3.8b, EIS spectrum related to the OER process can be obtained. Figure 3.9a shows the obtained polarization resistance (R_p) of both ORR and OER *vs.* j at 550 -700 ºC. It is evident that R_p decreases with j, which is expected from the *Butler-Vomer* equation. The degree of R_p reduction is more pronounced at lower temperatures, further implying the low-

temperature dominance of the charge transfer process. At higher temperatures where charge-transfer process is more facile, j has less effect on R_p. It is interesting to mention that OER-R_p of the LSM-BYC becomes noticeably lower than that of ORR at high j, making the polarization curve asymmetrical. This finding is important evidence that LSM-BYC is a better OER electrode at high j.

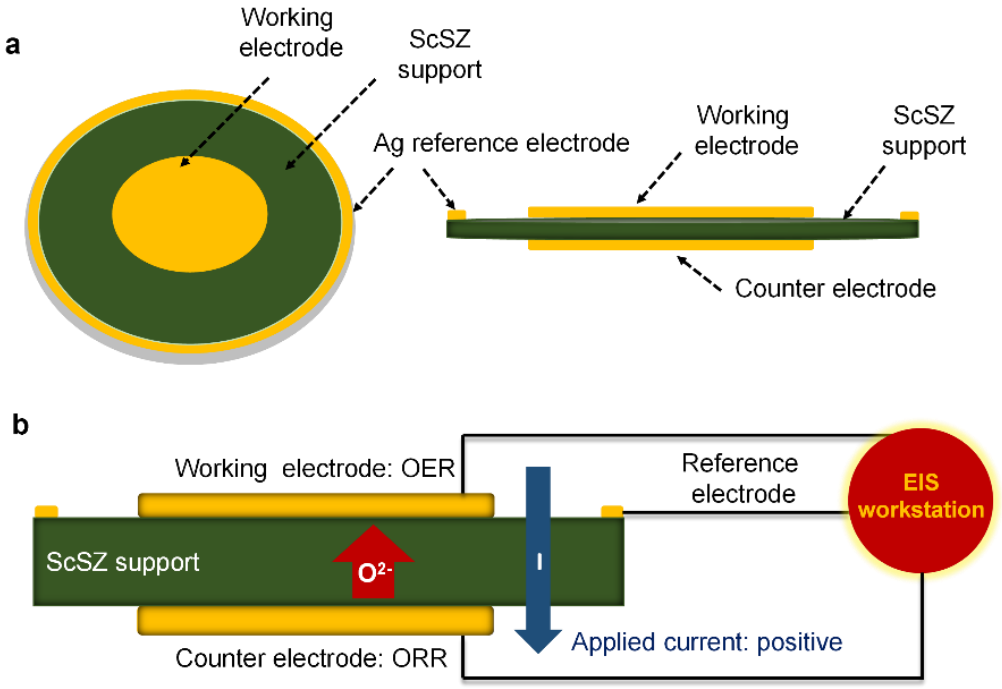

Figure 3.8 (a) and (b) Schematic of STEC method

The obtained $R_p(j)$-j data in Figure 3.9a can be further integrated into overpotential $\eta(j)$ by

$$\eta(j) = \int_0^j R_p dj \tag{3.1}$$

The overpotential (η) derived from R_p is shown in Figure 3.9b *vs.* j. A typical Tafel curve in both OER and ORR domains are clearly observed. We further apply below

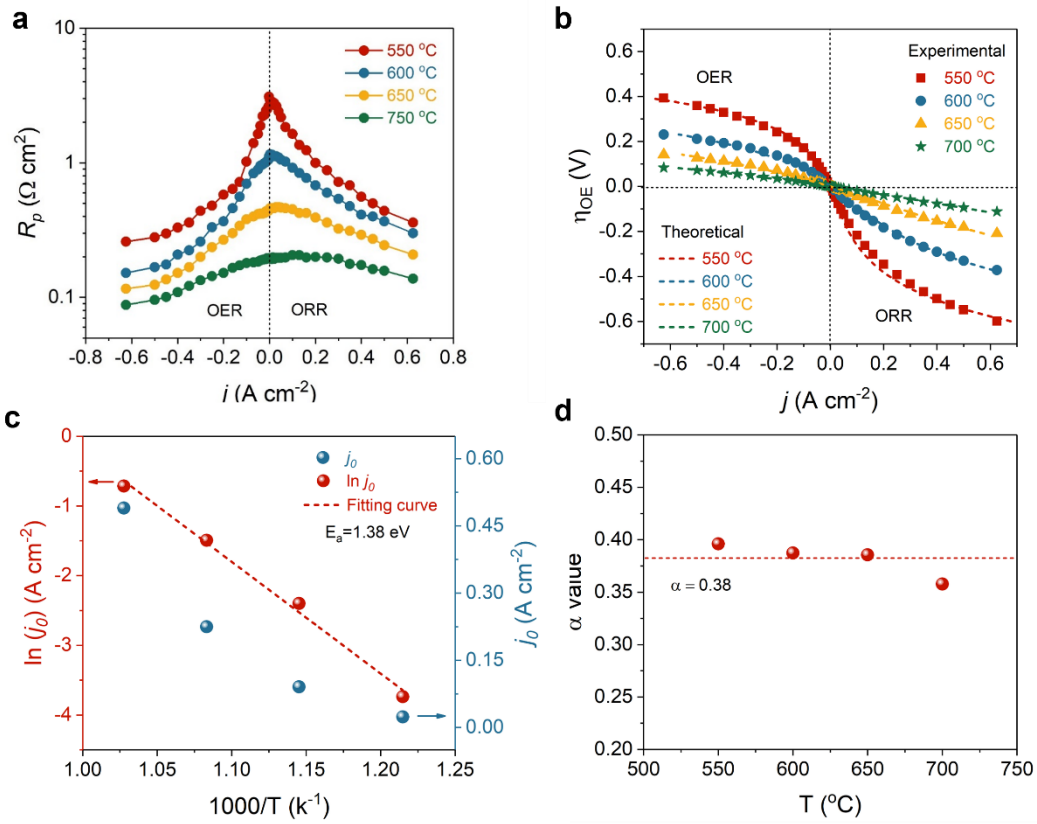

Figure 3.9 (a) R_p of LSM/BYC OE *vs. j* at different temperatures; (b) η_{OE} *vs. j*; (c) ln (j_0) *vs.* 1/T and (d) α *vs.* T.

Butler-Volmer equation [72] (assuming that ORR and OER are multi-step charge transfer processes, but the rate-limiting step involves single electron transfer) to fit the data with exchange current density j_0 and transfer coefficient α as variables:

$$j = j_o\left(exp\left(\frac{-\alpha F\eta}{RT}\right) - exp\left(\frac{(1-\alpha)F\eta}{RT}\right)\right) \tag{3.2}$$

where F, R and T have their usual meanings. The fitting results are shown in Figure 3.9c and 3.9d as a function of temperature. It is clear that j_o follows Arrhenius relationship with an activation energy E_a=1.38 eV, while α is insensitive to T and the average α is ~ 0.38 over 550-700°C.

With η_{OE} in Figure 3.9b and combining the overall V-j curve from the full cell, the

overpotential resulting from HE can be separated by the following equations

$$\eta_t = \pm(E_N - V_C) \tag{3.3}$$

$$\eta_{HE} = \eta_t - (\eta_{ohm} + \eta_{OE}) \tag{3.4}$$

where η_t is the total overpotential; "+" for ORR and "-" for OER; $\eta_{ohm} = jR_o$, where R_o is ohmic resistance obtained from EIS; V_C and E_N are cell voltage in the full cell and Nernst potential, respectively.

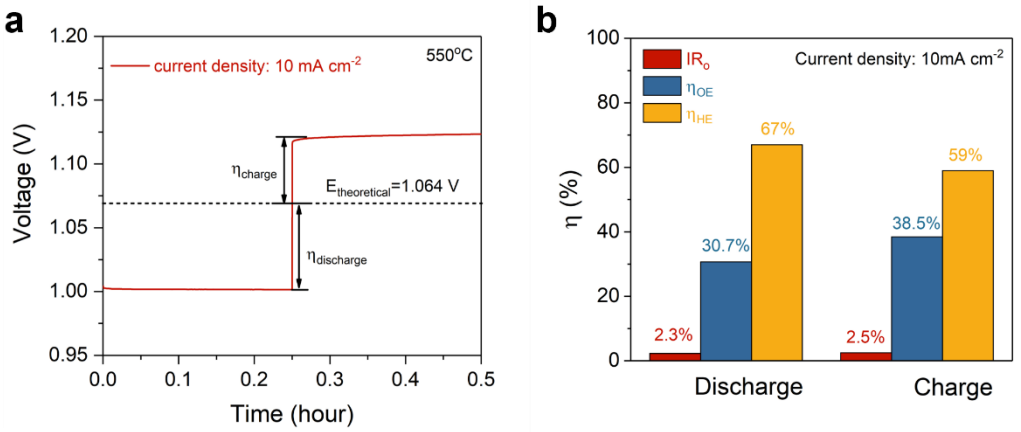

Figure 3.10 (a) A typical discharge and charge profile of SOIAB at j= 10mA cm^{-2} with U_{Fe}=5% of a cell by dip-coating technology; (b) η distribution among different cell components of the cell.

Figure 3.10a shows a typical discharge and charge profile of the battery at j=10 mA cm^{-2} (0.2 C) and U_{Fe}=5%. Based on the profile and eq. (3.3), η_t of discharge and charge processes is obtained separately. After separating overpotential contribution from cell components, Figure 3.10b compares them among cell components for the dip-coating cell. The results suggest the overpotential from HE, η_{HE}, accounts for 67 and 59% for discharge and charge, respectively, which is higher much more than that of OE. In addition, a slightly higher η_t for discharge than charge, which is consistent with the higher R_p for ORR (discharge) than OER (charge) shown in Figure 3.9a.

The long-term R_p stability of the LSM-BYC OE is also evaluated at j = 10 mA cm^{-2}

and 550 ºC; the results are shown in Figure 3.11. The LSM-BYC electrode shows a good stability for both OER and ORR polarization over ~500 h (it is in fact decreasing with time during the polarization), implying that any performance degradation of RSOFC may be related to either HE or electrolyte.

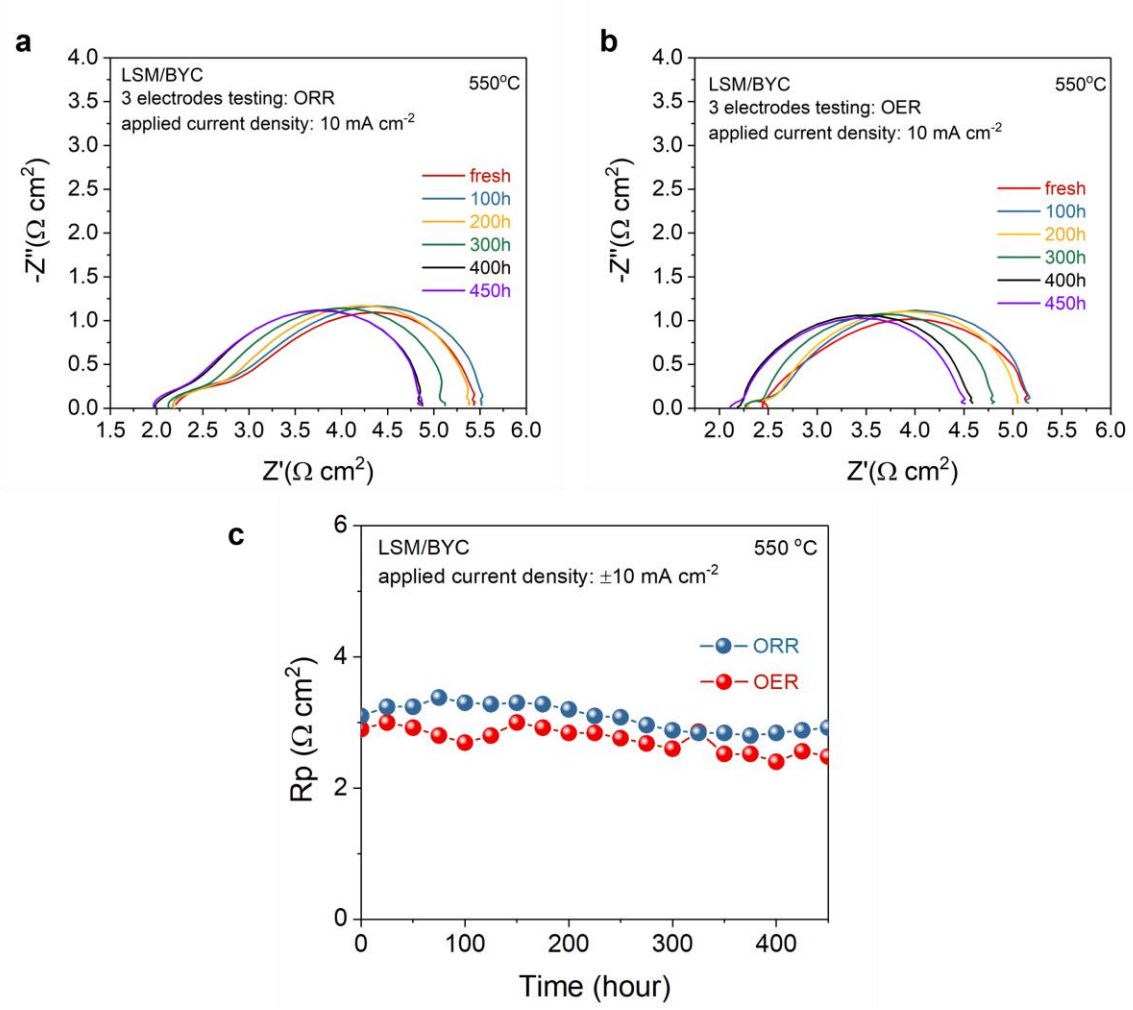

Figure 3.11 Stability of LSM/BYC cathode evaluated by three-electrode symmetric cell under an applied j= 10 mA cm^{-2}: (a) EIS spectra *vs.* time during ORR process; (b) EIS spectra *vs.* time during OER process; (c) R_p of ORR and OER *vs.* time.

3.6 Effect of GDC Infiltration on HE Degradation

The RSOFC performance has been significantly improved using dip-coating technology. However, questions remain regarding RSOFC long-term stability, especially at close

system that are generally high steam conditions (> 23 vol.%). The stability of Ni-ScSZ HE is a key issue. One common degradation phenomenon is Ni agglomeration at high steam environment, which leads to a decrease in triple phase boundary (TPB) length [73]. Furthermore, ZrO_2 reduction to form Ni-Zr compounds at very low oxygen levels could result in structural degradation in the TPB area [74]. In order to reduce Ni-ScSZ HE degradation, a few strategies, including fabrication of smaller Ni-ScSZ microstructure and mixed conductivity introducing have been proposed [74-77]. Both these measures tend to increase the TPB density and enhancing electrochemical activity. Here, we demonstrated that the electrode polarization resistance and stability of RSOFC was improved significantly by infiltrating gadolinia-doped ceria (GDC).

3.6.1 Microstructural Analysis

For the best performing RSOFC with 2 wt.% GDC infiltrated in the HE-support (to be shown later), we performed a detailed microscopic analysis. Figure 3.12a and 3.12b show its microstructures after reduction, where a porous structure like the original one (Figure 3.6c) after GDC infiltration is still observed; the infiltrated GDC appears to exhibit as a thin layer on the Ni-ScSZ surface. The elemental mapping results shown in Figure 3.12c indicate a uniform distribution of Zr, Sc, O, Ni, Ce and Gd across the HE; their semiquantitative contents analyzed by EDS are given in Figure 3.13.

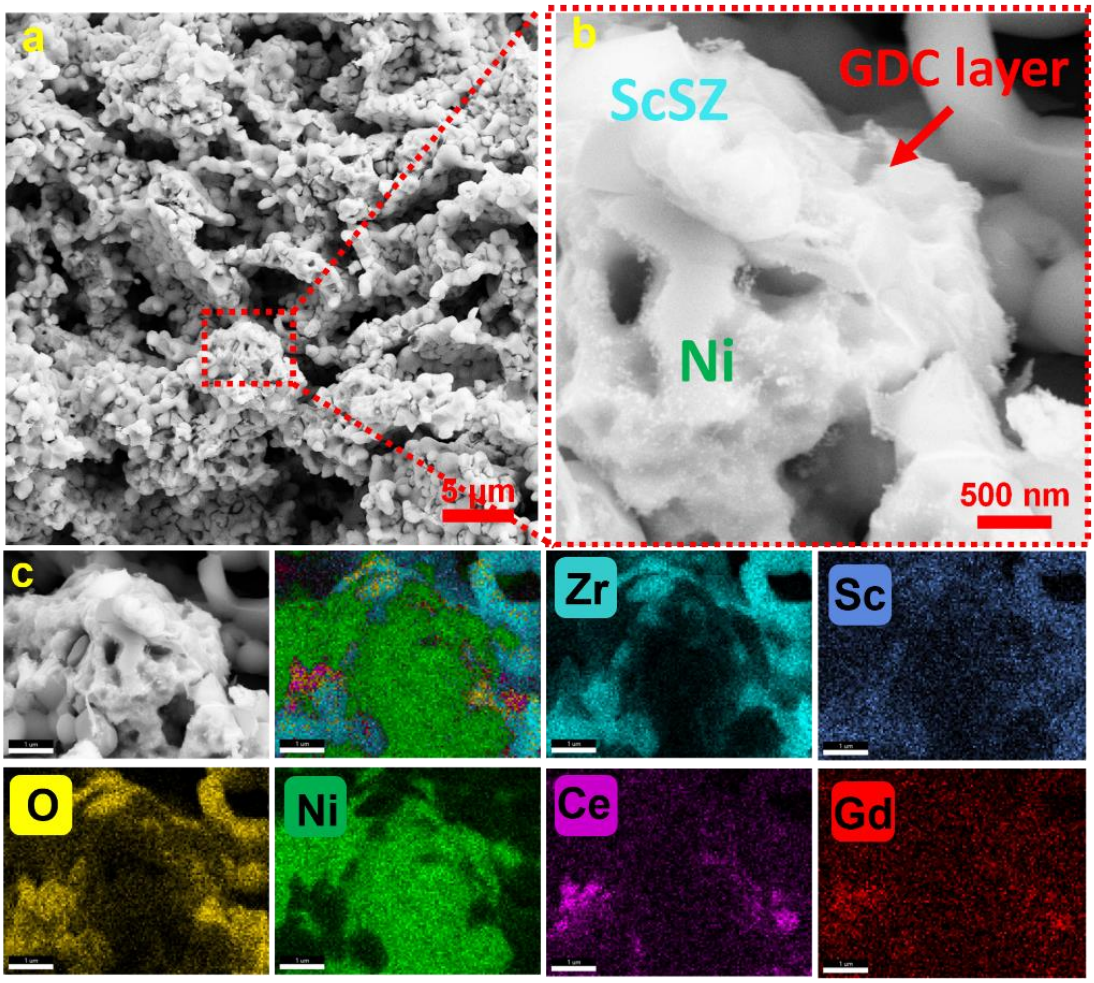

Figure 3.12 (a) and (b) SEM images of 2 wt.% GDC infiltrated HE-supported cell made by dip-coating; (c) elemental mapping. The sample was reduced in H_2.

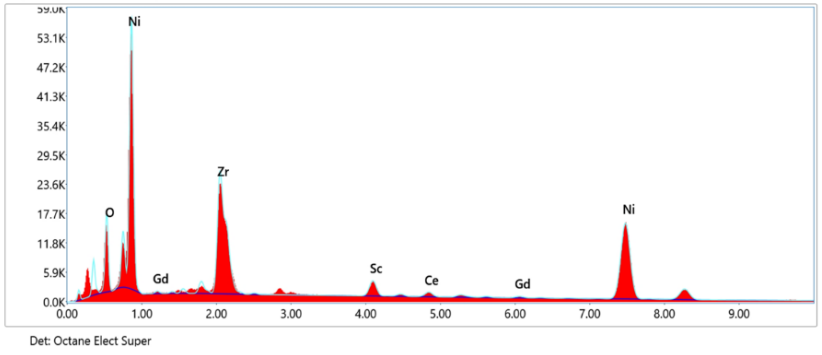

Element	Weight %	Atomic %
O K	8.65	27.93
ScK	3.01	3.46
NiK	62.35	54.87
ZrL	21.38	12.10
CeL	3.20	1.18
GdL	1.41	0.46

Figure 3.13 EDS spectrum and the corresponding elemental distributions of 2 wt.% GDC infiltration HE.

We further performed STEM to obtain a better elemental distribution and thickness of GDC layers. While there is no GDC present in the baseline HE (Figure 3.14a and 3.14b), Figure 3.14c and 3.14d clearly show a thin layer (~20 nm) of GDC layer on the surface of ScSZ/NiO particles for the 2 wt.% GDC sample; the GDC layer is thicker for the 4 wt.% GDC sample, see Figure 3.14d and 3.14e. Figure 3.15 shows the TEM images 4 wt.% GDC sample. It is observed that there is thicker GDC layer (~200 nm) on the

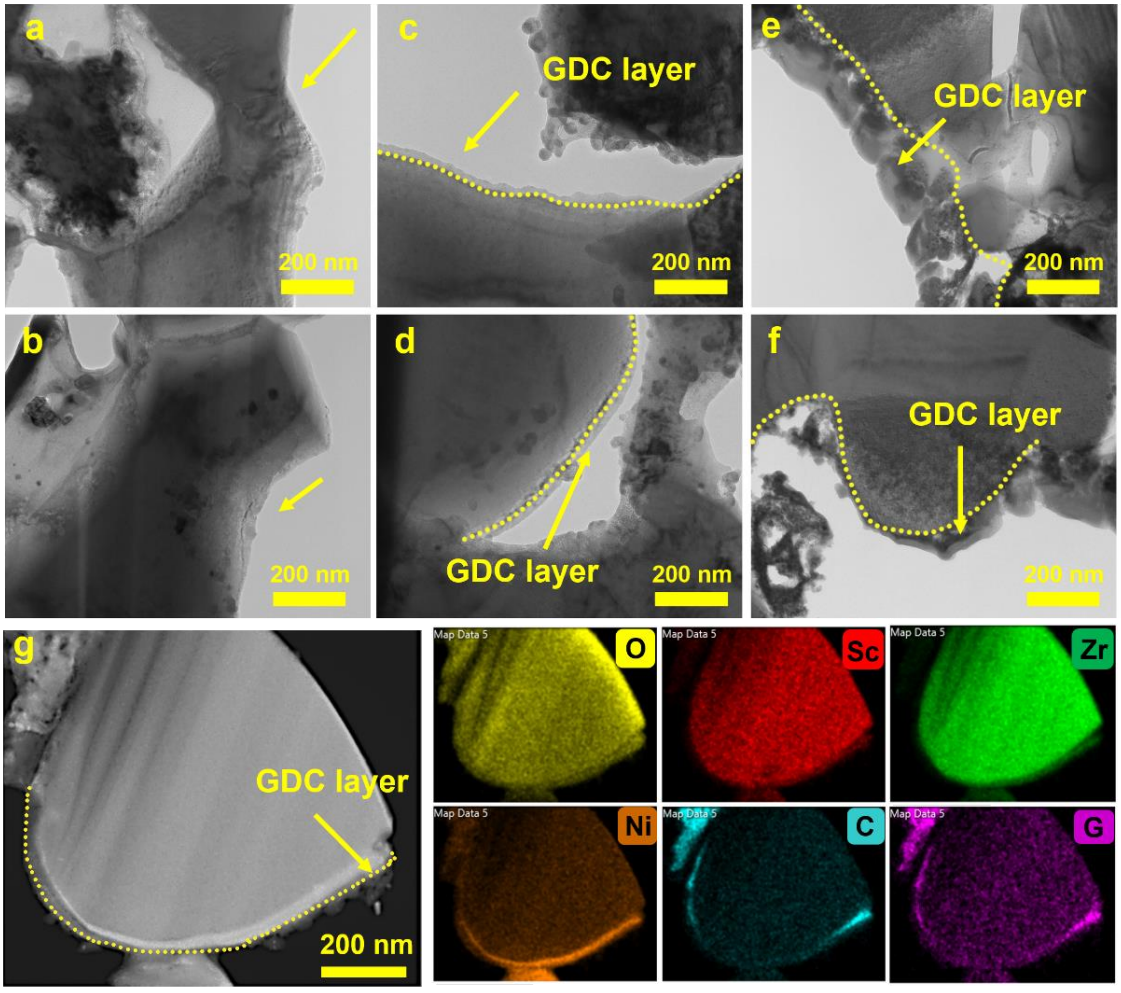

Figure 3.14 TEM image of (a and b) the baseline HE-supported cell made by dip-coating; (c and d) HE-support with 2 wt.% GDC; (e and f) HE-support with 4 wt.% GDC; (g) STEM mapping of a HE particle with 2 wt.% GDC after testing. All samples shown were after reduction in H_2.

surface of HE. Figure 3.16 shows the EDS elemental analysis. Compared to the 2 wt.% GDC sample, the 4 wt.% GDC sample contains much more Ce and Gd elements. The cell with 2 wt% GDC in HE was further analyzed after testing for 830 hours. Figure 3.14g shows more clearly a 20 nm thick GDC layer on the surface of an ScSZ particle and the same chemistry as that before testing.

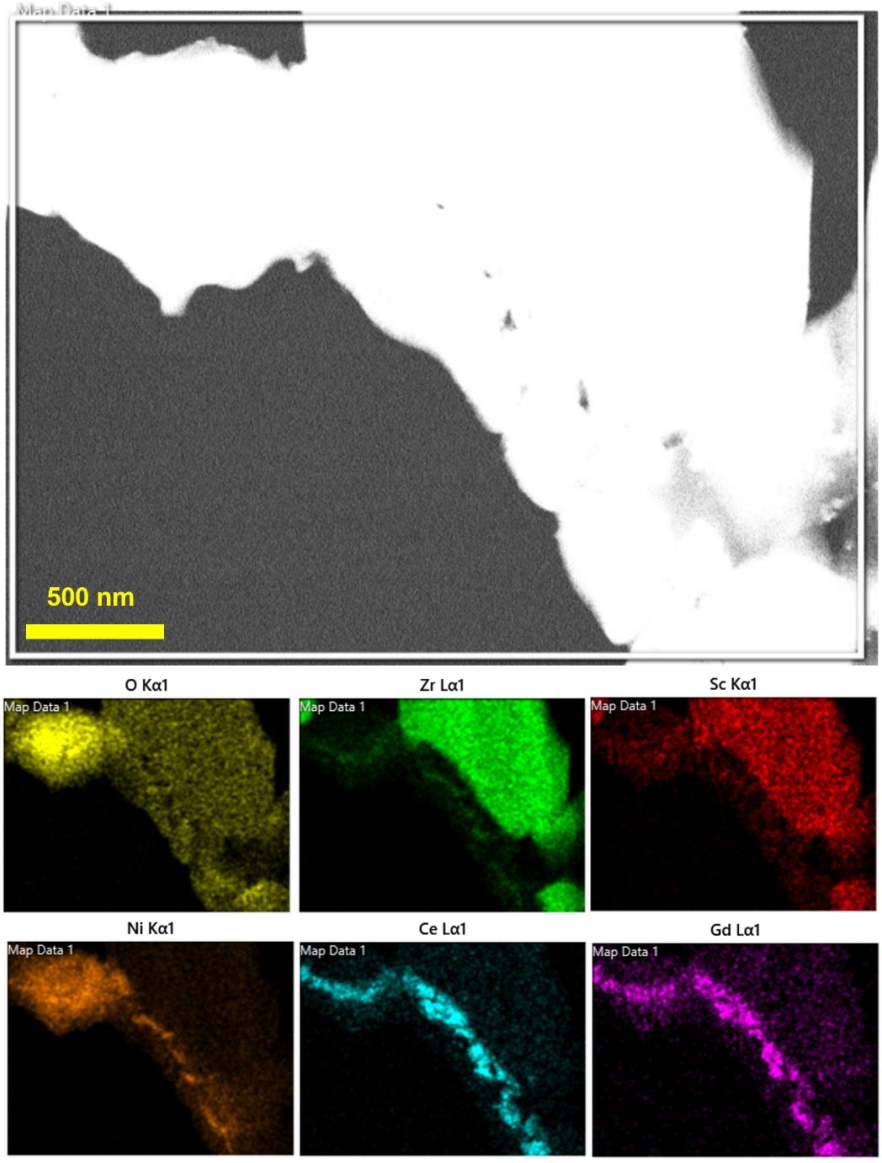

Figure 3.15 TEM image and the corresponding elemental mapping of 4 wt.% GDC infiltrated HE after reduction.

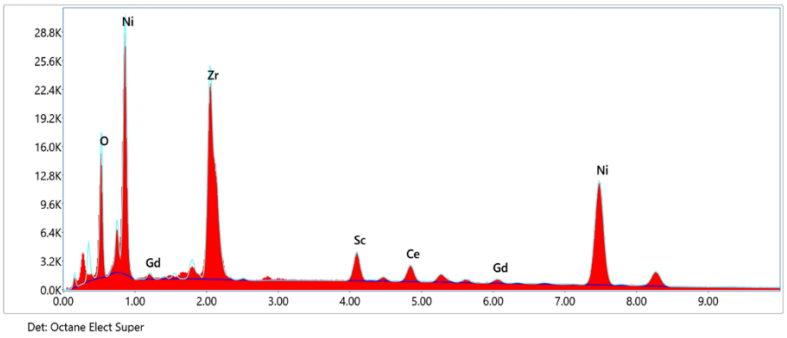

Element	Weight %	Atomic %
O K	10.58	33.63
ScK	3.60	4.08
NiK	53.04	45.97
ZrL	23.25	12.96
CeL	7.25	2.63
GdL	2.28	0.74

Figure 3.16 EDS spectrum and corresponding elemental contents of 4 wt.% GDC infiltrated HE.

3.6.2 Electrochemical Performance of RSOFC

After separating overpotential contribution from cell components, Figure 3.17a compare them among cell components for the baseline cell and GDC-modified cell. Compared to the HE without GDC, the overpotential from GDC infiltrated HE decreases obviously, where the η_{HE} accounts for 43.8 and 17% for discharge and charge, respectively. Figure 3.17b plots the effect of GDC loading on η_{HE}, suggesting that 2 wt.% is the optimal GDC loading.

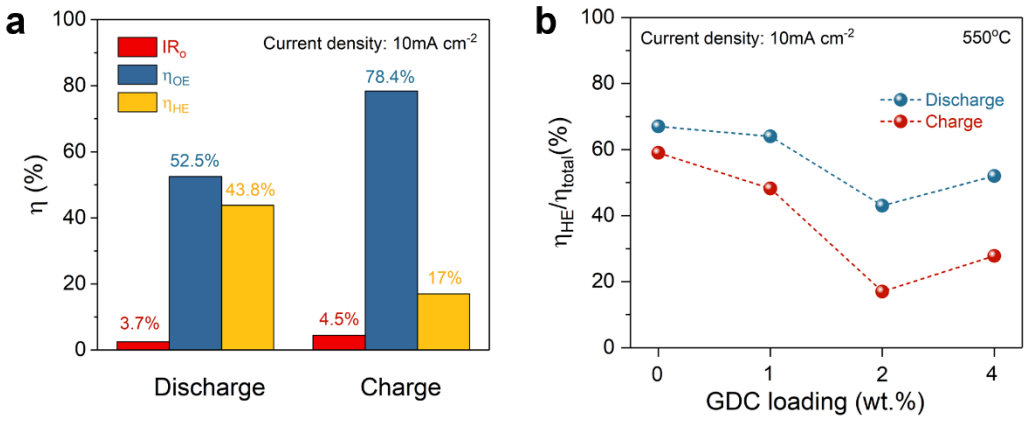

Figure 3.17 Separating overpotential contribution from cell components: (a) η distribution among different cell components of the 2 wt.% GDC-modified cell; (b) η contribution from HE for different GDC loadings.

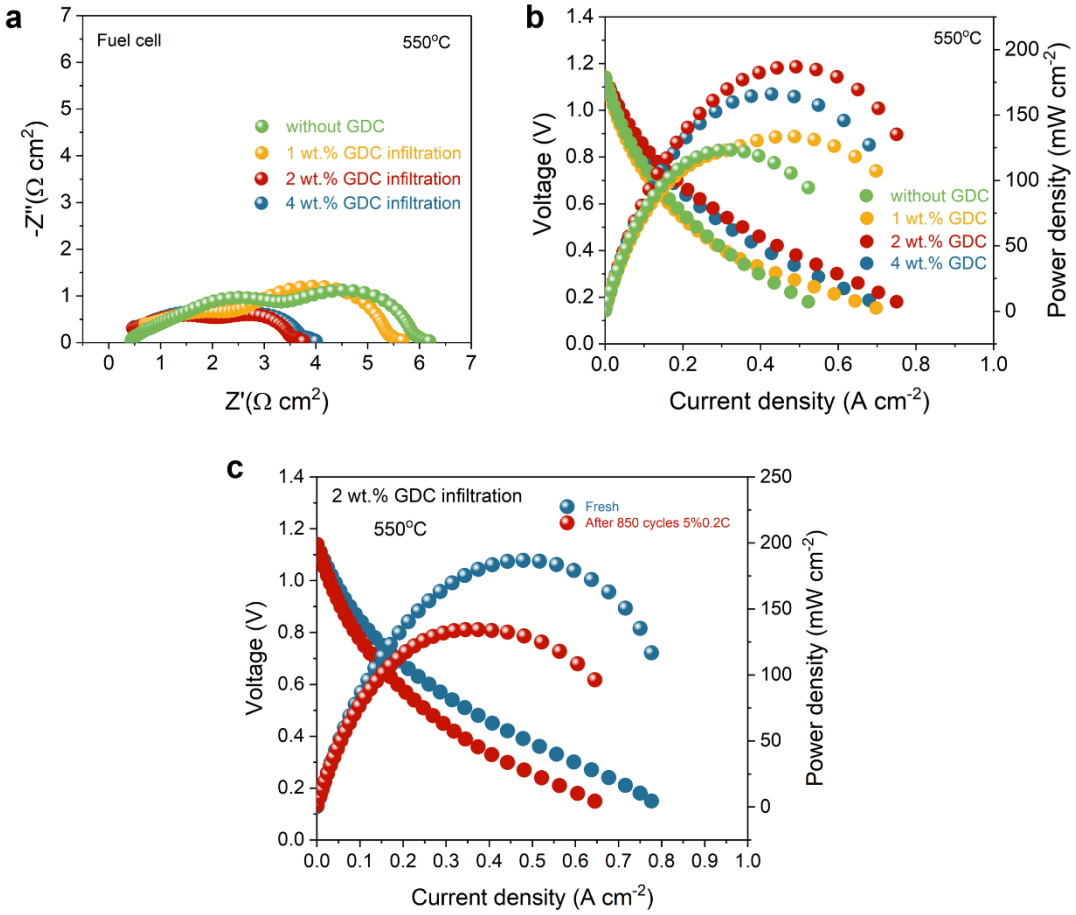

Figure 3.18 Comparison of cell performance at different GDC loadings: (a) EIS; (b) V-I and P-I curves; (c) V-I and P-I curves of the cell made by dip-coating method with 2 wt.% GDC added HE.

Subsequently, electrochemical impedance spectroscopy (EIS) measurements for the Ni-ScSZ and Ni-ScSZ:GDC electrode full cells were conducted with 3% H_2O at OCV in order to characterize the initial state of the cells. Figure 3.18 summarizes the ohmic resistance (R_Ω) and electrode polarization resistance (R_p) values. The R_Ω maintains a constant for different electrodes, while the R_p decreases gradually with the GDC loading increases, which could be attributed to that the formed GDC film electrode/electrolyte interface improves transfer process. The performance was also evaluated in a single cell. The V-I curves (Figure 3.18b) indicates the maximum power density reaches to 200 mA

cm^{-2} at 550 °C for 2 wt.% GDC infiltrated cell, which has a significant improvement compared to that of pristine HE cell. However, when the GDC loading increases to 4 wt.%, the performance did not show further improvement. That could be attributed to the thick GDC layer on the surface of electrode (see Figure 3.15) and slow transfer process, suggesting that 2 wt.% is the optimal GDC loading. After GDC infiltration treatment, the stability of RSOFC is also significantly improved, as shown in Figure 3.19c.

3.6.3 Electrochemical Performance of Battery

An exemplary performance demonstration of SOIAB operated at 550 °C is collectively shown in Figure 3.19. The performance of the cell tested as a battery was conducted in a closed system, *i.e.* the H_2 inlet and outlet were closed. Figure 3.19a gives the original voltage profiles at different C rate and Figure 3.19b shows the effect of C-rate varying from 0.1 C (5 mA cm^{-2}) to 0.6 C (30 mA cm^{-2}) on round-trip efficiency (RTE) at a fixed U_{Fe}= 10%. The battery can achieve an RTE= 95% at 0.1 C, but only 58% at 0.6 C. Since the voltage of RSOFC itself at higher *j* (*e. g.* 0.6 C=30 mA cm^{-2}) is still high (~1.0 V), see Figure 3.18c of V-*j* curve, the low RTE at higher C-rate is likely resulted from the slow reduction kinetics in the Fe-bed; When the C-rate returns to 0.1 C, a high RTE=93.2% is still achievable. U_{Fe} of the SOIAB is of critical importance to RTE and energy capacity to be stored. Figure 3.19c shows voltage profiles at different U_{Fe} under a fixed *j*=10 mA cm^{-2} (0.2 C). As U_{Fe} is increased from 5 to 100%, the total discharge time is increased proportionally from 15 to 300 min; see Supporting Information for the energy density calculation. In this study, only one cycle at each U_{Fe} was performed to show the effect of U_{Fe} on energy capacity; the low and high cutoff voltages were set to 0.6 and 2.0 V for discharge and charge cycle, respectively. From the results in Figure 3.19c, it is evident

that the battery can be cycled with a stable plateau at $U_{Fe} \leq 80\%$. At $U_{Fe} > 80\%$, however, the discharge voltage experiences a sharp decrease and reaches the cutoff voltage quickly, implying a severe mass transport limitation, likely related to the depletion of Fe. It is interesting to note that the charging process can still reach a stable voltage at $U_{Fe}=100\%$, reflecting the battery's ability to be recharged (reduction of iron oxide) even after the depletion of Fe during the discharge cycle.

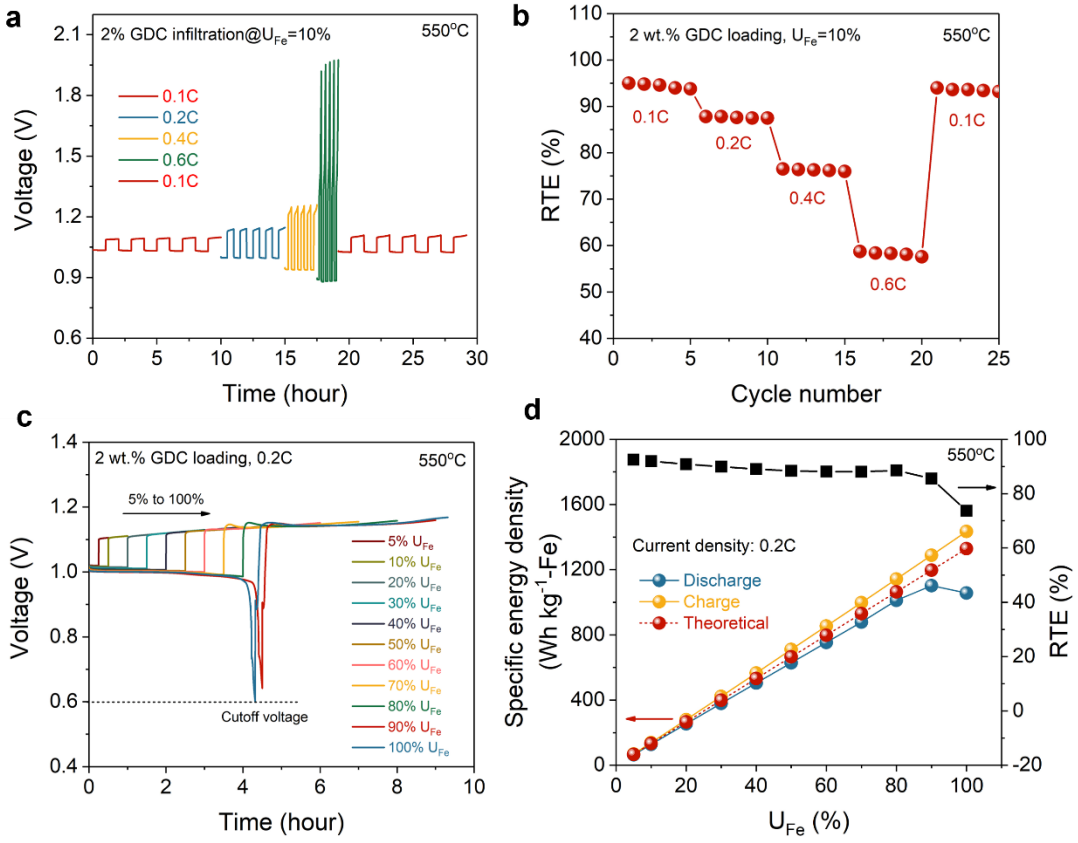

Figure 3.19 (a) A profile of OCV *vs.* time during cycle at different C rate for SOIAB with 2 wt.% GDC infiltrated RSOFC made by dip-coating; (b) effect of C-rate on RTE; (c) voltage profiles *vs.* time at a fixed j= 10 mA cm^{-2} (0.2 C) and different U_{Fe} (5-100%); (d) discharge and charge SED and corresponding RTE *vs.* U_{Fe}.

The discharge and charge specific energy density (SED) and RTE are further calculated and plotted in Figure 3.19d as a function of U_{Fe}. With an increase of U_{Fe}, both

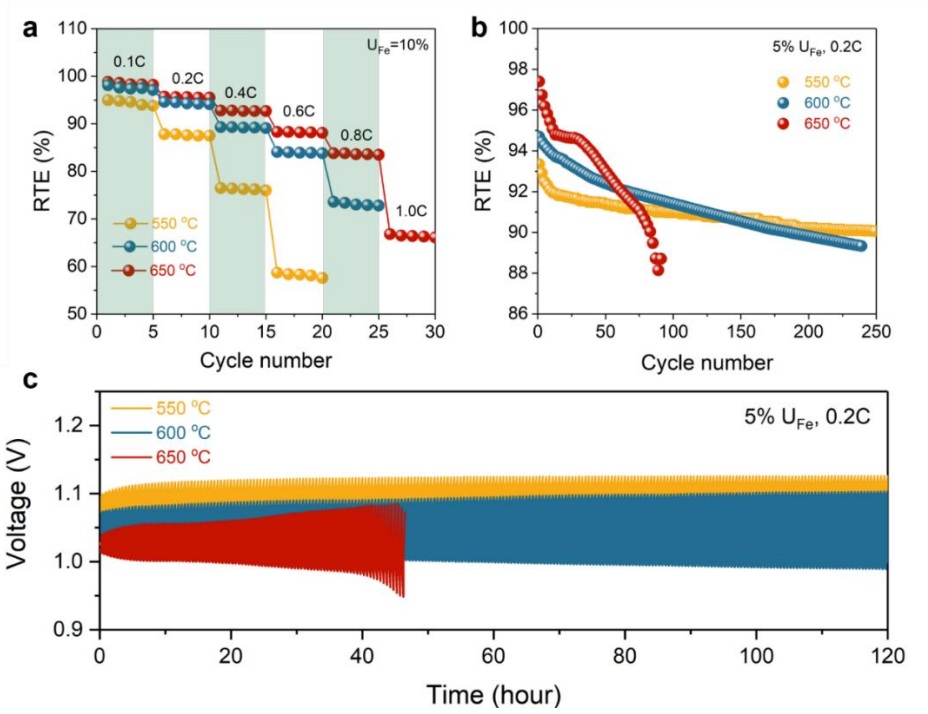

Figure 3.20 Battery performance tested at different T: (a) RTE *vs.* C-rate; (b) RTE *vs.* cycle number at U_{Fe}=5% and 0.2 C; (c) voltage profiles at U_{Fe}=5% and 0.2 C.

discharge and charge SED (CSED) (based on Fe mass) increase, *e.g.* discharge SED (DSED) of 63.8, 254, 628.1 and 1,012 Wh kg^{-1}-Fe at U_{Fe} of 5, 20, 50 and 80%, respectively. The deviation between the theoretical and experimental values increases with U_{Fe}, which reflects the mass transport limitation. It is also noted that RTE deceases from 92.5 to 73.7% when U_{Fe} is increased from 5 to 100%.

3.7 Temperature Effect on the Battery Performance

Knowing the effect of temperature (T) on battery performance can help determine the operational boundaries in practical applications. Figure 3.20 shows the SOIAB performance from 550 to 650 ºC for RSOFC with 2 wt.% GDC in the HE substrate. With increasing T, Figure 3.20a shows an improved rate performance and RTE at a fixed U_{Fe}=10%. At T=650 ºC, the battery can operate at 1.0 C before reaching the cutoff voltage, while it is not the case for 550 ºC. Temperature-enhanced kinetics of RSOFC

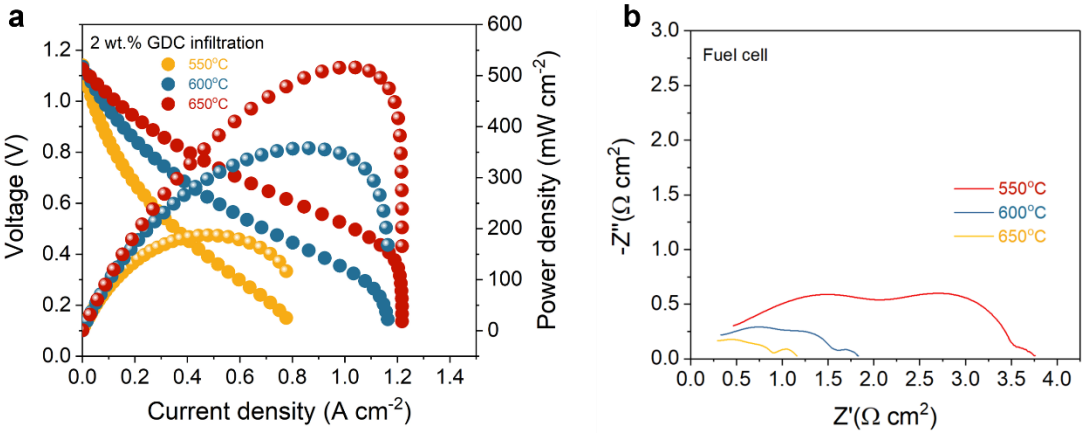

Figure 3.21 Electrochemical performance of RSOFC with 2 wt.%GDC added in HE vs. T: (a) V-I curves and (b) EIS spectra.

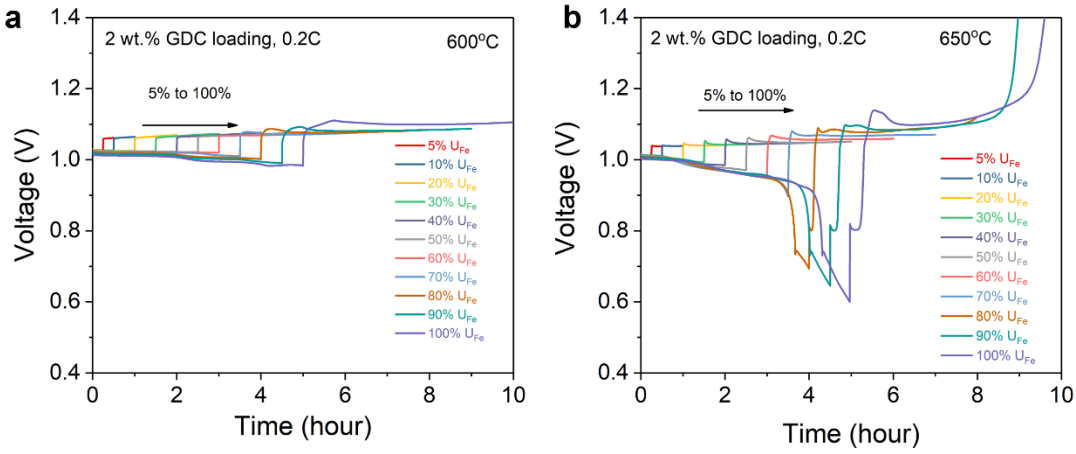

Figure 3.22 Profiles of discharge/charge at different U_{Fe} and different T for the 2 wt% GDC added cell: (a) 600 ºC and (b) 650 ºC.

(see Figure 3.21) and Fe-bed is undoubtedly the underlying reason.

However, higher temperature clearly has a negative effect RTE. Compared to Figure 3.19c, Figure 3.22 shows that RTE at 650 ºC suffers an accelerated decrease at U_{Fe}>60%, while it did not happen at 600 ºC until U_{Fe}>90% and at 550 ºC until U_{Fe}>80%. The stability of the battery tested at 0.2 C and U_{Fe}= 5% is further illustrated in Figure 3.20b and 3.20c, where RTE *vs.* cycle number and voltage-profile *vs.* cycle hour are shown, respectively. It is evident that higher temperature yields a higher initial RTE but

deteriorates the stability at a higher rate. Note that variations in V-profile are the results of different Fe/FeO_x redox potentials *vs.* temperature[xx] and partial Fe-bed sintering at higher T. To support the latter point, we performed SEM examination on the Fe-bed after testing. Figure 3.23 shows the results, where the degree of agglomerations of the material increases with temperature.

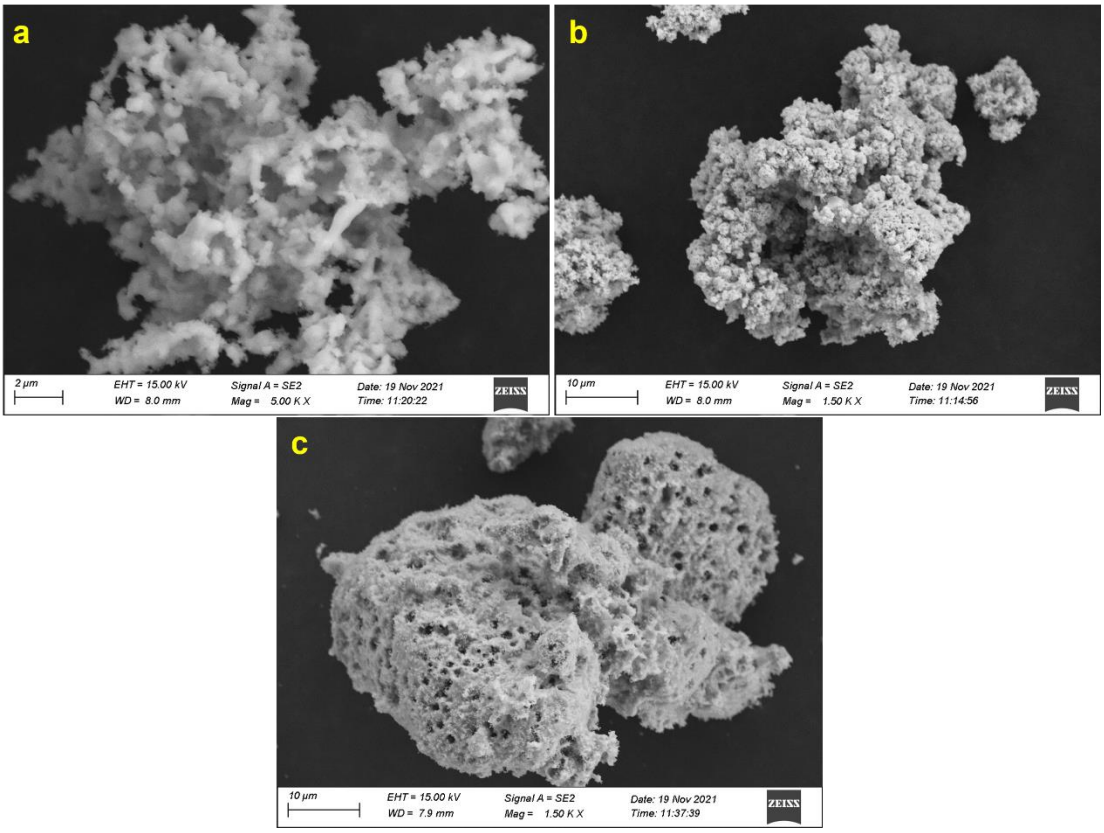

Figure 3.23 SEM images of Fe-bed material after cycling at 5% U_{Fe} and 0.2 C: (a) 550 ^oC, (b) 600 ^oC and (c) 650 ^oC.

A possible reason for poor reversibility at higher U_{Fe} is likely related to the thicker FeO_x scale formed during the discharge on the surface of Fe particles. This thick FeO_x scale will make the full recharge (full FeO_x reduction) more difficult within a fixed time (charge duration), resulting in gradual accumulation of FeO_x phase, a decline of active Fe in the Fe-bed, thus causing gradual performance decay over cycling. At a lower U_{Fe},

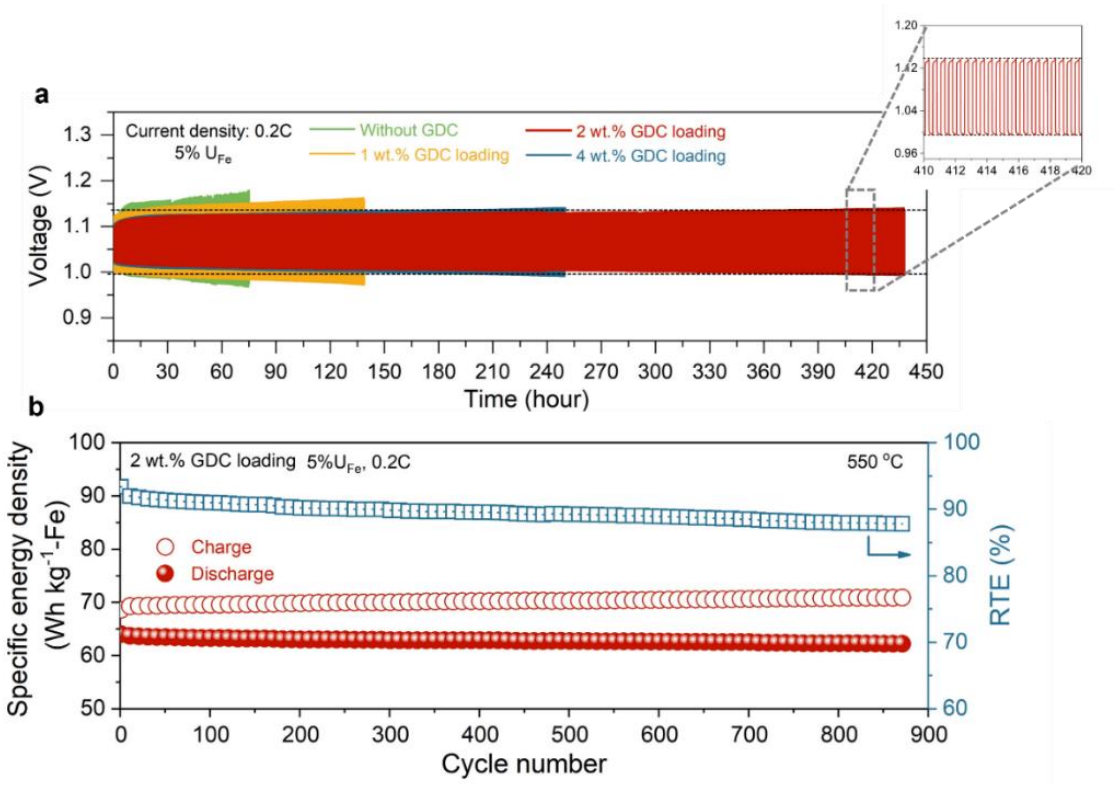

Figure 3.24 (a) Comparison of cycle stability of cells with different GDC loadings; (b) the corresponding SED and RTE of 2 wt.% GDC modified cell.

however, it is easier to fully reduce FeO_x back to Fe during the charging process due to the thinner (less) FeO_x formed during the discharging process. Therefore, selecting a reasonably low U_{Fe} for practical applications to achieve battery's longevity is not a bad choice as long as the energy storage materials are sufficiently cheap such as Fe. Overall, it seems that 550 ºC is a balanced operating temperature for SOIAB to achieve high RTE and better stability.

3.8 Long-Term Stability Evaluation of Battery

We, therefore, select 550 ºC for long-term stability testing. The results of the dip-coated SOIAB with different GDC loadings at 0.2 C (j=10 mA cm^{-2}) and U_{Fe}=5% are compared in Figure 3.24a. It is evident that 2 wt.% GDC-modified HE exhibits the best stability and highest efficiency compared to the 0, 1 and 4 wt.% counterparts. The corresponding

discharge and charge specific energy densities, (DSED and CSED, respectively) of a battery with 2 wt.%-GDC modified HE are given in Figure 3.24b, exhibiting DSED=63 and CSED=71 Wh kg^{-1}-Fe, respectively, retaining an RTE=88% even after 875 cycles.

3.9 Summary

In this chapter, we demonstrated SOIAB with significantly improved performance, moving this new battery a step further toward LDES applications. The performance improvement was realized through simultaneous optimizations in testing fixture, electrolyte, and electrodes. The use of three electrode configuration allows us to pinpoint the contribution of OE, through which the individual contribution from cell component is deconvoluted as a function of current density after combining with the battery cell voltage, ohmic resistance and Nernst potential. The finding is that HE contributes a majority of overpotential to the total cell voltage loss. Adding GDC catalyst into HE substrate significantly lowers the overpotential contribution of HE, thus further improving battery cell performance. With all the improvements made in cell, the characterization of battery performance further reveals excellent stability at low-C-rate and low-U_{Fe}. In general, C-rate has a more pronounced impact on cycle stability and RTE than U_{Fe}. Higher temperature in general promotes rate performance and RTE but again at a cost of cycle stability due to sintering of Fe-particles. Overall, given the excellent low C-rate performance and low-cost Fe, it is reasonable to regard SOIAB as a suitable LDES device. With large-size RSOFCs and more Fe-bed material loading, achieving 10+ hour electricity storage for SOIAB is straightforward.

CHAPTER 4

DESIGNING OF NEW IRON BED MATERIALS FOR ENERGY STORAGE UNIT

Qiming Tang, Morey Chaitali, Shichen Sun, Nansheng Xu and Kevin Huang, "$BaZr_{0.4}Ce_{0.4}Y_{0.1}Yb_{0.1}O_3$ (BZC4YYB) Mediated Energy Storage Materials Enabling Accelerated Kinetics in Solid Oxide Iron-Air Battery" to be submitted.

4.1 Introduction

In the previous chapter, the dip-coating method was used for fabricating Ni-ScSZ support cell, achieving a thin and dense electrolyte layer. In addition, the introduction of GDC nanoparticles into Ni-ScSZ anode increases TPBs and improves RSOFC stability and performance, which further improve SOIAB performance. However, the SOIAB still faces a challenge for low-temperature operation: sluggish kinetics of iron oxide reduction to Fe that limits the rechargeability, especially at high C-rates [17, 23, 78]. When the current density is over 30 mA cm^{-2}, RTE is decreased sharply because of the high overpotentials at SOFC and SOEC modes, resulted from low hydrogen and steam concentrations in the close system when the iron bed materials exhibit low redox reaction kinetics. A computational modeling study indicates that a battery with a Fe/Fe_3O_4 redox energy store at 550 °C becomes virtually non-rechargeable if operated at a current density of 15 mA cm^{-2} and Fe utilization (U_{Fe}) of 60% [79]. Therefore, promoting kinetics of iron oxide reduction to Fe is a key step to advance the development of reduced-temperature

SOIABs. Previous experimental work on improving the kinetics of Fe_3O_4 reduction has been primarily focused on increasing the surface area of Fe-based ESU materials[19, 21]. However, such nanostructured materials are still subject to coarsening during long-term operation, ultimately resulting in degradation. ZrO_2 support for iron bed materials has been proved to be a good inert phase in iron oxide, which can limit iron particles coursing during redox reaction repeatedly [80-82]. Other strategies to improve the redox kinetics, such as introducing proton conductor oxide support and catalyst have been reported [17, 83]. However, the fast decay and low RTE at high rates are still fundamentally limited by the slow kinetic rate of reduction that is unable to match the rate of electrolysis of RSOFC. Thus, A better solution is to develop ways of boosting the intrinsic kinetics of Fe_3O_4 reduction to Fe so that the rechargeability (reversibility) can be improved.

In this chapter, two types of new energy storage unit (ESU) materials were designed to enhance the reduction kinetics. The slow Fe_2O_3 reduction kinetics is significantly improved by IrO_2 nanoparticles in Fe-based ESU, achieving high cycle efficiency of 73% at high current density of 50 mA cm^{-2} (1 C). Furthermore, $BaZr_{0.4}Ce_{0.4}Y_{0.1}Yb_{0.1}O_{3-\delta}$ (BCZ4YYb), a proton-conducting perovskite, was also studied to replace ZrO_2 as a support for Fe particles in ESU. Compared to the traditional oxide support ZrO_2, this new support significantly enhances the kinetics of redox reactions, achieving a high round trip efficiency (RTE) of ~65% at 1.5C (75mA cm^{-2}). Even at U_{Fe}=20% and a current density of 20 mA cm^{-2}, the battery can yield a discharge energy density of 215 Wh kg^{-1}-Fe for 350 cycles with a RTE of 68%.

4.2 Experimental Methods

4.2.1 Materials Preparation

Fe_2O_3-ZrO_2 baseline Fe-bed material: it was prepared by a co-precipitation method as described in the previous chapter. Briefly, 0.0425mol $Fe(NO)_3$•$9H_2O$ (≥99.999%, Sigma-Aldrich) and 0.0075 mol $ZrO(NO)_2$•xH_2O (≥99.999%, Alfa-Aesar, x=2) were first dissolved in deionized water separately. It is worthy to mentioning that $ZrO(NO)_2$•xH_2O should be solved in 80mL DI water first, which provides an acid environment. Then the two solutions were mixed in a beaker with a cation concentration of 0.1 M. The resultant clear orange solution was then added dropwise to 1 L $(NH_4)_2CO_3$ (Sigma-Aldrich) solution bath under a constant stirring. To ensure a full precipitation of all cations in the solution, the molar ratio of $(NH_4)_2CO_3$ and Me+ (M= Zr and Fe) was kept as n $(NH_4)_2CO_3$: n Me^+=2.0 : 1. The resultant brownish precipitate was then left in the solution for 20 h with continuous stirring. Finally, the aged suspension was filtered and washed several times with DI water, dried overnight at 80 ºC and calcined in air at 600 ºC for 5h to yield the final product.

Fe_2O_3/ZrO_2-IrO_2 Fe-bed material: with the Fe_2O_3-ZrO_2 composite prepared above, it was first ball milled using a planetary ball mill (BM4X-04, COL-INT TECH) in a zirconium container for 20h with a milling speed of 300 rpm. Then, 0.1 g Ir precursor, iridium III 2,4-pentanedionate ($C_{15}H_{21}IrO_6$, Sigma-Aldrich) was dissolved in 2mL acetone (99.5%, Sigma-Aldrich). Subsequently, the obtained solution was added into 1 g of milled Fe_2O_3-ZrO_2 powders in an agata mortar followed by grinding. Finally, the impregnated powders were calcined at 600 ºC for 2h. The total IrO_2 loading in the ESU is around 4 wt.% of Fe_2O_3-ZrO_2.

Fe_2O_3-BZC4YYb Fe-bed by impregnation: $BaZr_{0.4}Ce_{0.4}Y_{0.1}Yb_{0.1}O_{3-\delta}$ (BZC4YYb) powders were prepared by a solid-state reaction (SSR) method. Briefly, $BaCO_3$ (Sigma Aldrich, ACS Reagent, ≥99%), CeO_2 (Acro's Organics, 99.9%), ZrO_2 (Alfa Aesar, 99.7%), Y_2O_3 (Alfa Aesar, 99.9%), and Yb_2O_3 (Sigma Aldrich, 99.9%) were mixed according to their stoichiometries and ball milled with ethanol for 24 h at a milling speed of 300 rpm followed by drying in oven. Then the milled powders were calcinated in the air and kept at 900 ^oC for 10h. Subsequently, the obtained powders were crashed and milled by a micronizing mill (McCrone) for 30 min. The crashed powders were then pressed into disk with diameter of 20 mm and thickness of 1 mm followed by calcination at 1350 ^oC for 10h. The extra powders were used to cover the pellet to compensate Ba-loss during sintering. This milling-pressing-calcination process was repeated twice to remove carbonates and obtain a pure perovskite. The Fe_2O_3 infiltrated BZCYYb materials were prepared by incipient wetness impregnation with $Fe(NO_3)_3 \cdot 6H_2O$ (99%, Alfa Aesar) as precursor. A 0.1 M of acetone (99.5%, Sigma-Aldrich) solution of $Fe(NO_3)_3 \cdot 6H_2O$ was used for the impregnation. The impregnated samples were calcined at 600 ^oC for 2 h before use. The total Fe_2O_3 loading relative to BZC4YYb is 1:1.

Fe_2O_3-BZC4YYb Fe-bed material by mechanical mixing: 3.25g iron oxide nanoparticles (Fe_2O_3, 99.5%, US Research Nanomaterials, Inc.) and 1.1g milled BZC4YYb powders were mixed/milled using ethanal (100%, Sigma-Aldrich) as medium in a planetary ball mill (BM4X-04, COL-INT TECH) with a zirconium container for 20h at a milling speed of 300 rpm. Then the mixture was dried in 80 ^oC to obtain final powders.

4.2.2 Battery Fabrication and Testing

The battery was fabricated by similar method mentioned in Chapter 3. For RSOFC, a mixture ink of LSM, BYC and a V-006 binder (Columbia International) in a weight ratio of LSM:BYC:V-006 = 40:60:200 was screen printed on top of ScSZ thin film electrolyte supported on Ni-ScSZ infiltrated with 4 wt.% GDC nanoparticles. Then the prepared iron bed materials were placed in the battery chamber followed by sealing with glass powder (melting point: 680 ^{o}C, Schott GM31107). The electrochemical performance of the battery was tested using a Solartron Multichannel system (model 1470e) coupled with a Solartron 1255 frequency response analyzer. The pre-treatment of battery is the same as that described in Chapter 3. The OCV, V-I curves and EIS of the RSOFC were first measured for both of open and close system. Then the rate performance, utilization of iron bed (U_{Fe}) and long-term stability were systematically carried out based on the protocol listed in Table D.1 in Appendix D. The cutoff voltages for discharge and charge are set at 0.8 and 2.0 V, respectively.

4.2.3 Materials Characterization

The phase compositions of the prepared iron bed materials were examined by X-ray diffraction operated at a scan rate of 5^{o} min^{-1} from 10 to 80^{o} using Rigaku D/MAX-2100. The morphologies of the Fe-bed materials and battery cell components were examined by an ultra-high resolution field emission scanning electron microscope (UHR-FESEM) (HITACHI, Regulus 8230) with Energy Dispersive X-Ray Spectroscopy (EDS) for elemental mapping analysis. A high-resolution transmission electron microscope (HRTEM, HITACHI H-9500) and scanning transmission electron microscope (STEM, HITACHI SU9000) was also used to examine the element distribution in the prepared

iron bed materials. Temperature-programmed reduction (TPR) studies were performed using 10% hydrogen H_2/Ar to gauge the reduction kinetics of new iron bed materials. The consumption of H_2 was measured by the change in thermal conductivity of the effluent gas stream, and a dry ice bath was used to remove water formed during the hydrogen reduction. A ~30 mg as-prepared iron bed material sample was placed in a quartz tube and signal was collected at a different temperature ramp of 2.5, 5, 10 and 15 ºC /min from 100 to 900 ºC.

4.3 IrO_2 Impregnated Fe_2O_3/ZrO_2

Engineering active catalyst on the surface of a redox material can effectively promote the kinetics of the underlying redox reaction. To date, many studies have been devoted to the development of catalytic formulation in the metal/metal oxide redox process, Metals such as Ru, Pd, Mo, and Cr have been previously reported as promising catalysts for hydrogen chemical looping with Fe as the active redox metal [84-86]. Zhang et al. reported a significant enhancement in the reversibility of a low-temperature SOIAB operated under a range of rate capacity and iron utilization by dispersing fine particles of catalytic Pd into the Fe-based ESU [17]. However, a major barrier for this process development is the rapid decay of catalytic effect caused by segregation, especially at high temperatures. To enhance the redox kinetics, IrO_2 nanoparticles as catalyst were blended on the Fe_2O_3/ZrO_2 ESU materials surface by wet impregnation, which shows a significant improvement of rechargeability of the battery compared to without IrO_2.

4.3.1 Phase Composition and Structural Analysis

The phase purity of the as-prepared Fe_2O_3/ZrO_2 and IrO_2-impregnated Fe_2O_3/ZrO_2 are examined by XRD; the XRD patterns are shown in Figure 4.1. The pristine Fe_2O_3/ZrO_2

powders show peaks at around 24º, 33.2 º, 25.6 º, 40.8 º, 49.5 º and 54.1 º, which are assigned to (012), (104), (110), (113), (024) and (116) planes of Fe_2O_3 (PDF # 33-0664). The sharp peaks without any impurity phase reveal a high crystallinity and purity of sample prepared by-coprecipitation process. Meanwhile, after the introduction of IrO_2, a wide weak peak at 28.1 º can be indexed to (110) plane of IrO_2, suggesting IrO_2 was blended into Fe_2O_3/ZrO_2. However, the intensity and shape of each peak of the sample are weaker and broader, implying that some IrO_2 particles with low crystallinity distributed on the surface of Fe_2O_3/ZrO_2, which can be also seen in the TEM images of as-prepared IrO_2-added Fe_2O_3/ZrO_2 sample in Figure 4.3.

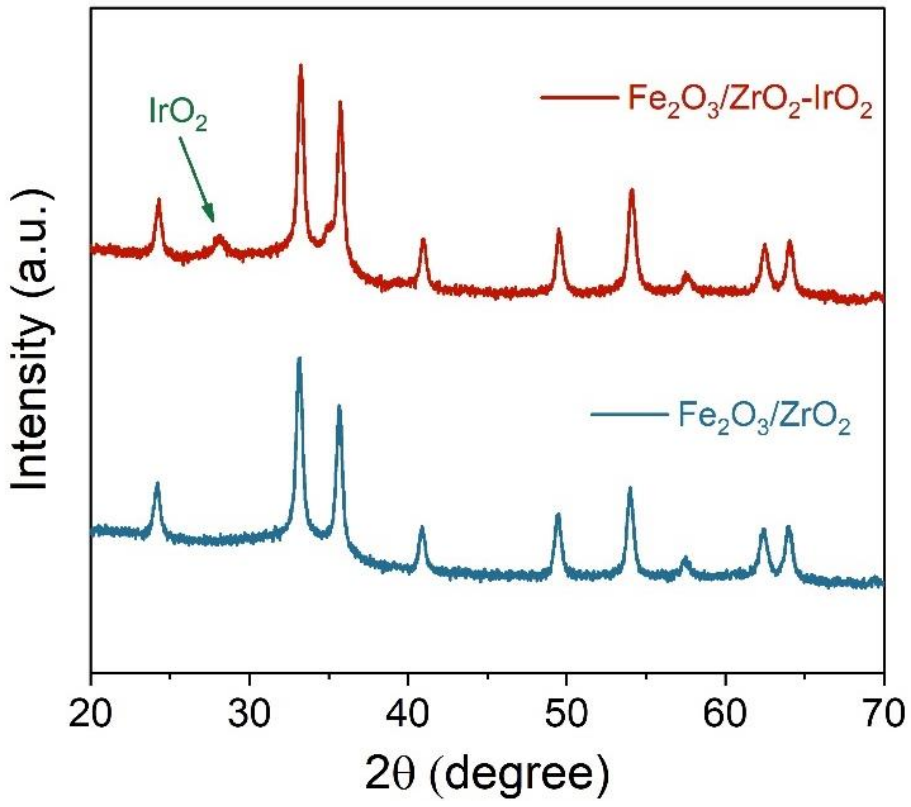

Figure 4.1 XRD pattern of as-prepared pristine Fe_2O_3/ZrO_2 and IrO_2-added Fe_2O_3/ZrO_2.

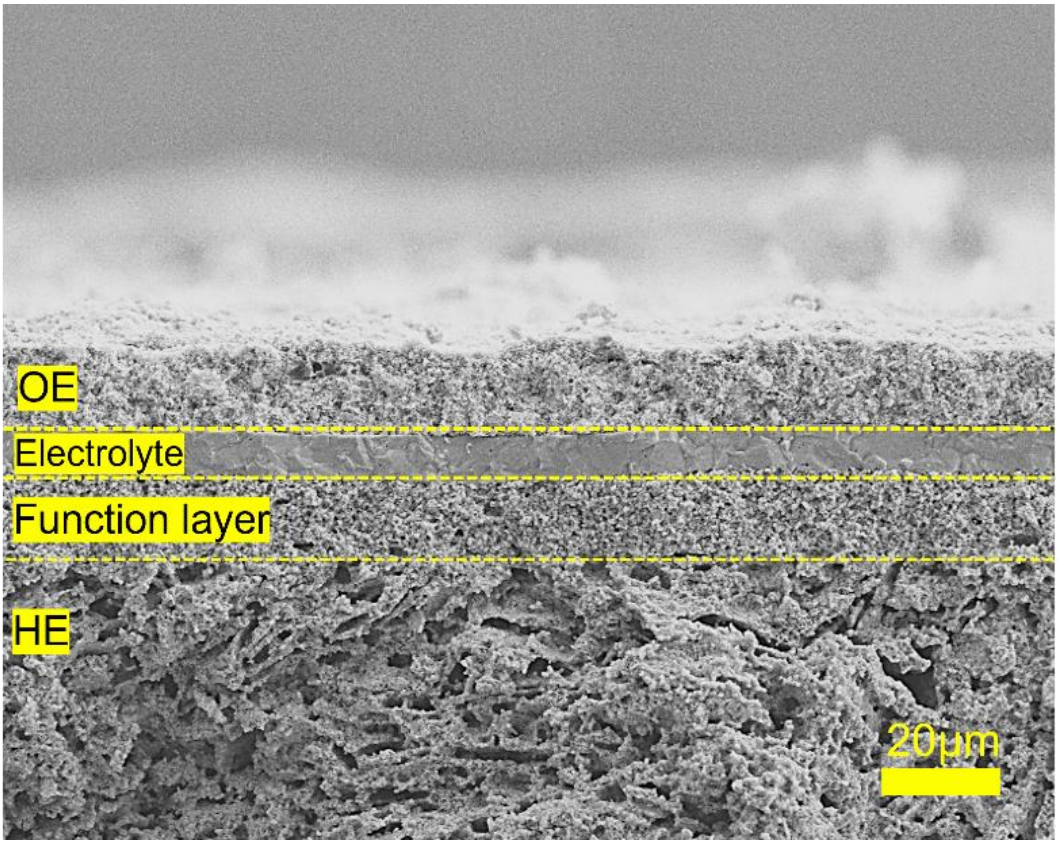

Figure 4.2 SEM images of HE-supported full cell made by dip-coating.

Figure 4.2 shows the cross-sectional view of microstructure in the dip-coated HE-supported full cell after reduction in H_2-3% H_2O at 550 ºC. Here, 2 wt.% GDC of HE was infiltrated in the electrode as mentioned in Chapter 3 to improve the electrochemical performance and stability of RSOFC. A 10-μm thick, dense ScSZ electrolyte and 15-μm thick, porous HE functional layer are clearly seen on the HE-support. The LSM/BYC (a weight ratio of LSM:BYC=4:6) mixed ionic and electronic conductor (MIEC), as OE active material, was screen printed on the ScSZ surface with a 18μm thickness. The pores distribute evenly in the HE.

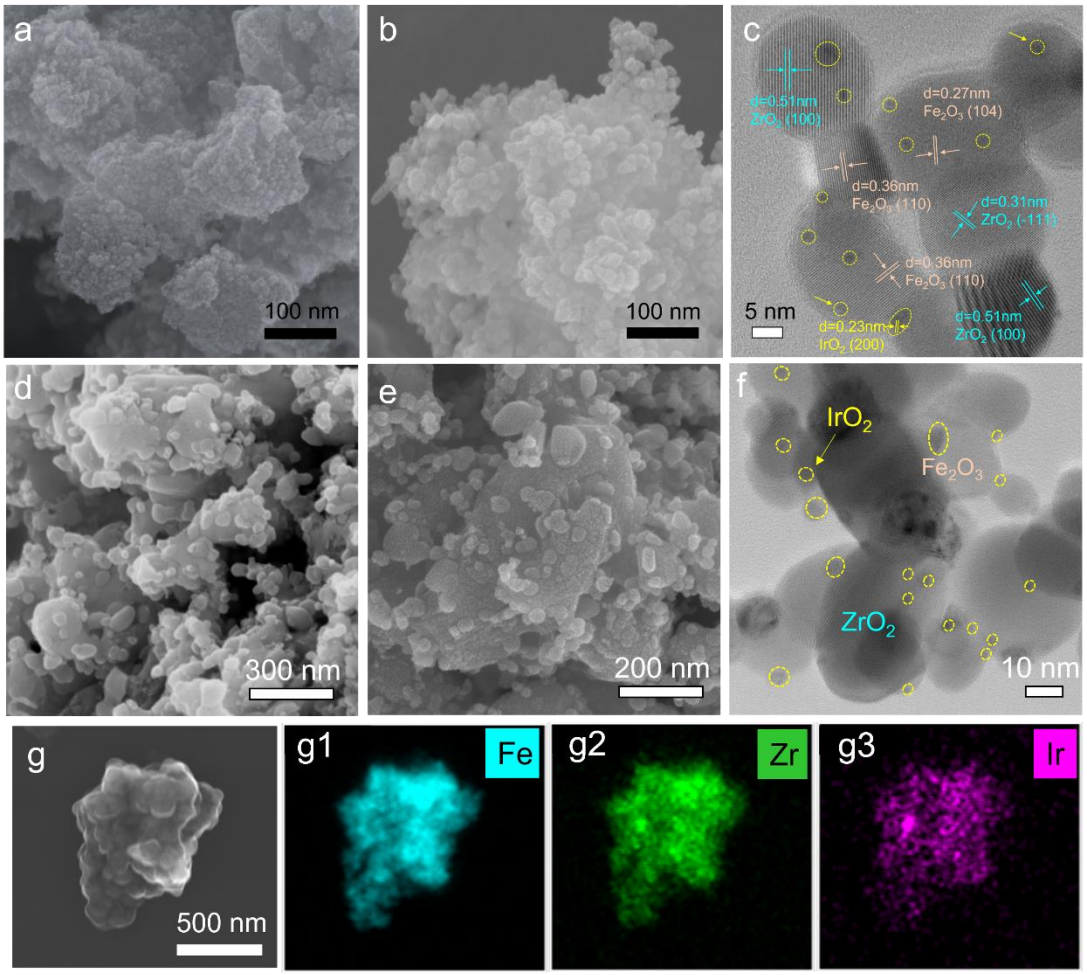

Figure 4.3 Characterization of Fe_2O_3/ZrO_2 and Fe_2O_3/ZrO_2-IrO_2 Fe-bed materials: (a) SEM image of fresh Fe_2O_3/ZrO_2; (b) SEM image of fresh Fe_2O_3/ZrO_2-IrO_2; (c) HRTEM image of fresh Fe_2O_3/ZrO_2-IrO_2; (d) SEM image of Fe_2O_3/ZrO_2 after 100h testing; (e) SEM image of Fe_2O_3/ZrO_2-IrO_2 after 100h testing; (f) HRTEM image of Fe_2O_3/ZrO_2-IrO_2 after 100h testing; (g) elemental mapping of Fe_2O_3/ZrO_2-IrO_2 after 100h testing: (g1) Fe, (g2) Zr, (g3) Ir.

SEM images of pristine Fe_2O_3/ZrO_2 powders in Figure 4.3a show that there is a slight agglomeration of pristine Fe_2O_3/ZrO_2. However, the IrO_2 added Fe_2O_3/ZrO_2 shown in Figure 4.3b exhibits that Fe_2O_3/ZrO_2 particles are discretely and uniformly covered with IrO_2 nanoparticles (NPs) in an average diameter of ~20 nm with nanochannels for the diffusion of hydrogen and steam during redox reaction. In addition, the high-resolution TEM (HRTEM) was also employed to explore the crystalline nature. The

regular crystalline fringes are clearly observed in Fe_2O_3/ZrO_2-IrO_2 in Figure 4.3c, where the lattice spacings of 0.51, 0.31, 0.36, 0.27 and 0.23 nm match well with the (100) and (-111) planes of ZrO_2, (110) and (104) planes of Fe_2O_3, and (200) plane of IrO_2, respectively. The IrO_2 NPs uniformly distribute on the surface of Fe_2O_3, providing catalytic sites for the redox reaction by H_2 "spill over" effect [87]. After cycling testing, all particles in Fe_2O_3/ZrO_2 without IrO_2 grew from 50 to 200 nm as expected, see Figure 4.3d. On the contrary, Figure 4.3e shows that the IrO_2 added Fe_2O_3/ZrO_2 exhibits similar morphologies, but the HRTEM in Figure 4.3f confirmed that the IrO_2 and ZrO_2 NPs still distribute uniformly on the Fe_2O_3 surface. The elemental mapping shown in Figure 4.3g confirms that Fe, Zr and Ir still distribute uniformly within the Fe-bed and there is no apparent Fe segregation to the surface as previously observed.

4.3.2 Understanding the Mechanism of IrO_2-Enhanced Iron Oxide Reduction Kinetics

To evaluate the reduction kinetics of Fe_2O_3/ZrO_2 after introducing IrO_2, temperature program reduction (TPR) was carried out on the as-prepared samples. By analyzing reduction temperature using the TPR peaks, some information on reduction kinetics can be gained. Figure 4.4 shows the TPR profiles of different samples. The pure Fe_2O_3 exhibits two peaks located at 416 and 641.4 ^oC, which can be assigned to the reduction of Fe_2O_3-to-Fe_3O_4 and Fe_3O_4-to-Fe. After adding ZrO_2, the second peak splits into two peaks, implying the FeO intermediate phase is present during reduction. The decreasing of reduction peak could be attributed to the ZrO_2 inert phase limiting the iron coarsening. On the contrary, the Fe_2O_3/ZrO_2-IrO_2 shows the fastest reduction kinetics by hydrogen as it exhibits the lowest reduction peak temperature, demonstrating the catalytic activity of IrO_2 nanoparticles to Fe-oxide reduction. It is worthy to noting that the sharp peak

located at 129.6 °C is indexed to the reduction of IrO_2 with hydrogen.

In addition, TPR can be also used to obtain activation energy of the reduction process of metal oxide, such as Fe_2O_3, based on the Kissinger's method [88]. For the peak temperature, T_{max}, of a TPR profile, the following equation holds:

$$\ln\left(\frac{\Phi}{T_{max}{}^2}\right) = -\frac{E}{RT_{max}} + \ln\left(\frac{AR}{E}\right) + C \tag{4.1}$$

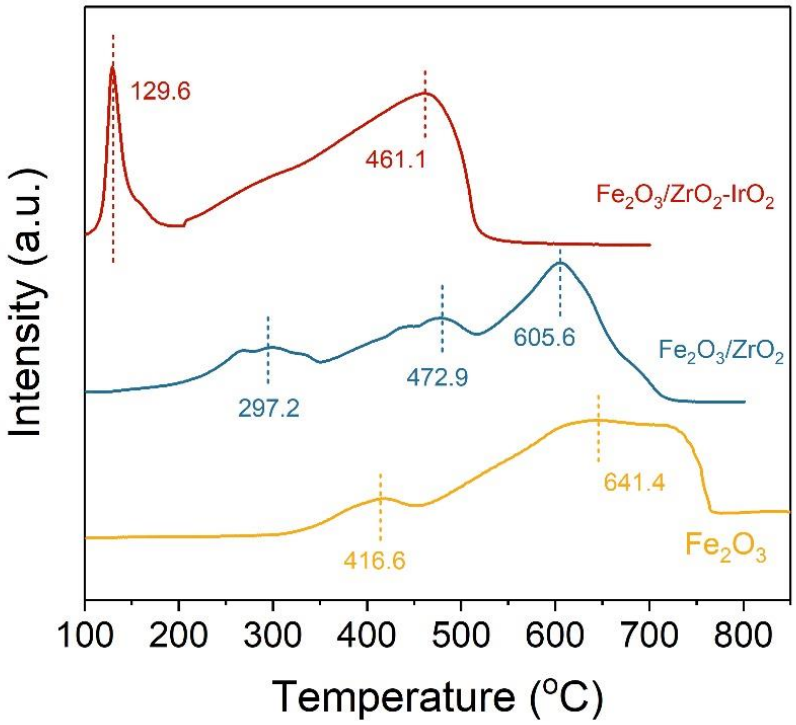

Figure 4.4 TPR profiles of different samples at a ramping rate of 10 °C/min: Fe_2O_3 (bottom); Fe_2O_3/ZrO_2 (medium) and Fe_2O_3/ZrO_2-IrO_2.

Where Φ is the ramping rate, E is the activation energy of reduction process, C is a constant, A is the pre-exponential term, R is the universal gas constant. Since E is a constant for a fixed process, by plotting $\ln\left(\frac{\Phi}{T_{max}{}^2}\right)$ *vs.* $\frac{1}{T_{max}}$, the slope (-E/R) can be calculated by fitting the Arrhenius plots.

Figure 4.5a and 4.5b show obtained TPR profiles with different heating rates from

2.5 to 15 °C/min for Fe_2O_3/ZrO_2 and Fe_2O_3/ZrO_2-IrO_2. Small changes in peak shape can be observed, especially at the ramping rate, due to the changes in the reduction mechanism. The T_{max} value was extracted from Figure 4.5a and 4.5b. From the slope of Figure 4.5c, the activation energy E_a is obtained. The Fe_2O_3/ZrO_2-IrO_2 shows lower E=34.9 kJ mol^{-1} than Fe_2O_3/ZrO_2 (81.5 kJ mol^{-1}), further suggesting that IrO_2 can boost significantly the Fe_2O_3-reduction kinetics.

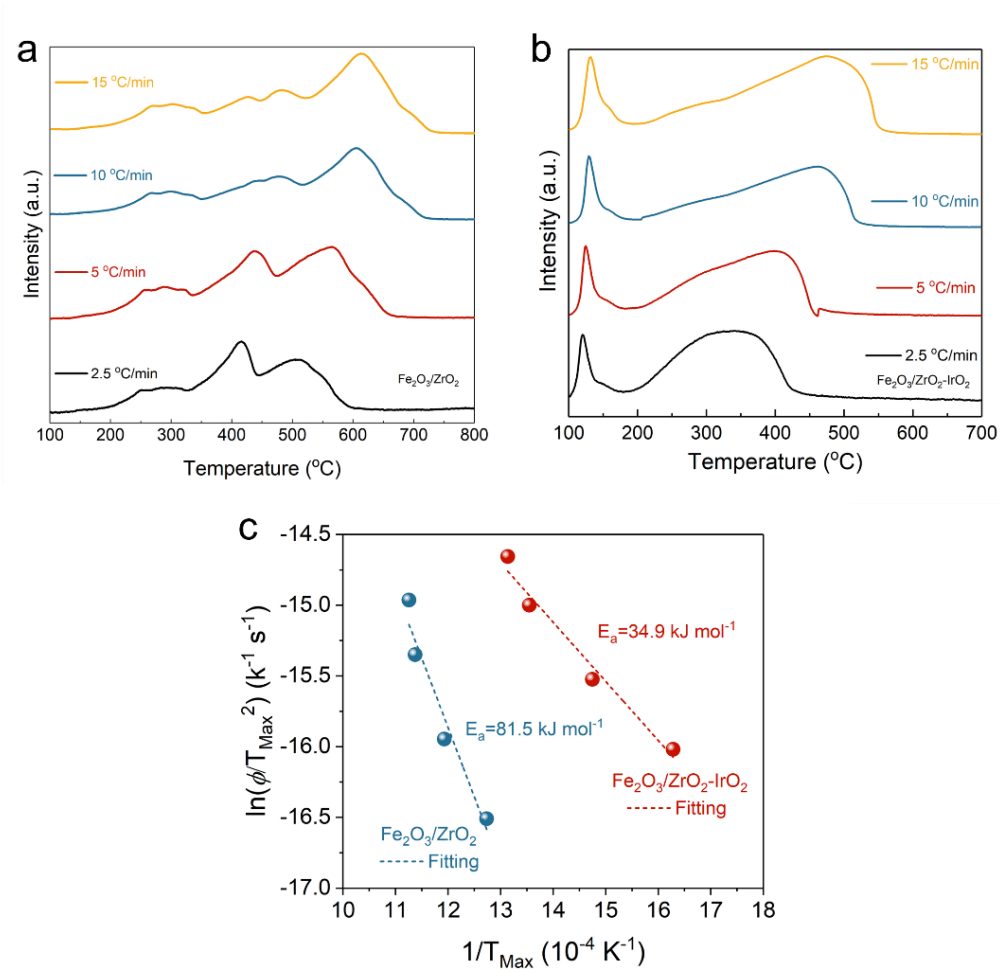

Figure 4.5 TPR profiles under different ramping rates for (a) Fe_2O_3/ZrO_2; (b) Fe_2O_3/ZrO_2-IrO_2; (c) Arrhenius plots to extract E_a.

4.3.3 Evaluation of Electrochemical Performance

To evaluate the performance of SOMAB with IrO_2 added Fe_2O_3/ZrO_2 ESU materials,

0.1g of as-prepared powders (with a Fe mass of 56 mg) was placed into battery chamber. The electrochemical performance was first tested. Figure 4.6a shows the variation of OCV *vs.* time in H_2-3%H_2O in open system. After full reduction, the cell exhibits a OCV of 1.144 V, which is close to the theoretical potential, suggesting a good gas tightness of the system. Then the performance of RSOFC was tested in a closed system, where the H_2 inlet and outlet were closed. Figure 4.6b shows the V-*j* curve in both fuel cell and electrolyzer modes at close system, where the OCV of battery is seen to decrease to ~1.06 V in close system; 1.067 V is an equilibrium voltage for Fe-Fe_3O_4 redox couple at 550 ^oC, signifying the oxidation of Fe into Fe_3O_4.

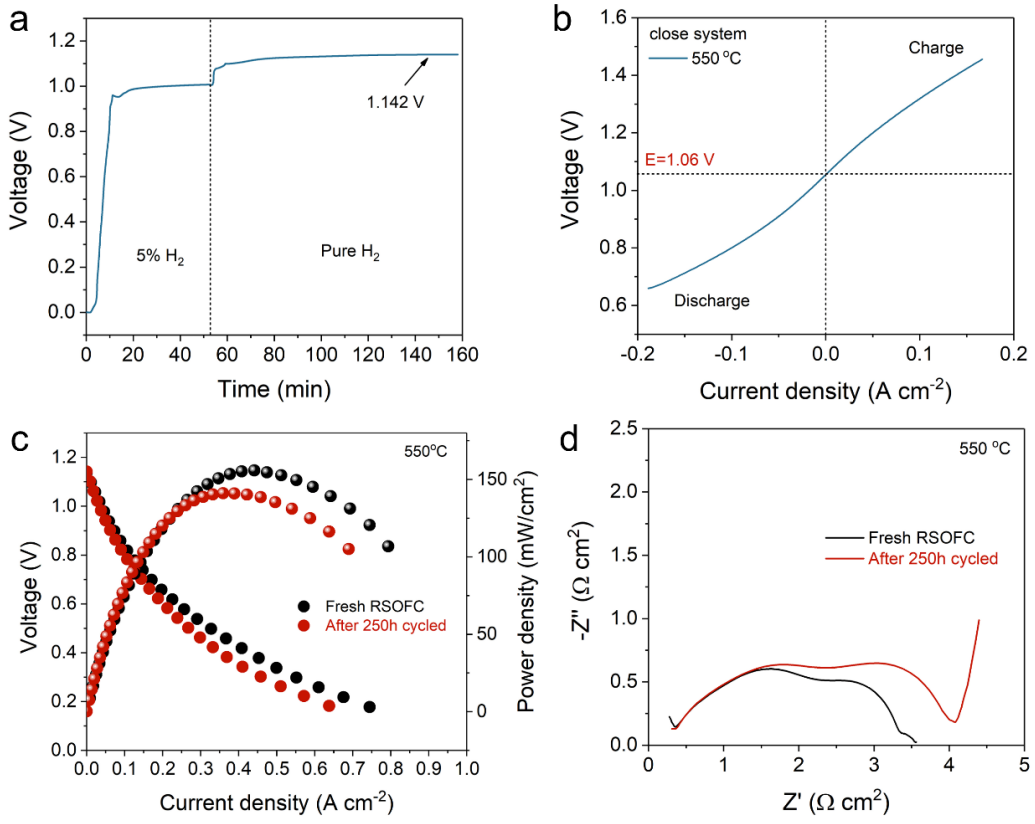

Figure 4.6 Electrochemical performance of RSOFC of battery with Fe_2O_3/ZrO_2-IrO_2 (a) A profile of OCV *vs.* time during reduction process in open system; (b) V-I curve of battery in close system; (c) Current-voltage and current-power curves and (d) EIS spectra with H_2/3% H_2O as fuel before and after cycling testing in open system.

The current-power curves in open system are shown in Figure 4.6c, where voltage is approximately linear with current density without obvious concentration polarization even at a current density of j = 750 mA cm^{-2} at 550 ºC, suggesting an enough porosity and tortuosity for RSOFC. The cell delivers a maximum power density (MPD) of 155 mW cm^{-2} at 550 ºC. After 250h discharge testing at a current density of 10 mA cm^{-2}, the MPD still can reach 145 mW cm^{-2}, suggesting excellent stability at low current density. After cycling testing, the EIS spectrum shown in Figure 4.6d indicates that the low-frequency parts enlarge, implying a possible change in microstructure [89].

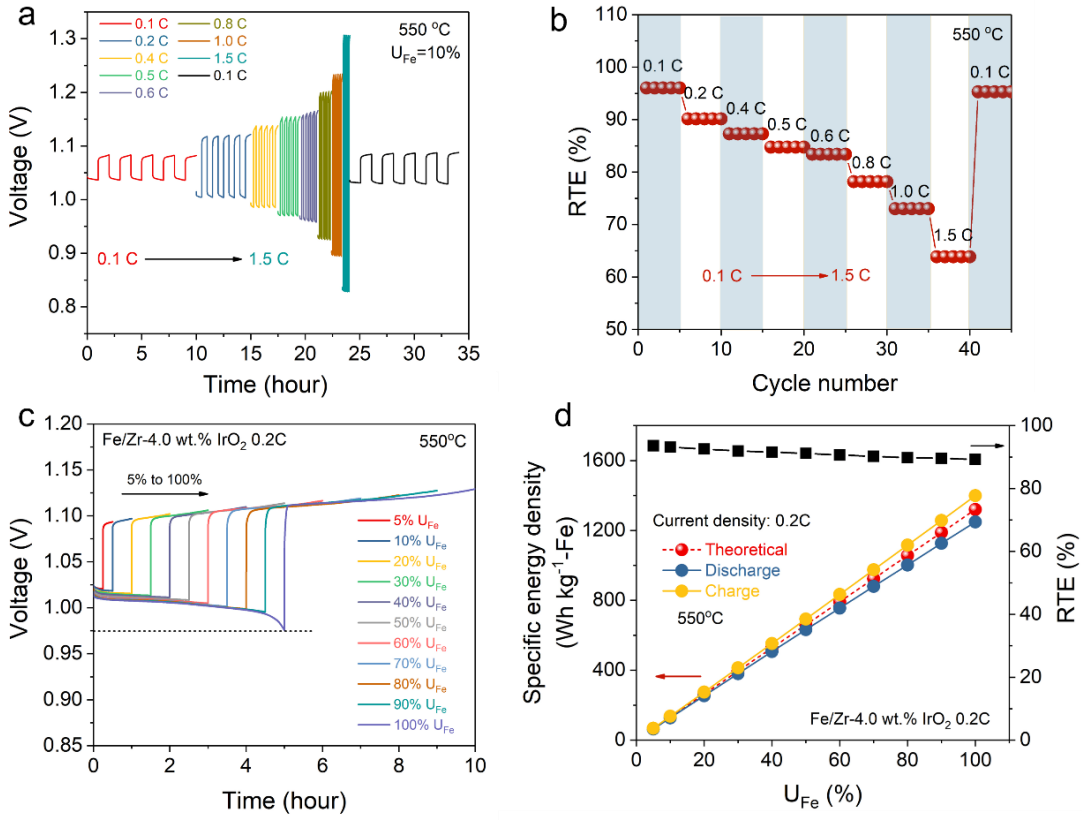

Figure 4.7 Electrochemical performance for SOIAB with IrO_2 added Fe_2O_3/ZrO_2 ESU materials: (a) Voltage profiles under different current density with a fixed U_{Fe}=10%; (b) RTE *vs.* C-rate; (c) voltage profiles *vs.* time at a fixed j= 10 mA cm^{-2} (0.2 C) and different U_{Fe} (5-100%); (d) discharge and charge specific energy density and corresponding RTE *vs.* U_{Fe}.

Figure 4.7a displays the voltage profiles at different C rates and Figure 4.7b shows the effect of C-rate varying from 0.1 C (5 mA cm^{-2}) to 1.5 C (75 mA cm^{-2}) on round-trip efficiency (RTE) at a fixed U_{Fe}= 10%. The battery with IrO_2 added Fe_2O_3/ZrO_2 ESU materials can achieve an RTE= 63% at 1.5 C, while the Fe_2O_3/ZrO_2 without IrO_2 can only reach to 0.6C with a low RTE of 58% (see Figure 3.19). When the C-rate returns to 0.1 C, a high RTE=95.8% is still achievable. After introducing IrO_2, more activation sites are achieved, thus the redox kinetics of iron bed materials are boosted significantly, resulting in lower polarization at higher current density. The iron utilization (U_{Fe}) of the SOIAB is of critical importance to RTE and energy capacity to be stored. Figure 4.7c shows voltage profiles at different U_{Fe} under a fixed j=10 mA cm^{-2} (0.2 C). All utilization testing was performed in one battery and only one cycle for each U_{Fe}. The dis/charge voltage range was set to be 0.6-2.0 V to keep battery from over dis/charge. The discharge voltage experiences a slight decrease at the end of discharge for fully discharge, while it can cycle with a stable voltage at U_{Fe} from 5 to 100%. Again, no obvious "voltage drop/rise" in the battery with Fe_2O_3/ZrO_2-IrO_2 can be seen, suggesting sufficiently fast kinetics of the redox reaction even at high U_{Fe}; the latter is critically important to provide fast enough H_2 and H_2O for the RSOFC to perform discharge and charge cycle. The discharge and charge specific energy density and RTE are shown in Figure 4.7d *vs.* U_{Fe}. As expected, both discharge and charge specific energy density increase with U_{Fe}, e.g., the discharge specific energy reaches 254.2, 631.8, and 1248.8 Wh kg^{-1}-Fe at U_{Fe} of 20, 50, and 100%, respectively. Even at U_{Fe}=100%, the RTE can hold 89.3%.

To evaluate the long-term stability, the as-fabricated battery was cycled at U_{Fe}=5% and a current density of 10 mA cm^{-2} (0.2 C). The results are shown in Figure 4.8. The

discharge/charge voltage remains ~1.0 V and 1.15 V, respectively, at the end of 500th cycle, see Figure 4.8a, which delivers a specific energy density (SED) of 65 Wh kg^{-1}-Fe with a high RTE of 91.5%, see Figure 4.8b, while the Fe_2O_3/ZrO_2 without IrO_2 shows a lower RTE of 89.5% (as shown in Chapter 3). The stable RTE over cycling implies is a result of implementing IrO_2 into the Fe-bed.

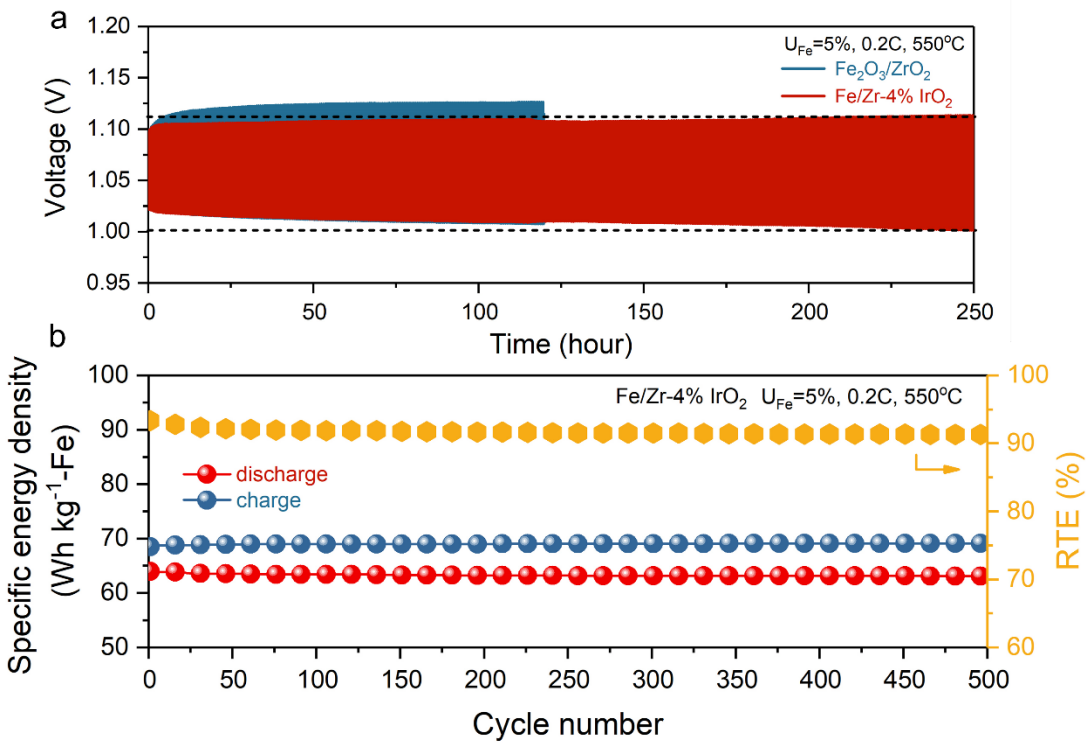

Figure 4.8 (a) Comparison of cycle stability of battery with different ESU materials; (b) the corresponding SED and RTE of Fe_2O_3/ZrO_2-IrO_2.

To demonstrate the feasibility for the practical applications, the battery with Fe_2O_3/ZrO_2-IrO_2 was further cycled at a higher current density, 0.4 C and a higher U_{Fe}=20% and 50%; the results are shown in Figure 4.9. Figure 4.9a and 4.9b show the cycling performance of this battery at a current density of 0.4 C and U_{Fe}=20%, which delivers a DSED of 240 Wh kg^{-1}-Fe and a CSED of the 297 Wh kg^{-1}-Fe with a RTE of 80.5%. However, compared to the low utilization testing, the discharge voltage decreases

slowly with time, while charge voltage increases faster with time in the high utilization testing, which can be attributed to the higher reduction degree of iron oxide could affect the reversibility. The same battery was again cycled at U_{Fe}=50% and a current density of 0.4 C (with a cycle duration of 1.25h) after generation in H_2-3%H_2O. As expected, Figure 4.9c and 4.9d show that higher utilization lead to higher energy capacity, for example, a DSED of 596 Wh kg^{-1}-Fe and CSED of 738 Wh kg^{-1}-Fe at U_{Fe}=50% with a RTE of 80.8%. It is worthy to noting that the RTE of battery depends more sensitively on current density than U_{Fe}.

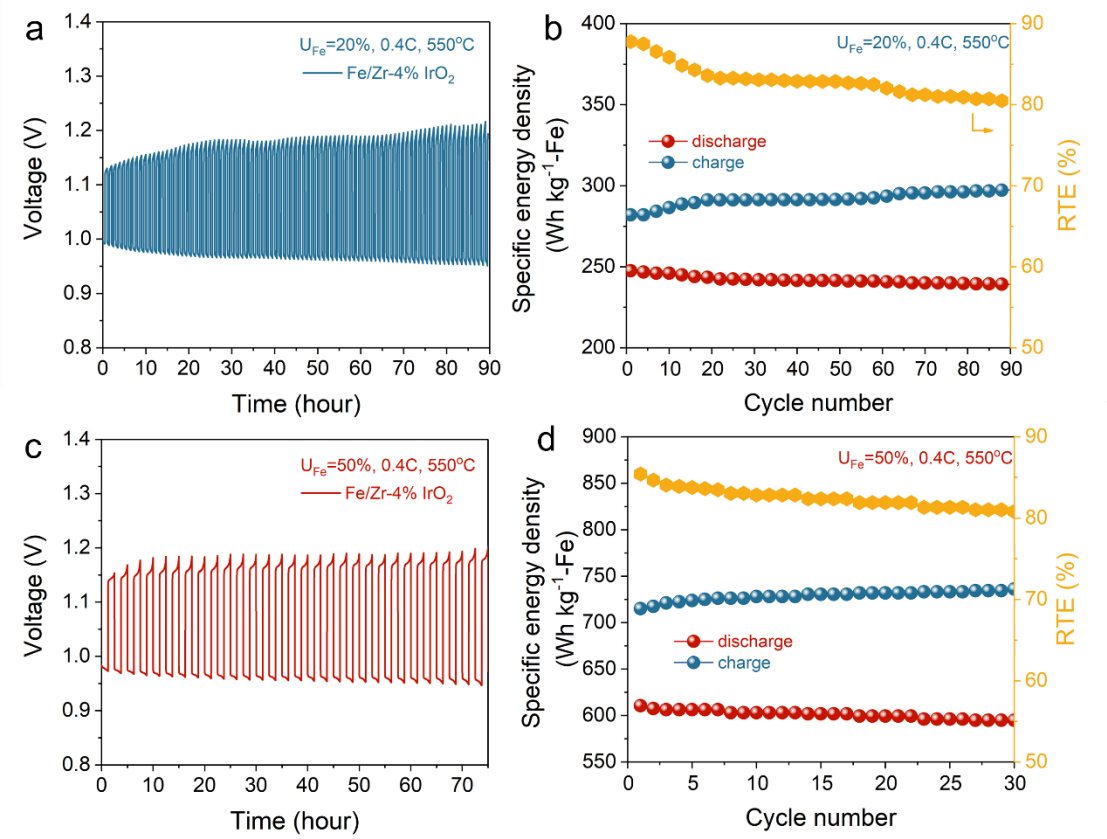

Figure 4.9 Cycling performance of a 550 °C battery with Fe_2O_3/ZrO_2-IrO_2 ESU materials at 0.4 C (20 mA cm^{-2}): (a) voltage profiles at U_{Fe}=20%; (b) the corresponding SED and RTE of U_{Fe}=20%; (c) voltage profiles at U_{Fe}=50%; (d) the corresponding SED and RTE of U_{Fe}=50%.

4.4 Proton Conductor as Fe-Supporting Oxide

To inhibit Fe-sintering during redox process and improve reversibility of iron bed materials, ZrO_2 has been extensively studied as an inert oxide supporting of iron bed materials [17, 20, 21]. However, the sluggish kinetics of iron oxide reduction by H_2 is still a major challenge. The catalyst introduction can boost the redox kinetics, but the high cost of noble metal, such as Pb, Ir etc., could potentially limit its practical application [17]. Proton conducting ceramic is an attractive electrolyte material for intermediate temperature SOFC since they exhibit not only adequate proton conductivity but also sufficient chemical and thermal stability under hydrogen and steam environment, especially in the Barium-Zirconium-Cerium-Yttrium-Ytterbium (BZCYYb) family [90-95]. Given their excellent stability in relevant hydrogen and water environments at high temperatures, BZCYYb has been reported as an iron-bed oxide support for SOIAB [83]. Xu et al. demonstrated that the battery with $BaCe_{0.7}Zr_{0.1}Y_{0.1}Yb_{0.1}O_{3-\delta}$ supported Fe_2O_3 exhibit improved iron utilization compared to ZrO_2 support [83]. However, the poor long-term stability and low RTE is still a challenge. Here, we investigate a more stable proton conductor, $BaZr_{0.4}Ce_{0.4}Y_{0.1}Yb_{0.1}O_{3-\delta}$ (BZC4YYb), used as the iron oxide support in performance improved RSOFC. Compared to the traditional oxide support ZrO_2, this new support significantly enhances the kinetics of redox reactions, achieving a high round trip efficiency (RTE) of ~75% at 1.5C (75mA cm^{-2}). Even at U_{Fe}=20% and a current density of 20 mA cm^{-2}, the battery can yield a discharge energy density of 225 Wh kg^{-1}-Fe for 350 cycles with a RTE value of 68%.

4.4.1 Phase Composition and Structural Analysis

Two methods, wet impregnation and ball milling, were used to prepare the BZC4YYb-

supported Fe_2O_3. The phase purity of the as-prepared Fe_2O_3/BZC4YYb by these two methods are confirmed by XRD in Figure 4.10. The BZC4YYb was synthesized by a facile solid-state method, and all positions of the diffraction peaks in the XRD spectrum are consistent with those reported in the literature [92]. After mixing with Fe_2O_3 by milling, the sharp peaks without any other impure peaks suggest excellent crystallinity and high purity. However, the Fe_2O_3 impregnated BZC4YYb exhibits weak and wide diffraction peaks, implying poor crystallinity and smaller iron oxide particles.

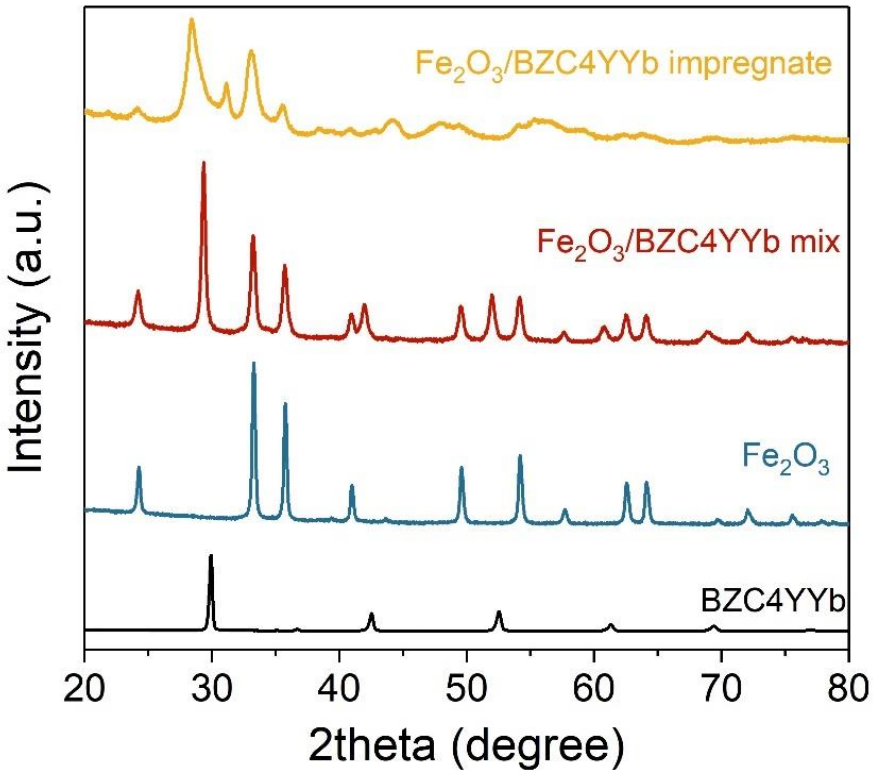

Figure 4.10 XRD patterns of as-prepared samples.

The cross-sectional SEM image in Figure 4.11a illustrates the RSOFC structure after reduction. A 10-μm thick, dense ScSZ electrolyte and 15-μm thick, porous HE functional layer are clearly seen on the HE-support. The LSM/BYC (a weight ratio of LSM:BYC=4:6) mixed ionic and electronic conductor (MIEC), as OE material, was

screen printed on the ScSZ surface with a 18µm thickness. The pores in a diameter of ~5 µm distributes evenly in the HE, which guarantees the hydrogen and steam diffusion during battery operation. The SEM images of as-prepared Fe_2O_3/BZC4YYb reveals a structure with uniform Fe_2O_3/BZC4YYb particles in an average size of ~25 nm, see Figure 4.11b and 4.11c. However, the Fe_2O_3 impregnated BZC4YYb shown in Figure 4.12a exhibits serious agglomeration, which could block gas diffusion during redox reactions. After 100 cycling testing at 550 °C, the mechanically mixed Fe_2O_3/BZC4YYb exhibits a slight aggregation, but a porous nanostructure remained, see Figure 4.11d. In addition, the corresponding elemental mapping analysis suggests all elements distribute uniformly within the Fe-bed.

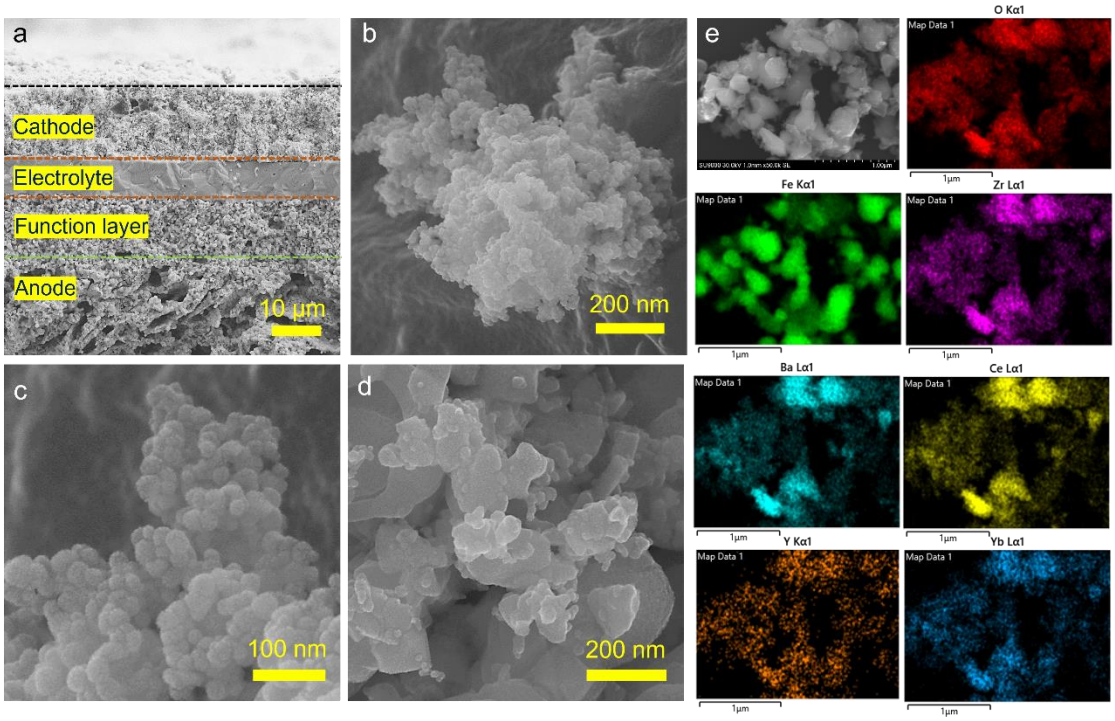

Figure 4.11 (a) Cross-sectional SEM image of RSOFC; (b) and (c) SEM images of fresh mechanically mixed Fe_2O_3/BZC4YYb; (d) SEM image of mechanically mixed Fe_2O_3/BZC4YYb after 100h testing; (e) corresponding elemental mapping after testing: O, Fe, Zr, Ba, Ce, Y and Yb.

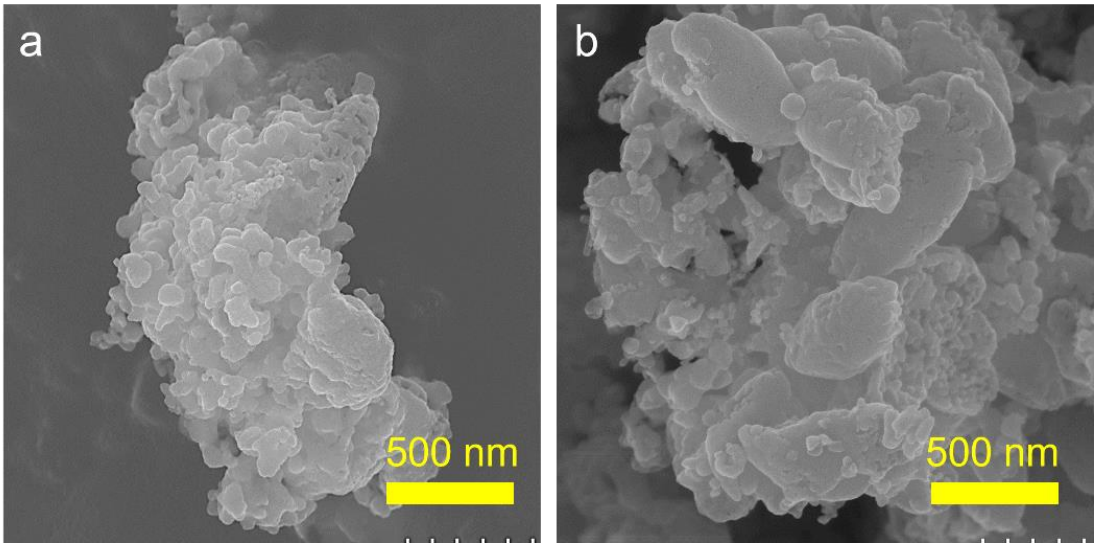

Figure 4.12 SEM images of Fe_2O_3 impregnated BZC4YYb: (a) fresh powders; (b) after 100h testing.

In contrast, more serious aggregation is seen in Figure 4.12b in Fe_2O_3-impregnated BZC4YYb, which is the result of Fe-coarsening of impregnation-derived fine particles at the operating temperature.

4.4.2 Understanding the Mechanism of BZC4YYb-boosted Reduction Kinetics

To confirm the role of proton in catalyzing Fe-oxide reduction, TPR studies were performed on the as-prepared Fe_2O_3/BZC4YYb materials using 10% hydrogen balanced argon. The different hydrogen consumption peaks for different samples are shown in Figure 4.13a. For Fe_2O_3, there are two well separated reduction peaks, the smaller low temperature peak taking up about 13% of total surface area under TPR curve, reflects the first stage of the reduction of hematite to magnetite α-$Fe_2O_3 \rightarrow Fe_3O_4$ and the second, broad and much larger, high temperature peak represents the reduction of magnetite to metallic iron $Fe_3O_4 \rightarrow \alpha$-Fe. After introduction of BZC4YYb, the main reduction peak of Fe_2O_3 shifts to the left, from 662 ^oC to 452 ^oC, even lower than that of Fe_2O_3/ZrO_2 (605 ^oC), suggesting the enhanced reduction kinetics. This is also indirectly supported by the

third sharp peak on the TPR profile of Fe_2O_3/BZC4YYb at high temperature range, which is related to the lattice oxygen release, forming oxygen vacancies [xx]; the latter will further promote the formation of OH_O^* in the presence of water vapor. Figure 4.13b shows the TPR profiles collected at different heating rates.

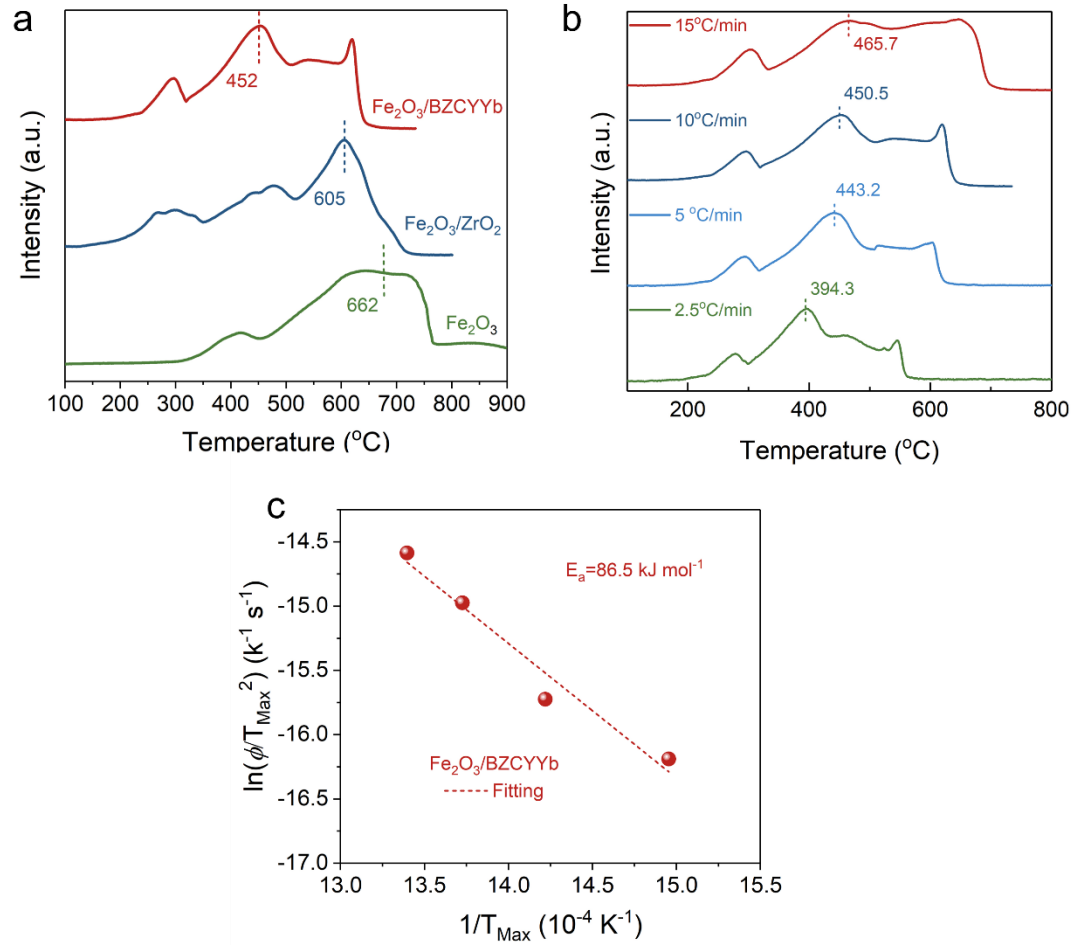

Figure 4.13 TPR profiles of different samples at a ramping rate of 10 °C/min: Fe_2O_3 (bottom); Fe_2O_3/ZrO_2 (medium) and Fe_2O_3/BZC4YYb mixed by milling; (b) TPR profiles under different ramping rates for Fe_2O_3/BZC4YYb mixed by milling; (c) Temperature-programmed Arrhenius plots corresponding to the fitting results.

With increasing the ramp rate, all the reduction peaks experienced a right shift, which might be caused by the diffusion limitations of reduction at high heating rates. According to the Kissinger's method, the linear relationship between $\ln\left(\frac{\Phi}{T_{max}{}^2}\right)$ *vs.* $\frac{1}{T_{max}}$

is observed in Figure 4.13c. From the slopes in Figure 4.5c, Fe_2O_3/BZC4YYb exhibits an activation energy of 86.5 kJ mol^{-1} for reduction from Fe_3O_4 to Fe, while Fe_2O_3/ZrO_2 exhibits an activation energy of 81.5 kJ mol^{-1} for reduction from FeO to Fe.

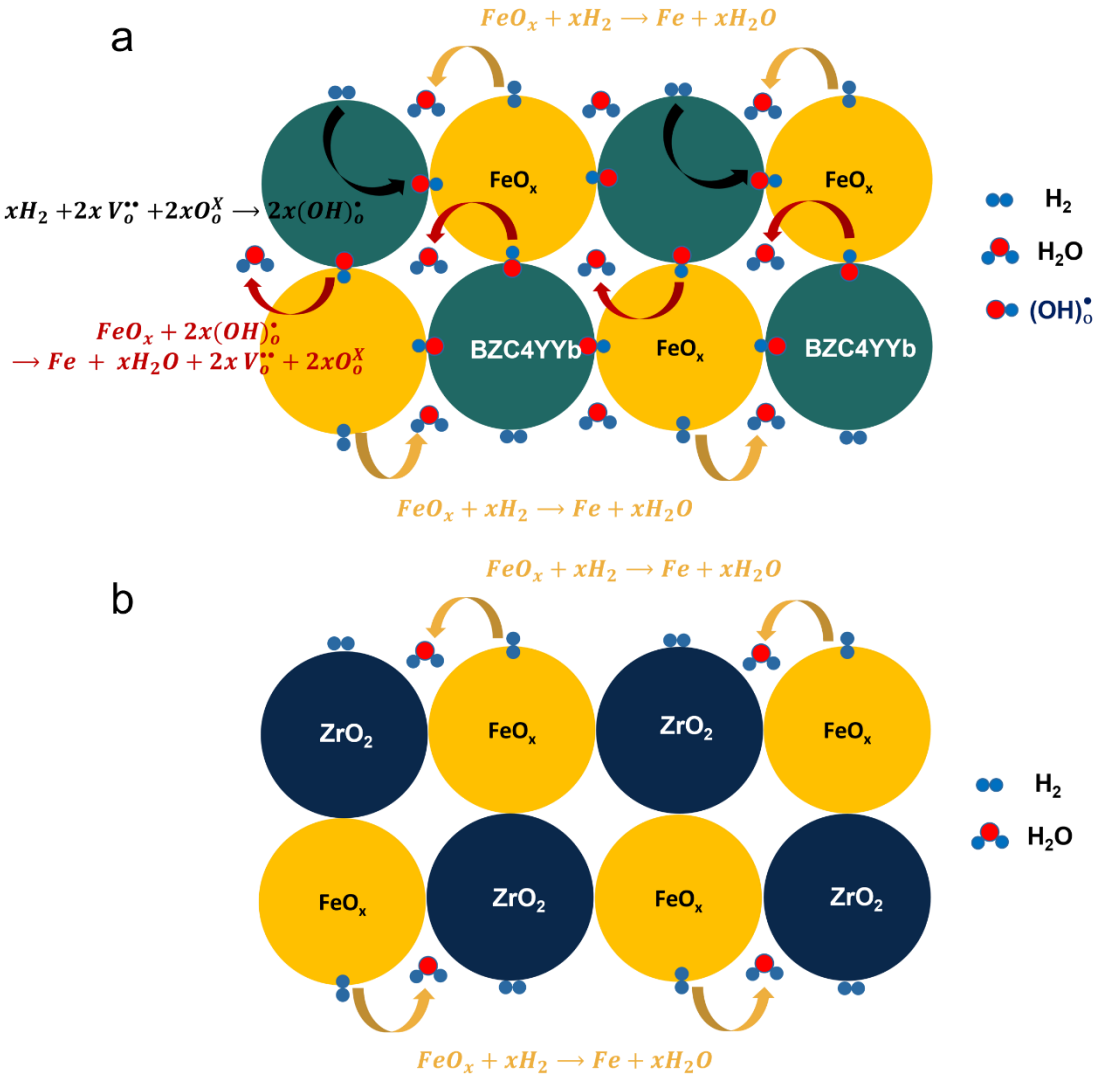

Figure 4.14 Schematic illustrating reduction process with hydrogen for: (a) proton conducting-mediated iron oxide; (b) ZrO_2-mediated iron oxide.

To understand the beneficial effect of proton conducting oxide support on the reduction process of iron oxide, Figure 4.14 illustrates the schematic of reduction process with H_2 for the BZC4YYb-mediated iron oxide and Fe_2O_3/ZrO_2. As shown in Figure 4.14a, there are two parallel reaction pathways in the BZC4YYb-mediated iron oxide. On

one hand, the conventional reduction reaction of iron oxide to iron and release water takes place at the surface of iron oxide particle during charging process, as illustrated in eq. 4.2:

$$FeO_x + xH_2 \longrightarrow Fe + xH_2O \tag{4.2}$$

On the other hand, a complex reduction process also occurs at the interface of BZC4YYb and iron oxide, which consists of multiple elementary steps including (1) hydrogen adsorption on the BZC4YYb surface; (2) dissociation of hydrogen and transportation of protons through BZC4YYb bulk to the interface with iron oxide, as shown in reaction (4.3); (3) chemical reaction step of iron oxide to iron and generation of water, as shown in reaction (4.4).

$$xH_2 + 2x\,V_o^{\bullet\bullet} + 2xO_o^X \longrightarrow 2x(OH)_o^{\bullet} \tag{4.3}$$

$$FeO_x + 2x(OH)_o^{\bullet} \longrightarrow Fe + xH_2O(g) + 2x\,V_o^{\bullet\bullet} + 2xO_o^X \tag{4.4}$$

Where $V_o^{\bullet\bullet}$ represents oxide-ion vacancy, O_o^X is the lattice oxygen, and $(OH)_o^{\bullet}$ represents proton on oxygen lattice.

On the contrary, Fe_2O_3/ZrO_2 has limited reaction sites on the gas-solid interface, implying only traditional reduction pathway could occur, see Figure 4.14b. The overall reduction is expressed in (4.2).

A reverse process is expected for the oxidation process (discharge) in BZC4YYb-mediated Fe_2O_3,

$$H_2O(g) + V_o^{\bullet\bullet} + O_o^X \longrightarrow 2(OH)_o^{\bullet} \tag{4.5}$$

$$Fe + 2x(OH)_o^{\bullet} \longrightarrow FeO_x + xH_2 + x\,V_o^{\bullet\bullet} + xO_o^X \tag{4.6}$$

Thus, though the production and transportation of $(OH)_o^{\bullet}$, the additional oxygen and proton pathway could be provided to improve the overall reduction kinetics.

4.4.3 Evaluation of Electrochemical Performance

To evaluate the performance of SOIAB with BZC4YYb-mediated iron oxide ESU materials, 0.12g of as-prepared powders (with a Fe mass of 56 mg) was used as active materials and placed into battery chamber. Figure 4.15a shows the variation of OCV *vs.* time in H_2-3%H_2O in open system. A OCV of 1.14 V, near the theoretical potential, was achieved after fully reduction, implying a good gas tightness of the system. Then the performance of RSOFC was also evaluated in a closed system, where the H_2 inlet and outlet were closed. Figure 4.15b shows the V-j curve in both fuel cell and electrolyzer modes in close system, where the OCV of battery is seen to decrease to ~1.06 V after

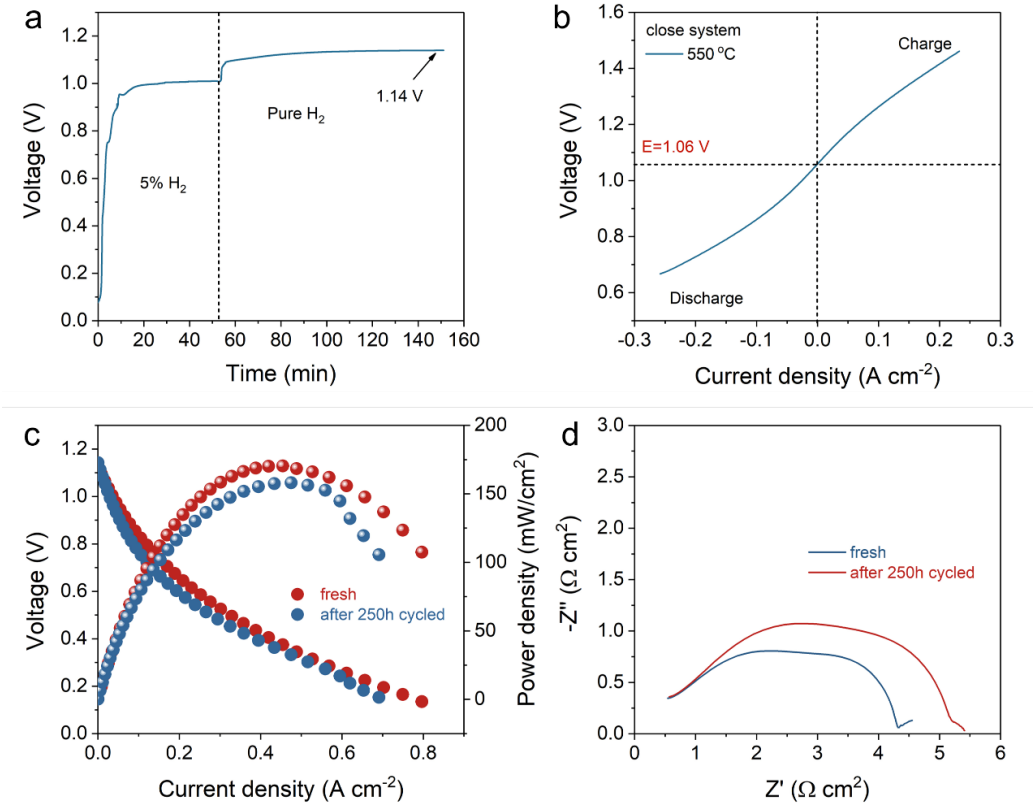

Figure 4.15 Electrochemical performance of RSOFC of battery with Fe_2O_3/BZC4YYb mixed by milling (a) A profile of OCV *vs.* time during reduction process in open system; (b) V-I curve of battery in close system; (c) Current-voltage and current-power curves and (d) EIS spectra with H_2/3% H_2O as fuel before and after cycling testing in open system.

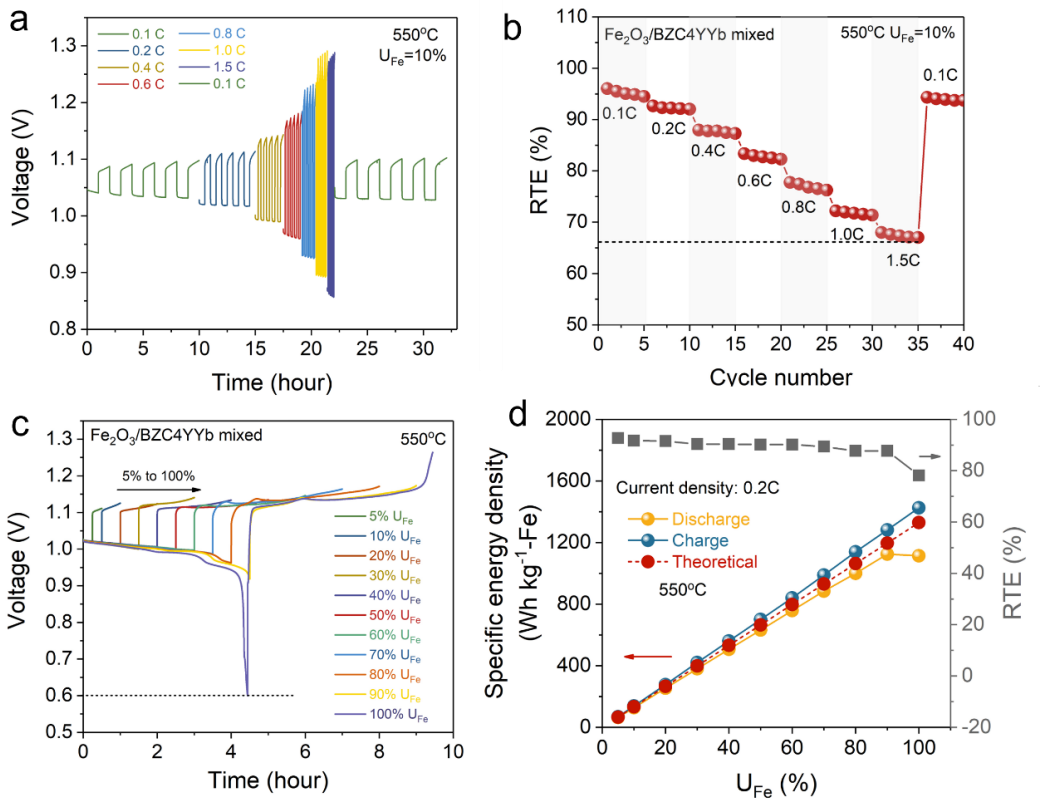

Figure 4.16 Electrochemical performance for SOIAB with Fe_2O_3/BZC4YYb mixed by milling ESU materials: (a) Voltage profiles under different current density with a fixed U_{Fe}=10%; (b) RTE *vs.* C-rate; (c) voltage profiles *vs.* time at a fixed j= 10 mA cm^{-2} (0.2 C) and different U_{Fe} (5-100%); (d) discharge and charge specific energy density and corresponding RTE *vs.* U_{Fe}.

closing the H_2 valve, signifying the equilibrium state of Fe and Fe_3O_4. The voltage is approximately linear with current density and no obvious concentration polarization even at a current density of j = 250 mA cm^{-2} at 550 °C, suggesting an excellent electrochemical performance for RSOFC. The power density and EIS of this anode supporting RSOFC was examined in open system at 550 °C. The results shown in Figure 4.15c indicate a MPD of 175 mW cm^{-2}, even after 250h cycling test at U_{Fe}=5% and a current of 10 mA cm^{-2}. A slight degradation of performance (~7.5%) is observed after the cycling. The EIS spectra shown in Figure 4.15d suggest an increase in low-frequency impedance, implying

a possible anode-microstructure change. This is indeed confirmed by the increased concentration polarization observed at 0.6 A cm^{-2} [89].

To evaluate the rate performance, the battery was cycled at different current densities of 0.1-1.5C (10 to 75 mA cm^{-2}) with an iron utilization of 10%. Figure 4.16a displays the voltage profiles *vs.* time for different C rates and the corresponding RTE is shown in Figure 4.16b. Even at 1.5 C, the battery with mechanically mixed Fe_2O_3/BZC4YYb ESU materials can still deliver a high RTE of 66.8%, while the Fe_2O_3/ZrO_2 can only reach 0.6C with a low RTE of 58% (see Figure 3.19), while Figure 4.17a shows the Fe_2O_3-impregnated BZC4YYb can only reach 0.4 C with a serious charge overpotential. When the C-rate returns to 0.1 C, a high RTE=95.2% is still achievable. After introducing BZC4YYb, the C-rate performance can be not only improved significantly, but also the performance at higher iron utilization (U_{Fe}) can be achieved, see Figure 4.16c. The discharge voltage experiences a sharp decrease at the end of discharge at U_{Fe}>90%. Similarly, the charging voltage also suffers a sharp increase toward the end of cycle. These rapid overpotential changes are attributed to the mass transport limitation caused by the formation of thick and dense Fe_3O_4/Fe layer, especially at high U_{Fe}, seriously limiting the transport process of hydrogen and water and resulting in H_2/H_2O starvation for the dis/charge cycle. Fortunately, it can cycle with a stable voltage at U_{Fe} from 5 to 90%. The SED and RTE are shown in Figure 4.16d *vs.* U_{Fe}. As expected, both DSED and CSED increase with U_{Fe}, e.g., the DSED reaches 254, 631, and 1125 Wh kg^{-1}-Fe at U_{Fe} of 20, 50, and 90%, respectively. Again, the iron oxide impregnated BZC4YYb shows sharp "voltage drop/rise" when the U_{Fe} is > 60%, see Figure 4.17b, suggesting mass transport limitation during redox process at high U_{Fe}.

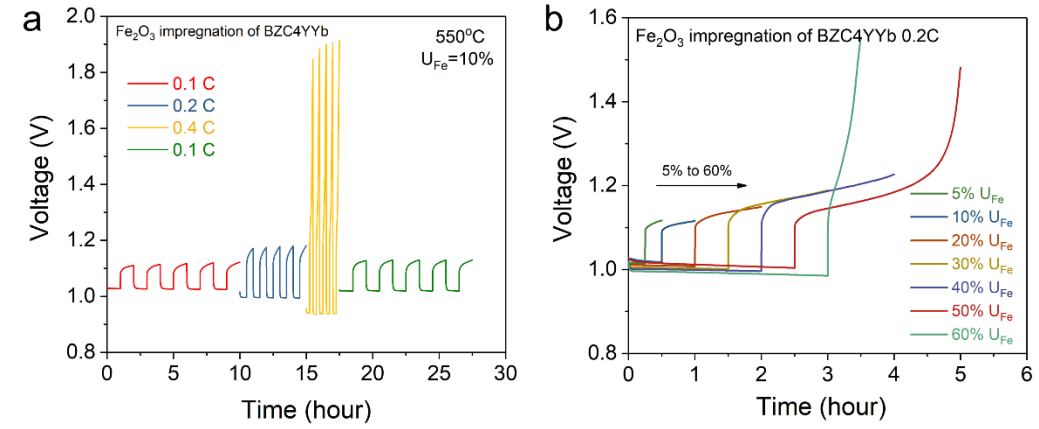

Figure 4.17 Electrochemical performance for SOIAB with Fe_2O_3 impregnated BZC4YYb ESU materials: (a) Voltage profiles under different current density with a fixed U_{Fe}=10%; (b) voltage profiles *vs.* time at a fixed j= 10 mA cm^{-2} (0.2 C) and different U_{Fe} (5-60%);

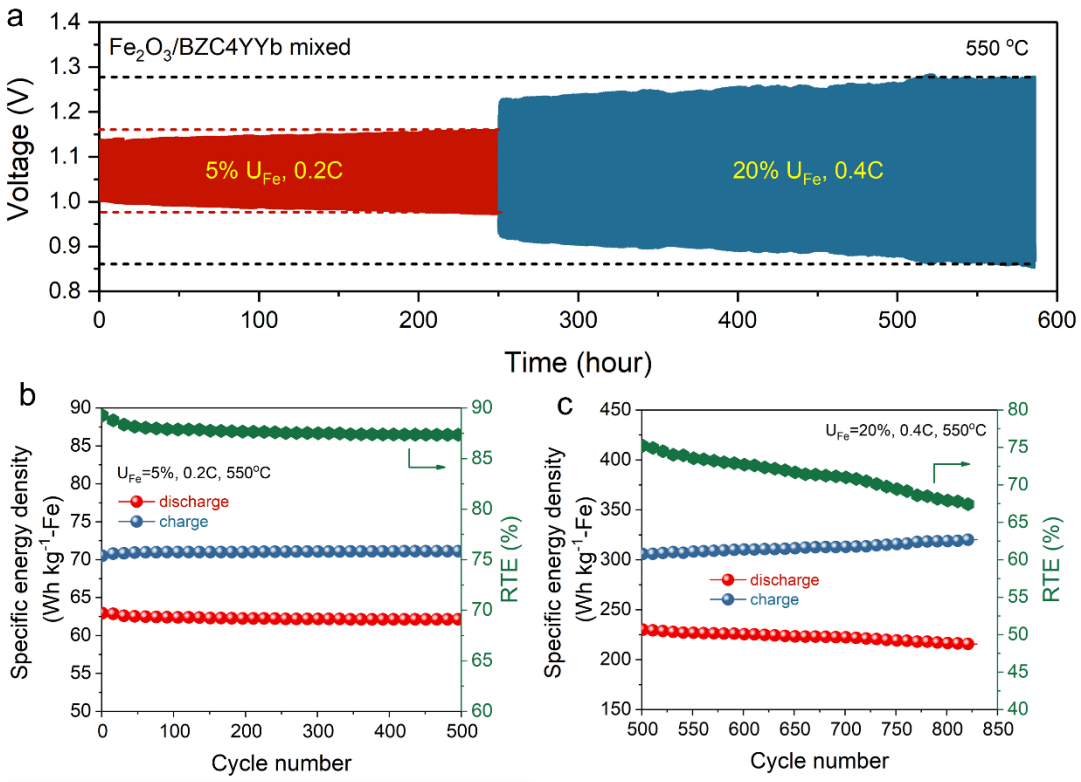

Figure 4.18 Cycling performance of a 550 ºC battery with Fe_2O_3/BZC4YYb mixed by milling ESU materials: (a) voltage profiles at U_{Fe}=5% and 0.2 C (10 mA cm^{-2}) followed by cycling at U_{Fe}=20% and 0.4 C (20 mA cm^{-2}); (c) and (d) the corresponding SED and RTE of U_{Fe}=5% and 20%, respectively.

To evaluate the long-term cycling performance, the battery with mechanically mixed Fe_2O_3/BZC4YYb ESU materials was tested at U_{Fe}=5% and a discharge-charge current density of 10mA cm^{-2}, followed by testing at U_{Fe}=20% and a current density of 20 mA cm^{-2}. Figure 4.18a shows the voltage profiles *vs.* time and the corresponding SED and RTE are shown in Figure 4.18b and 4.18c. These results suggest that over the 500 cycles tested at U_{Fe}=5%, the battery exhibits excellent stability, which delivers around discharge specific capacity of 62.5 Wh kg^{-2}-Fe with a high RTE of 87.9%. After that, the same battery was regenerated by H_2-3%H_2O and tested again under more severe conditions. When tested at higher utilization (U_{Fe}=20%) and higher current density (20 mA cm^{-2}), the battery shows a slight degradation after 350 cycles. The DSED decreases from 230 to 215 Wh kg^{-1}-Fe, while the CSED increases from 305 to 320 Wh kg^{-2}-Fe, resulting in an RTE decrease from 75% to 68%.

4.5 Summary

In this chapter, two types of new ESU materials were investigated to enhance reduction kinetics: IrO_2 as the active catalyst and BZC4YYb as oxide support. Using the improved RSOFC, the SOIAB performance was further improved by adding IrO_2 nanoparticles in Fe-based ESU, achieving high cycle efficiency of 73% at high power density of 50 mA cm^{-2} and a discharge SED of 596 Wh kg^{-1}-Fe with a RTE of 80.8% at high utilization of U_{Fe}=50% for 30 cycles. For BZC4YYb, a proton-conducting perovskite, as a support for Fe particles in ESU, a significantly enhanced kinetics of redox reactions is achieved, resulting a high RTE of ~65% at 1.5C (75mA cm^{-2}), due to the additional hydrogen and water pathways. Even at U_{Fe}=20% and a current density of 20 mA cm^{-2}, the battery can produce a DSED of 215 Wh kg^{-1}-Fe for 350 cycles with a RTE of 68%.

CHAPTER 5

CONCLUSIONS AND OUTLOOK

In this work, studies on the reduction kinetics of Fe_3O_4 derived from Fe_2O_3/ZrO_2 were carried out, starting from multiple-step reduction process with hydrogen. The work first demonstrates the need for ZrO_2 to achieve stable performance and provides key kinetic data for engineering design of SOIAB systems in the future. We show that the reduction of Fe_3O_4 to Fe follows two consecutive steps and can be reasonably described by phenomenological chemical-controlled and diffusion-controlled kinetic models. In addition, the desired iron oxide, Fe_3O_4 or FeO, has been formed *in situ* from fully reduced iron particles by precisely controlling the ratio of H_2O and H_2 concentrations and temperature. With the desired iron oxide, the reduction kinetics of one-step iron oxide to iron was studied by measuring H_2O content *vs.* time with an on-line MS and phenomenological modeling. It is found that the reduction degree of the two one-step reduction processes follows nicely the JMA phase transformation model, revealing three stages during the reduction, in which the E_a of the nucleation is faster than the growth. The kinetics of FeO-to-Fe reduction exhibits two orders of magnitude higher kinetic rate constant than that of Fe_3O_4-to-Fe counterpart with half the activation energy.

Another major contribution of this thesis is the performance of SOIAB has been improved significantly through simultaneous optimizations in testing fixture, electrolyte, and electrodes. The use of three electrode configuration allows us to pinpoint the contribution of OE, through which the individual contribution from cell component is

deconvoluted as a function of current density after combining with the battery cell voltage, ohmic resistance and Nernst potential. The finding is that HE contributes a majority of overpotential to the total cell voltage loss. Adding GDC catalyst into HE substrate significantly lowers the overpotential contribution of HE, thus further improving battery power density and stability, especially at low-C-rate and low-U_{Fe}. In general, C-rate has a more pronounced impact on cycle stability and RTE than U_{Fe}. Higher temperature in general promotes rate performance and RTE but again at a cost of cycle stability due to sintering of Fe-particles. Overall, given the excellent low C-rate performance and low-cost Fe, it is reasonable to regard SOIAB as a suitable LDES device. With large-size RSOFCs and more Fe-bed material loading, achieving 10+ hour electricity storage for SOIAB is straightforward.

The majority of SOIAB work focus on developing new ESU materials for improving reduction kinetics. Here we have investigated two types of new materials: IrO_2 as the active catalyst and BZC4YYb as oxide support. Using the improved RSOFC, the SOIAB performance was further improved by adding IrO_2 nanoparticles in Fe-based ESU, achieving high cycle efficiency of 73% at high power density of 50 mA cm^{-2} and a discharge SED of 596 Wh kg^{-1}-Fe with a RTE of 80.8% at high utilization of U_{Fe}=50% for 30 cycles. For BZC4YYb, a proton-conducting perovskite, as a support for Fe particles in ESU, a significantly enhanced kinetics of redox reactions is achieved, resulting a high RTE of ~75% at 1.5 C (75mA cm^{-2}), due to the additional hydrogen and water pathways. Even at U_{Fe}=20% and a current density of 20 mA cm^{-2}, the battery can produce a DSED of 215 Wh kg^{-1}-Fe for 350 cycles with a RTE of 68%.

Currently, in the current state of SOIAB technology, the major challenge is seal

technology for guaranteeing battery testing. The new battery holder has provided good gas tightness for short term though, it shows poor long-term stability, especially more than 500h testing, resulting from the other key element of battery: electrolyte. Thus, investigating on an appropriate electrolyte thickness to confirm a good gas tightness and power density should be imperative, which is of most important to LDES.

We have sought to the reduction process of iron oxide with hydrogen by MS, which provided limited kinetic mechanism. To achieve a better understanding of the redox reaction mechanisms and study the rate-limiting step, *in situ* Ambient Pressure XPS (APXPS) surface analyses should be carried out, which could increase the understanding of the surface chemistry variations occurring at the iron/iron oxide surface during a redox cycle.

REFERENCES

[1] Climate Mointoring, https://www.ncei.noaa.gov/access/monitoring/products/, National Centers for Environmental Information (2021).

[2] IEA, Net Zero by 2050, IEA, Paris https://www.iea.org/reports/net-zero-by-2050, (2021).

[3] P. Albertus, J.S. Manser, S. Litzelman, Long-Duration Electricity Storage Applications, Economics, and Technologies, Joule 4(1) (2020) 21-32.

[4] P. Denholm, M. Hand, Grid flexibility and storage required to achieve very high penetration of variable renewable electricity, Energy Policy 39(3) (2011) 1817-1830.

[5] W.A. Braff, J.M. Mueller, J.E. Trancik, Value of storage technologies for wind and solar energy, Nature Climate Change 6(10) (2016) 964-969.

[6] M.R. Shaner, S.J. Davis, N.S. Lewis, K. Caldeira, Geophysical constraints on the reliability of solar and wind power in the United States, Energy & Environmental Science 11(4) (2018) 914-925.

[7] P. Denholm, & Margolis, Robert. , Energy Storage Requirements for Achieving 50% Solar Photovoltaic Energy Penetration in California. United States. https://doi.org/10.2172/1298934, (2016).

[8] O.J. Guerra, J. Zhang, J. Eichman, P. Denholm, J. Kurtz, B.-M. Hodge, The value of seasonal energy storage technologies for the integration of wind and solar power, Energy & Environmental Science 13(7) (2020) 1909-1922.

[9] D. Aurbach, B.D. McCloskey, L.F. Nazar, P.G. Bruce, Advances in understanding mechanisms underpinning lithium–air batteries, Nature Energy 1(9) (2016) 16128.

[10] L. Grande, E. Paillard, J. Hassoun, J.-B. Park, Y.-J. Lee, Y.-K. Sun, S. Passerini, B. Scrosati, The Lithium/Air Battery: Still an Emerging System or a Practical Reality?, Advanced Materials 27(5) (2015) 784-800.

[11] H.-G. Jung, J. Hassoun, J.-B. Park, Y.-K. Sun, B. Scrosati, An improved high-performance lithium–air battery, Nature Chemistry 4(7) (2012) 579-585.

[12] K.G. Gallagher, S. Goebel, T. Greszler, M. Mathias, W. Oelerich, D. Eroglu, V. Srinivasan, Quantifying the promise of lithium–air batteries for electric vehicles, Energy & Environmental Science 7(5) (2014) 1555-1563.

[13] T. Liu, J.P. Vivek, E.W. Zhao, J. Lei, N. Garcia-Araez, C.P. Grey, Current Challenges and Routes Forward for Nonaqueous Lithium–Air Batteries, Chemical Reviews 120(14) (2020) 6558-6625.

[14] P. Tan, B. Chen, H. Xu, H. Zhang, W. Cai, M. Ni, M. Liu, Z. Shao, Flexible Zn– and Li–air batteries: recent advances, challenges, and future perspectives, Energy & Environmental Science 10(10) (2017) 2056-2080.

[15] Y. Shao, S. Park, J. Xiao, J.-G. Zhang, Y. Wang, J. Liu, Electrocatalysts for Nonaqueous Lithium–Air Batteries: Status, Challenges, and Perspective, ACS Catalysis 2(5) (2012) 844-857.

[16] B. Dunn, H. Kamath, J.-M. Tarascon, Electrical Energy Storage for the Grid: A Battery of Choices, Science 334(6058) (2011) 928-935.

[17] C. Zhang, K. Huang, An Intermediate-Temperature Solid Oxide Iron–Air Redox Battery Operated on O2−-Chemistry and Loaded with Pd-Catalyzed Iron-Based Energy Storage Material, ACS Energy Letters 1(6) (2016) 1206-1211.

[18] X. Zhao, X. Li, Y. Gong, N. Xu, K. Huang, A novel intermediate-temperature all ceramic iron–air redox battery: the effect of current density and cycle duration, RSC Advances 4(43) (2014) 22621-22624.

[19] X. Zhao, X. Li, Y. Gong, K. Huang, Enhanced reversibility and durability of a solid oxide Fe–air redox battery by carbothermic reaction derived energy storage materials, Chemical Communications 50(5) (2014) 623-625.

[20] X. Zhao, Y. Gong, X. Li, N. Xu, K. Huang, Cyclic Durability of a Solid Oxide Fe-Air Redox Battery Operated at 650°C, Journal of The Electrochemical Society 160(10) (2013) A1716-A1719.

[21] X. Zhao, Y. Gong, X. Li, N. Xu, K. Huang, Performance of Solid Oxide Iron-Air Battery Operated at 550°C, Journal of The Electrochemical Society 160(8) (2013) A1241-A1247.

[22] C. Zhang, K. Huang, MOF-derived iron as an active energy storage material for intermediate-temperature solid oxide iron–air redox batteries, Chemical Communications 53(76) (2017) 10564-10567.

[23] C. Zhang, K. Huang, A Comprehensive Review on the Development of Solid-State Metal–Air Batteries Operated on Oxide-Ion Chemistry, Advanced Energy Materials 11(2) (2021) 2000630.

[24] D.J.L. Brett, A. Atkinson, N.P. Brandon, S.J. Skinner, Intermediate temperature solid oxide fuel cells, Chemical Society reviews 37 8 (2008) 1568-78.

[25] S.Y. Gómez, D. Hotza, Current developments in reversible solid oxide fuel cells, Renewable and Sustainable Energy Reviews 61 (2016) 155-174.

[26] N. Mahato, A. Banerjee, A. Gupta, S. Omar, K. Balani, Progress in material selection for solid oxide fuel cell technology: A review, Progress in Materials Science 72 (2015) 141-337.

[27] J.B. Goodenough, Oxide-Ion Electrolytes, Annual Review of Materials Research 33(1) (2003) 91-128.

[28] S.P.S. Badwal, F.T. Ciacchi, D. Milosevic, Scandia–zirconia electrolytes for intermediate temperature solid oxide fuel cell operation, Solid State Ionics 136-137 (2000) 91-99.

[29] P. Hjalmarsson, X. Sun, Y.-L. Liu, M. Chen, Durability of high performance Ni–yttria stabilized zirconia supported solid oxide electrolysis cells at high current density, Journal of Power Sources 262 (2014) 316-322.

[30] X. Guo, E. Vasco, S. Mi, K. Szot, E. Wachsman, R. Waser, Ionic conduction in zirconia films of nanometer thickness, Acta Materialia 53(19) (2005) 5161-5166.

[31] J.W. Stevenson, K. Hasinska, N.L. Canfield, T.R. Armstrong, Influence of Cobalt and Iron Additions on the Electrical and Thermal Properties of (La,Sr)(Ga,Mg)O[sub 3−δ], Journal of The Electrochemical Society 147(9) (2000) 3213.

[32] V.V. Kharton, F.M. Figueiredo, L. Navarro, E.N. Naumovich, A.V. Kovalevsky, A.A. Yaremchenko, A.P. Viskup, A. Carneiro, F.M.B. Marques, J.R. Frade, Ceria-based materials for solid oxide fuel cells, Journal of Materials Science 36(5) (2001) 1105-1117.

[33] S. Zha, C. Xia, G. Meng, Effect of Gd (Sm) doping on properties of ceria electrolyte for solid oxide fuel cells, Journal of Power Sources 115(1) (2003) 44-48.

[34] S. Zhu, Y. Wang, Y. Rao, Z. Zhan, C. Xia, Chemically-induced mechanical unstability of samaria-doped ceria electrolyte for solid oxide electrolysis cells, International Journal of Hydrogen Energy 39(24) (2014) 12440-12447.

[35] T. Ishihara, N. Jirathiwathanakul, H. Zhong, Intermediate temperature solid oxide electrolysis cell using LaGaO3 based perovskite electrolyte, Energy & Environmental Science 3(5) (2010) 665-672.

[36] M.A. Laguna-Bercero, S.J. Skinner, J.A. Kilner, Performance of solid oxide electrolysis cells based on scandia stabilised zirconia, Journal of Power Sources 192(1) (2009) 126-131.

[37] A. Atkinson, S. Barnett, R.J. Gorte, J.T.S. Irvine, A.J. McEvoy, M. Mogensen, S.C. Singhal, J. Vohs, Advanced anodes for high-temperature fuel cells, Nature Materials 3(1) (2004) 17-27.

[38] E.D. Wachsman, K.T. Lee, Lowering the Temperature of Solid Oxide Fuel Cells, Science 334(6058) (2011) 935-939.

[39] T. Ishihara, H. Matsuda, Y. Takita, Doped LaGaO3 Perovskite Type Oxide as a New Oxide Ionic Conductor, Journal of the American Chemical Society 116(9) (1994) 3801-3803.

[40] G. Yang, C. Su, H. Shi, Y. Zhu, Y. Song, W. Zhou, Z. Shao, Toward Reducing the Operation Temperature of Solid Oxide Fuel Cells: Our Past 15 Years of Efforts in Cathode Development, Energy & Fuels 34(12) (2020) 15169-15194.

[41] S.P. Jiang, Development of lanthanum strontium cobalt ferrite perovskite electrodes of solid oxide fuel cells – A review, International Journal of Hydrogen Energy 44(14) (2019) 7448-7493.

[42] Z. Gao, L.V. Mogni, E.C. Miller, J.G. Railsback, S.A. Barnett, A perspective on low-temperature solid oxide fuel cells, Energy & Environmental Science 9(5) (2016) 1602-1644.

[43] M. Mosiałek, M. Zimowska, D. Kharytonau, A. Komenda, M. Górski, M. Krzan, Improvement of La0.8Sr0.2MnO3−δ Cathode Material for Solid Oxide Fuel Cells by Addition of YFe0.5Co0.5O3, Materials 15(2) (2022) 642.

[44] J. Yang, J.M. Polfus, Z. Li, H.L. Tuller, B. Yildiz, Role of Adsorbate Coverage on the Oxygen Dissociation Rate on Sr-Doped LaMnO3 Surfaces in the Presence of H2O and CO2, Chemistry of Materials 32(13) (2020) 5483-5492.

[45] A.G. Jolley, R. Jayathilake, E.D. Wachsman, Optimizing rhombohedral Bi2O3 conductivity for low temperature SOFC electrolytes, Ionics 25(8) (2019) 3531-3536.

[46] D.W. Joh, J.H. Park, D. Kim, E.D. Wachsman, K.T. Lee, Functionally Graded Bismuth Oxide/Zirconia Bilayer Electrolytes for High-Performance Intermediate-Temperature Solid Oxide Fuel Cells (IT-SOFCs), ACS Applied Materials & Interfaces 9(10) (2017) 8443-8449.

[47] A. Jaiswal, C.-T. Hu, E.D. Wachsman, Bismuth Ruthenate-Stabilized Bismuth Oxide Composite Cathodes for IT-SOFC, Journal of The Electrochemical Society 154(10) (2007) B1088.

[48] A. Pesaran, A. Jaiswal, Y. Ren, E.D. Wachsman, Development of a new ceria/yttria-ceria double-doped bismuth oxide bilayer electrolyte low-temperature SOFC with higher stability, Ionics 25(7) (2019) 3153-3164.

[49] L. Zeng, Z. Cheng, J.A. Fan, L.-S. Fan, J. Gong, Metal oxide redox chemistry for chemical looping processes, Nature Reviews Chemistry 2(11) (2018) 349-364.

[50] Y. Liu, L. Qin, Z. Cheng, J.W. Goetze, F. Kong, J.A. Fan, L.-S. Fan, Near 100% CO selectivity in nanoscaled iron-based oxygen carriers for chemical looping methane partial oxidation, Nature Communications 10(1) (2019) 5503.

[51] J. Adánez, L.F. de Diego, F. García-Labiano, P. Gayán, A. Abad, J.M. Palacios,

Selection of Oxygen Carriers for Chemical-Looping Combustion, Energy & Fuels 18(2) (2004) 371-377.

[52] C. Chung, L. Qin, V. Shah, L.-S. Fan, Chemically and physically robust, commercially-viable iron-based composite oxygen carriers sustainable over 3000 redox cycles at high temperatures for chemical looping applications, Energy & Environmental Science 10(11) (2017) 2318-2323.

[53] X. Zhao, X. Li, Y. Gong, N. Xu, K. Romito, K. Huang, A high energy density all solid-state tungsten–air battery, Chemical Communications 49(47) (2013) 5357-5359.

[54] D. Spreitzer, J. Schenk, Reduction of Iron Oxides with Hydrogen—A Review, steel research international 90(10) (2019) 1900108.

[55] E.R. Monazam, R.W. Breault, R. Siriwardane, Kinetics of Hematite to Wüstite by Hydrogen for Chemical Looping Combustion, Energy & Fuels 28(8) (2014) 5406-5414.

[56] K. Piotrowski, K. Mondal, T. Wiltowski, P. Dydo, G. Rizeg, Topochemical approach of kinetics of the reduction of hematite to wüstite, Chemical Engineering Journal 131(1) (2007) 73-82.

[57] B. Janković, B. Adnađević, J. Jovanović, Application of model-fitting and model-free kinetics to the study of non-isothermal dehydration of equilibrium swollen poly (acrylic acid) hydrogel: Thermogravimetric analysis, Thermochimica Acta 452(2) (2007) 106-115.

[58] A.M. Jubb, H.C. Allen, Vibrational Spectroscopic Characterization of Hematite, Maghemite, and Magnetite Thin Films Produced by Vapor Deposition, ACS Applied Materials & Interfaces 2(10) (2010) 2804-2812.

[59] B. Gunawardana, N. Singhal, P. Swedlund, Degradation of Chlorinated Phenols by Zero Valent Iron and Bimetals of Iron: A Review, Environmental Engineering Research 16(4) (2011) 187-203.

[60] A. Goikhman, P. Shvets, U. Koneva, R. Mantovan, K. Maksimova, Polycrystalline magnetite (Fe3O4) thin films from FeOx/Fe bilayers grown by pulsed laser depositions, Thin Solid Films (2018) 28-33.

[61] C.E. Seaton, J.S. Foster, J. Velasco, Redution Kinetics of Hematite and Magnetite Pellets Containing Coal Char, Transactions of the Iron and Steel Institute of Japan 23(6) (1983) 490-496.

[62] S.-S. Jung, J.-S. Lee, In-Situ Kinetic Study of Hydrogen Reduction of Fe2O3 for the Production of Fe Nanopowder, MATERIALS TRANSACTIONS 50(9) (2009) 2270-2276.

[63] M. Fanfoni, M. Tomellini, The Johnson-Mehl- Avrami-Kohnogorov model: A brief review, Il Nuovo Cimento D 20(7) (1998) 1171-1182.

[64] H. Liu, R.M. Sullivan, J.C. Hanson, C.P. Grey, J.D. Martin, Kinetics and Mechanism of the β- to α-CuAlCl4 Phase Transition: A Time-Resolved 63Cu MAS NMR and Powder X-ray Diffraction Study, Journal of the American Chemical Society 123(31) (2001) 7564-7573.

[65] M.C. Weinberg, D.P. Birnie, V.A. Shneidman, Crystallization kinetics and the JMAK equation, Journal of Non-Crystalline Solids 219 (1997) 89-99.

[66] E. Lorente, J. Herguido, J.A. Peña, Steam-iron process: Influence of steam on the kinetics of iron oxide reduction, International Journal of Hydrogen Energy 36(21) (2011) 13425-13434.

[67] K. Piotrowski, K. Mondal, H. Lorethova, L. Stonawski, T. Szymański, T. Wiltowski, Effect of gas composition on the kinetics of iron oxide reduction in a hydrogen production process, International Journal of Hydrogen Energy 30(15) (2005) 1543-1554.

[68] P. Pourghahramani, E. Forssberg, Reduction kinetics of mechanically activated hematite concentrate with hydrogen gas using nonisothermal methods, Thermochimica Acta 454(2) (2007) 69-77.

[69] R. Lueck, Frantz, W, and Lu, K., JMA analysis of the transformation kinetics from the amorphous to the nanocrystalline state, Scripta Metallurgica et Materialia 28 (1993) 1071-1075.

[70] E.R. Monazam, R.W. Breault, R. Siriwardane, Reduction of hematite (Fe2O3) to wüstite (FeO) by carbon monoxide (CO) for chemical looping combustion, Chemical Engineering Journal 242 (2014) 204-210.

[71] X. Jin, K. Huang, Precautions of Using Three-Electrode Configuration to Measure Electrode Overpotential in Solid Oxide Electrochemical Cells: Insights from Finite Element Modeling, Journal of The Electrochemical Society 167(12) (2020) 124501.

[72] A.J. Bard, L.R. Faulkner, Fundamentals and applications, Electrochemical methods 2(482) (2001) 580-632.

[73] S.A. Barnett, B.-K. Park, R. Scipioni, Effect of Infiltration on Performance of Ni-YSZ Fuel Electrodes, ECS Transactions 91(1) (2019) 1791-1797.

[74] A. Hauch, K. Brodersen, M. Chen, M.B. Mogensen, Ni/YSZ electrodes structures optimized for increased electrolysis performance and durability, Solid State Ionics 293 (2016) 27-36.

[75] B.-K. Park, D. Cox, S.A. Barnett, Effect of Nanoscale Ce0.8Gd0.2O2−δ Infiltrant and Steam Content on Ni–(Y2O3)0.08(ZrO2)0.92 Fuel Electrode Degradation during High-Temperature Electrolysis, Nano Letters 21(19) (2021) 8363-8369.

[76] M. Chen, Y.-L. Liu, J.J. Bentzen, W. Zhang, X. Sun, A. Hauch, Y. Tao, J.R. Bowen, P.V. Hendriksen, Microstructural Degradation of Ni/YSZ Electrodes in Solid Oxide

Electrolysis Cells under High Current, Journal of The Electrochemical Society 160(8) (2013) F883-F891.

[77] Q. Zhang, Q.-Y. Liu, B.-K. Park, S. Barnett, P. Voorhees, The oxygen partial pressure in solid oxide electrolysis cells with multilayer electrolytes, Acta Materialia 213 (2021) 116928.

[78] C. Zhang, K. Huang, Chapter 7 - Solid-oxide metal–air redox batteries, in: M. Lo Faro (Ed.), Solid Oxide-Based Electrochemical Devices, Academic Press2020, pp. 217-250.

[79] X. Jin, X. Zhao, C. Zhang, R.E. White, K. Huang, Computational Analysis of Performance Limiting Factors for the New Solid Oxide Iron-air Redox Battery Operated at 550°C, Electrochimica Acta 178 (2015) 190-198.

[80] C.M. Berger, O. Tokariev, P. Orzessek, A. Hospach, Q. Fang, M. Bram, W.J. Quadakkers, N.H. Menzler, H.P. Buchkremer, Development of storage materials for high-temperature rechargeable oxide batteries, Journal of Energy Storage 1 (2015) 54-64.

[81] K. Otsuka, C. Yamada, T. Kaburagi, S. Takenaka, Hydrogen storage and production by redox of iron oxide for polymer electrolyte fuel cell vehicles, International Journal of Hydrogen Energy 28(3) (2003) 335-342.

[82] X. Liu, H. Wang, Hydrogen production from water decomposition by redox of Fe2O3 modified with single- or double-metal additives, Journal of Solid State Chemistry 183(5) (2010) 1075-1082.

[83] N. Xu, C. Zhang, K. Huang, Proton-mediated energy storage in intermediate-temperature solid-oxide metal–air batteries, Journal of Materials Chemistry A 6(42) (2018) 20659-20662.

[84] M. Ni, D.Y.C. Leung, M.K.H. Leung, A review on reforming bio-ethanol for hydrogen production, International Journal of Hydrogen Energy 32(15) (2007) 3238-3247.

[85] D.K. Liguras, D.I. Kondarides, X.E. Verykios, Production of hydrogen for fuel cells by steam reforming of ethanol over supported noble metal catalysts, Applied Catalysis B: Environmental 43(4) (2003) 345-354.

[86] J. Llorca, P.R.r. de la Piscina, J.-A. Dalmon, J. Sales, N.s. Homs, CO-free hydrogen from steam-reforming of bioethanol over ZnO-supported cobalt catalysts: Effect of the metallic precursor, Applied Catalysis B: Environmental 43(4) (2003) 355-369.

[87] W. Karim, C. Spreafico, A. Kleibert, J. Gobrecht, J. VandeVondele, Y. Ekinci, J.A. van Bokhoven, Catalyst support effects on hydrogen spillover, Nature 541(7635) (2017) 68-71.

[88] O.J. Wimmers, P. Arnoldy, J.A. Moulijn, Determination of the reduction mechanism

by temperature-programmed reduction: application to small iron oxide (Fe2O3) particles, The Journal of Physical Chemistry 90(7) (1986) 1331-1337.

[89] L. Wehrle, Y. Wang, P. Boldrin, N.P. Brandon, O. Deutschmann, A. Banerjee, Optimizing Solid Oxide Fuel Cell Performance to Re-evaluate Its Role in the Mobility Sector, ACS Environmental Au 2(1) (2022) 42-64.

[90] L. Yang, C. Zuo, S. Wang, Z. Cheng, M. Liu, A Novel Composite Cathode for Low-Temperature SOFCs Based on Oxide Proton Conductors, Advanced Materials 20(17) (2008) 3280-3283.

[91] A. VahidMohammadi, Z. Cheng, Fundamentals of Synthesis, Sintering Issues, and Chemical Stability of BaZr0.1Ce0.7Y0.1Yb0.1O3-δProton Conducting Electrolyte for SOFCs, Journal of The Electrochemical Society 162(8) (2015) F803-F811.

[92] S. Choi, C.J. Kucharczyk, Y. Liang, X. Zhang, I. Takeuchi, H.-I. Ji, S.M. Haile, Exceptional power density and stability at intermediate temperatures in protonic ceramic fuel cells, Nature Energy 3(3) (2018) 202-210.

[93] C. Duan, R. Kee, H. Zhu, N. Sullivan, L. Zhu, L. Bian, D. Jennings, R. O'Hayre, Highly efficient reversible protonic ceramic electrochemical cells for power generation and fuel production, Nature Energy 4(3) (2019) 230-240.

[94] C. Duan, J. Huang, N. Sullivan, R. O'Hayre, Proton-conducting oxides for energy conversion and storage, Applied Physics Reviews 7(1) (2020) 011314.

[95] L. Yang, S. Wang, K. Blinn, M. Liu, Z. Liu, Z. Cheng, M. Liu, Enhanced Sulfur and Coking Tolerance of a Mixed Ion Conductor for SOFCs: BaZr0.1Ce0.7Y0.2, Science 326(5949) (2009) 126-129.

[96] Balart, M. J., et al.. "Grain Refinement of Deoxidized Copper." Metallurgical and Materials Transactions A 47(10) (2016): 4988-5011.

APPENDIX A

THERMODYNAMIC PROPERTIES OF OXIDATION REACTIONS

Table A.1 Thermodynamic properties of involved oxidation reactions in SOIAB

$3Fe+4H_2O(g)=Fe_3O_4+4H_2(g)$			
T (°C)	ΔG^o (kJ/mol)	K	Log(K)
500	-37.336	333.2	2.523
550	-32.831	121.2	2.084
600	-28.676	51.96	1.716
650	-24.71	25.02	1.398

$Fe+H_2O(g)=FeO+H_2(g)$			
T (°C)	ΔG^o (kJ/mol)	K	Log(K)
500	-8.762	3.909	0.592
550	-8.203	3.316	0.521
600	-7.668	2.876	0.459
650	-7.147	2.538	0.404

$3Fe+2O_2(g)=Fe_3O_4$			
T (°C)	ΔG^o (kJ/mol)	K	Log(K)
500	-857.390	8.527E+057	57.931
550	-842.209	2.809E+053	53.449
600	-827.286	3.126E+049	49.495
650	-812.466	9.454E+045	45.976

Table A.1 Continued

$2Fe+O_2(g)=2FeO$			
T (°C)	ΔG° (kJ/mol)	K	Log(K)
500	-427.552	7.729E+028	28.888
550	-421.095	5.293E+026	26.724
600	-414.641	6.415E+024	24.807
650	-408.173	1.252E+023	23.098

$4H_2(g)+O_2(g)=2H_2O(g)$			
T (°C)	ΔG° (kJ/mol)	K	Log(K)
500	-410.027	5.06E+27	27.704
550	-404.689	4.81E+25	25.682
600	-399.305	7.76E+23	23.89
650	-393.878	1.94E+22	22.289

APPENDIX B

ELLINGHAM DIAGRAM

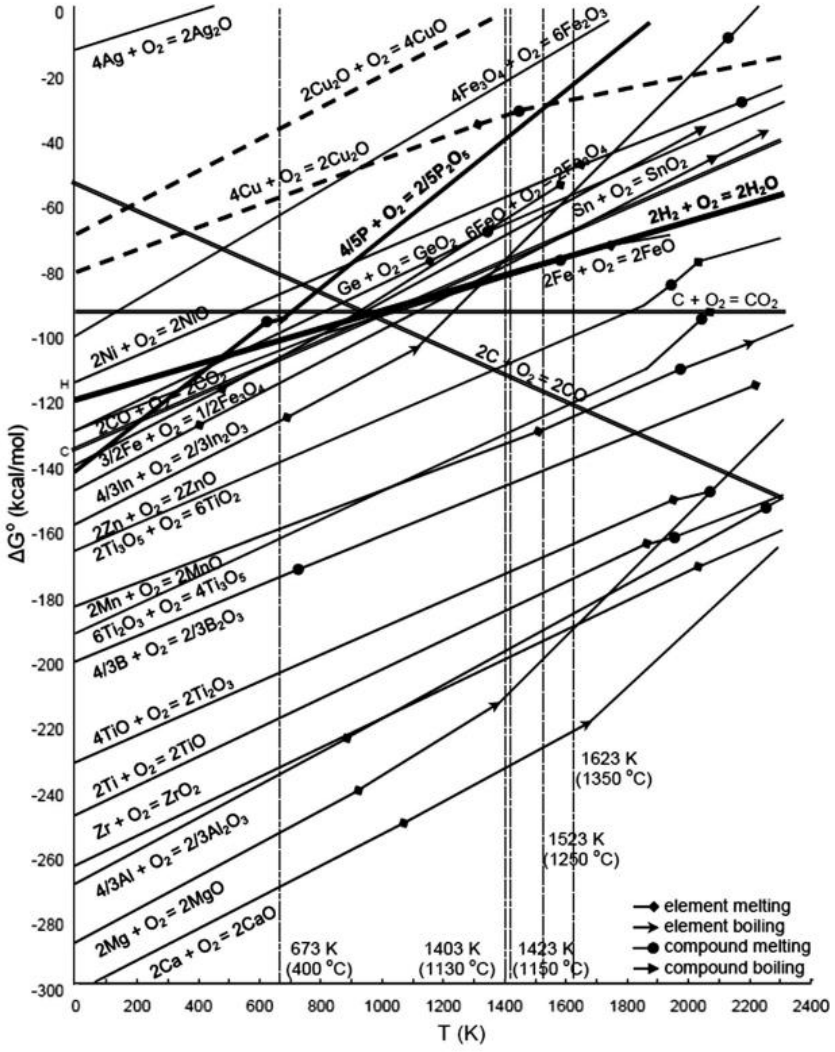

Figure B.1 Schematic of the Ellingham diagram for investigated oxides [96].

APPENDIX C

MODEL FITTING RESULTS

Table C.1 Summary of rate constants and activation energies of Fe_3O_4/ZrO_2 derived from the chemical-controlled model.

5% H_2					
T (°C)	**600**	**650**	**700**	**750**	**800**
K (s^{-1})	$1.83*10^{-4}$	$2.45*10^{-4}$	$2.86*10^{-4}$	$3.27*10^{-4}$	$3.39*10^{-4}$
R^2	0.999	0.997	0.996	0.998	0.998
E_a (kJ/mol)	24 ± 3				
10% H_2					
T (°C)	**600**	**650**	**700**	**750**	**800**
K (s^{-1})	$3.71*10^{-4}$	$4.89*10^{-4}$	$5.28*10^{-4}$	$6.85*10^{-4}$	$7.77*10^{-4}$
R^2	0.992	0.997	0.995	0.997	0.995
E_a (kJ/mol)	28 ± 2				
20% H_2					
T (°C)	**600**	**650**	**700**	**750**	**800**
K (s^{-1})	$7.96*10^{-4}$	$1.04*10^{-3}$	$1.18*10^{-3}$	$1.46*10^{-3}$	$1.50*10^{-3}$
R^2	0.991	0.991	0.994	0.991	0.995
E_a (kJ/mol)	25 ± 3				

Table C.2 Rate constants of pure Fe_3O_4 derived from the chemical controlled and combined chemical-diffusion controlled models.

Chemical-controlled			**Combined chemical-diffusion controlled**		
T (°C)	**600**	**650**	**700**	**750**	**800**
K (s^{-1})	$3.10*10^{-4}$	$4.20*10^{-4}$	$8.32*10^{-5}$	$7.45*10^{-5}$	$4.86*10^{-5}$
R^2	0.995	0.944	0.959	0.983	0.977

Table C.3 Summary of fitting results of the reduction of Fe_3O_4 to Fe at 500 to 550 °C based on the JMA model.

	5% H_2			10% H_2			20% H_2		
T (°C)	500	525	550	500	525	550	500	525	550
K (s^{-1})	$8.61*10^{-6}$	$1.07*10^{-5}$	$1.35*10^{-5}$	$2.27*10^{-5}$	$2.67*10^{-5}$	$3.67*10^{-5}$	$5.01*10^{-5}$	$5.62*10^{-5}$	$7.37*10^{-5}$
n	1.45	1.45	1.45	1.45	1.45	1.45	1.45	1.45	1.45
R^2	0.994	0.996	0.996	0.998	0.998	0.998	0.999	0.995	0.998
E_a (KJ mol^{-1})		47.6±2.8			50.6±5.6			40.1±2.3	

Table C.4 Summary of fitting results of the reduction of FeO to Fe at 700 to 850 °C based on the JMA model.

	5% H_2				10% H_2				20% H_2			
T (°C)	700	750	800	850	700	750	800	850	700	750	800	850
k(s^{-1})	$5.16*10^{-5}$	$5.41*10^{-5}$	$7.28*10^{-5}$	$7.90*10^{-5}$	$1.31*10^{-4}$	$1.45*10^{-4}$	$1.73*10^{-4}$	$1.97*10^{-4}$	$3.56*10^{-4}$	$4.05*10^{-4}$	$4.36*10^{-4}$	$5.40*10^{-4}$
n	1.45	1.45	1.45	1.45	1.45	1.45	1.45	1.45	1.45	1.45	1.45	1.45
R^2	0.996	0.997	0.996	0.994	0.997	0.996	0.997	0.996	0.997	0.996	0.997	0.996
E_a (KJ mol^{-1})		29.0±5.6				25.8±1.9				23.9±4.0		

APPENDIX D

BATTERY TESTING PROTOCOL

Table D.1 Electrochemical performance testing protocol.

1	OCV during reduction												
2	5% Hydrogen reduction												
3	Pure hydrogen reduction												
4	V-i curve for open system												
5	EIS for open system												
6	OCV during close												
7	V-i curve for close system												
8	EIS for close system												
9	Rate performance at 10%	Rate	0.1C	0.2C	0.4C	0.5C	0.6C	0.8C	1.0C	1.0C	1.5C	0.1C	
		Current	0.007A	0.014A	0.028A	0.035A	0.042A	0.056A	0.007A				
		Time	3600s	1800s	900s	720s	600s	450s	3600s				
		Cycle #	5	5	5	5	5	5	5				
10	Utilization testing	U_{Fe}	5.00%	10%	20%	30%	40%	50%	60%	70%	80%	90%	100%
		Current	0.014A	0.014A	0.014A	0.014A	0.014A	0.014A	0.014A	0.014A	0.014A	0.014A	0.014A
		Time	900s	1800s	3600s	5400s	7200s	9000s	10800s	12600s	14400s	16200s	18000s
		Cycle #	1	1	1	1	1	1	1	1	1	1	1
11	Cycling performance	U_{Fe}	5.00%	20%	50%								
		Current	0.014A	0.028A	0.028A								
		Time	900s	3600s	4500s								
		Cycle #	500	500	100								